

THE INTERPLAY BETWEEN STARBURSTS AND THEIR INTERSTELLAR MEDIUM

by

Sherry Chia-Chen Yeh

A thesis submitted in conformity with the requirements
for the degree of Doctor of Philosophy
Graduate Department of Astronomy & Astrophysics
University of Toronto

Copyright © 2013 by Sherry Chia-Chen Yeh

Abstract

The Interplay Between Starbursts and Their Interstellar Medium

Sherry Chia-Chen Yeh

Doctor of Philosophy

Graduate Department of Astronomy & Astrophysics

University of Toronto

2013

We explore massive star feedback in starburst systems, employing both theoretical approaches and observational studies. First we investigate this topic using ionization parameter \mathcal{U} as a tool to measure radiation pressure feedback in H II regions. Starburst galaxies display $\log_{10} \mathcal{U} \lesssim -2.3$, while single H II regions never show very high \mathcal{U} . In our theoretical study, we show that in a resolved H II region, \mathcal{U} is limited to $\log_{10} \mathcal{U} \lesssim -1$ when radiation pressure is important. The observed ionization parameter \mathcal{U}_{obs} cannot exceed this maximum, and stellar winds and photoevaporative flows in the region can reduce \mathcal{U}_{obs} . On the other hand, we show that the limit $\log_{10} \mathcal{U} \lesssim -2.3$ of starburst galaxies is likely due to radiation pressure and internal dust extinction in their H II regions. The effect of stellar wind pressure cannot be large relative to radiation pressure and internal dust extinction, and H II regions in starburst are not adiabatic wind bubbles.

We then study the characteristic diagnostic $[\text{O III}]/\text{H}\beta$ and $[\text{N II}]/\text{H}\alpha$ line ratios of different H II region models. We found that at a fixed ionizing spectrum and metallicity, there is a unique mapping between the line ratios and \mathcal{U} and H II region density. We also confirm that under strong stellar winds with the influence of radiation pressure, an H II region cannot reach high \mathcal{U} . The assumption of an adiabatic wind bubble with high \mathcal{U} breaks down when reaching the high luminosity required to produce high \mathcal{U} values.

In our observational studies, we present the first fully calibrated H₂ 1–0 S(1) image of 30 Doradus, together with a Br γ image. The morphologies of H₂ emission traces the CO-emitting clouds well, and H₂ spatially correlates with Br γ , implying that the observed H₂ emission arises from the photodissociation regions of 30 Doradus. With the H₂ to Br γ line ratio analysis and photoionization modeling efforts, we suggest that H₂ emission comes from molecular gas of density 10^2 to 10^3 cm⁻³, at a depth of $A_V \sim 0.34$. We further suggest that radiation pressure is not important in 30 Doradus; stellar winds and photoevaporative flows are at work to reduce the \mathcal{U}_{obs} of 30 Doradus.

Dedication

For my paternal grandmother, the strongest woman who taught me power of endurance.

For my paternal grandfather, the most gracious man who taught me wisdom of kindness.

For my mother, the most truthful woman who gave me a heart of honesty.

For my father, the most open-minded man who gave me eyes of curiosity.

And for my little brother, who always has innovative perspectives for life and the world.

Acknowledgements

I am forever indebted to my family's unconditional support, from the very first day at primary school to the last day of my PhD study. I am also grateful to my PhD thesis advisors, Prof. Ernie Seaquist and Prof. Christopher Matzner, for their astronomical patience in guiding me through the muddles in the early stage of the PhD study, and for training me to become an independent researcher. I would like to express my gratitude to all the support staff and scientists at the Gemini Observatory and the National Optical Astronomy Observatory, for all their assistance during the observing runs of collecting my thesis data. I am grateful to all the advices I have received from the Cloudy team, which tremendously helped me to accomplish the numerical studies for the thesis. I also thank my thesis projects collaborators, for their aids and insightful discussions. I am grateful to have received profound professional training during the earlier stage of my career, from Academia Sinica Institute of Astronomy and Astrophysics.

What a bliss it has been for me to have met many incredible people, most of whom have become my best friends for life, during the 6-year journey of my PhD study. Among my best friends, I especially thank Mr. Lucas Fuhrman, for supporting and loving me for who I am. Last but not least, I would like to thank my borrowed-pet, R2 the cat, for those warm and furry cuddling sessions.

There are simply not enough words to express my endless gratitude. Thank you, to everyone I have come across in my life. I would not have made it this far without any of you.

Contents

1	Introduction	1
1.1	HII Regions, the Classical and Modern Views	1
1.2	Photodissociation Regions	3
1.3	Topics in the Thesis	3
1.3.1	Part I: Theoretical Work	4
1.3.2	Part II: Observational Work	5
2	Ionization Parameter as a Diagnostic of Radiation and Wind Pressures in HII Regions and Starburst Galaxies	7
2.1	Chapter Overview	7
2.2	Introduction	8
2.3	Quasi-Static HII regions: Parameters, Properties, and Saturation of \mathcal{U}_{obs}	12
2.3.1	Ionization Parameter, Radiation Pressure, and Dust Opacity . . .	15
2.3.2	Radiation Confinement and Saturation of \mathcal{U}_{obs}	17
2.3.3	Pressurized Inner Boundary	20
2.4	Factors affecting \mathcal{U}_{obs} in individual HII regions	22
2.4.1	Pressurization by Shocked Stellar Winds	22
2.4.2	Clumps Within HII Regions	25
2.4.3	Magnetic Fields	27
2.4.4	Inertially-Confined and Impulsive Regions	27

2.4.5	Additional Effects: Recombination Line Pressure and Photoelectric Heating	28
2.5	Dust-bounded Regions and Saturation of \mathcal{U} from Selective Dust Attenuation	30
2.5.1	Internal Dust Extinction	30
2.5.2	External Dust Extinction	33
2.6	Numerical Models of Quasi-Static HII Regions	35
2.6.1	Spectral synthesis and photoionization models	36
2.6.2	Mapping Line Ratios to \mathcal{U}_{obs}	36
2.6.3	Model Parameters	39
2.6.4	Results	40
2.7	Discussion: implications of \mathcal{U}_{obs} Saturation in Starburst Galaxies	43
2.8	Conclusions	44
3	Line Emission from Radiation-Pressurized HII Regions: Internal Structure and Line Ratios	57
3.1	Chapter Overview	57
3.2	Introduction	58
3.3	Photoionization Models	60
3.4	Cloudy Model Results and Discussion	62
3.4.1	Mapping \mathcal{U} to the BPT Diagram	62
3.4.2	Quasi-Static HII Regions on the BPT Diagram	64
3.4.3	Comparison of Different Photoionization Models	68
3.5	Conclusions	70
4	The 30 Doradus Nebula: An Imaging Study of Molecular and Ionized Hydrogen	72
4.1	Chapter Overview	72
4.2	Introduction	73

4.3	Observations and Data Reduction	75
4.3.1	Ripple Pattern Removal in the Br γ Image	76
4.3.2	PSF Matching Among the H $_2$, Br γ , and Ks Images	78
4.3.3	Continuum Subtraction	81
4.3.4	Flux Calibration	84
4.4	Results	86
4.4.1	H $_2$ and Br γ Morphologies	86
4.4.2	Areas of Interest	88
4.4.3	The Spatial Relationships Between Ionized and Molecular Gas in 30 Doradus	90
4.4.4	H $_2$ to Br γ Line Ratio	94
4.5	Photoionization Models	95
4.5.1	Motivations	95
4.5.2	Model Parameters	100
4.6	Model Results and Discussion	101
4.6.1	Bright Emission Line Contamination	101
4.6.2	Origin of the H $_2$ 1–0 S(1) Line Emission	104
4.6.3	Radiation Pressure	105
4.7	Summary	109
5	Conclusions	111
6	Future Work	114
6.1	Near Future	115
6.1.1	Line Emission From Radiation-Pressurized HII Regions: Dynam- ics and Population Synthesis	115
6.1.2	Spectroscopic Studies of the 30 Doradus PDR	116
6.1.3	High-resolution Spectroscopic Studies of Mass-Loading in 30 Doradus	120
6.2	Far Future	123

7 Appendix	125
7.1 A. Force balance and pressure equilibrium	125
7.2 B. Dusty, radiation-dominated HII regions: the planar limit	126
Bibliography	131

List of Tables

2.1	Definitions	16
2.2	Mid-Infrared Forbidden Lines ^a	29
2.3	Coeval Massive Cluster Ionizing Spectra	39
2.4	Physical parameters of starburst galaxies	42
3.1	Comparison of Model Parameters	63
3.2	Optical Emission Lines on the BPT Diagram	64
4.1	Observation Summary	77
4.2	Filter Configurations	79
4.3	Emission lines within the Ks bandpass	102

List of Figures

2.1	Parameter space of HII regions surrounding central wind bubbles . . .	21
2.2	Influence of internal dust absorption	34
2.3	Argon line ratio vs. \mathcal{U} and n_H	37
2.4	Neon line ratio vs. \mathcal{U} and n_H	38
2.5	Sulphur line ratio vs. \mathcal{U} and n_H	38
2.6	Pressure and electron density profiles of HII regions	50
2.7	One-zone model of Neon line ratio as a function of \mathcal{U} and n_H	51
2.8	\mathcal{U} as a function of radiation and wind pressure parameters	52
2.9	Neon line ratio vs. \mathcal{U} and n_H at 4 Myr	53
2.10	Neon line ratio vs. \mathcal{U} and n_H at 6 Myr	54
2.11	f_{ion} as a function of radiation and wind pressure parameters	55
2.12	Individual and galactic-scale HII regions and their \mathcal{U}_{obs}	56
3.1	One-zone calculations of \mathcal{U} on the BPT diagram	65
3.2	Models compared on the BPT plot	69
4.1	$\text{Br}\gamma$ image of 30 Doradus.	79
4.2	$\text{Br}\gamma$ image of 30 Doradus, ripple patterns removed.	80
4.3	H_2 1–0 S(1) image.	85
4.4	Three-color composite image of 30 Doradus	87
4.5	H_2 , $\text{Br}\gamma$, and CO 1–0 emission in 30 Dor	91
4.6	Areas of interest in 30 Doradus	92

4.7	H ₂ to Br γ line ratio map in 30 Dor	96
4.8	H ₂ to Br γ line ratio map of Area A	97
4.9	H ₂ to Br γ line ratio map of Area B	98
4.10	H ₂ to Br γ line ratio map of Area C	99
4.11	Cloudy modeled continuum spectrum	103
4.12	Modeled H ₂ to Br γ ratio vs. densities	106
6.1	Modeled H ₂ line ratios vs. densities	120
7.1	Dust optical depth, emission-averaged ionizing radiation pressure-to-gas ratio, and fraction of ionizing radiation absorbed by gas within planar, radiation-confined, dusty HII regions	129
7.2	$\log_{10} \bar{\Xi}_{i,\text{geom}}$ and $\log_{10} \bar{\Xi}_{i,\text{em}}$ in planar, radiation-confined ionized layers with no internal pressure	130

Chapter 1

Introduction

Feedback of energy and momentum of massive stars in starburst galaxies is vital in galaxy evolution, for its potential in unbinding large molecular clouds (Krumholz et al. 2006; Fall et al. 2010; Murray et al. 2010) and driving turbulent motions within the clouds (Matzner 2002), eroding molecular clouds by photoevaporation (Whitworth 1979; Williams & McKee 1997; Matzner 2002), and triggering gravitational collapse inside the clouds and leading to subsequent star formation (Elmegreen & Lada 1977; Oey et al. 2005; Zavagno et al. 2010). Energy and momentum feedback occur at the interfaces between ionized gas and warm molecular clouds. Therefore H II regions and photodissociation regions are the agents mediating the interaction between young massive stars and their interstellar medium. Understanding physical properties of these regions, such as their density structures, emission line spectra, amount of FUV energy penetrated into molecular clouds, and dynamical expansion of ionized gas, is crucial to decipher feedback from young massive stars.

1.1 HII Regions, the Classical and Modern Views

Hot O type and B type stars emit photons with energy higher than 13.6 eV, ionizing their surrounding ISM and creating a region filled with ionized gas. This region,

known as an H II region, was named for its abundant line emissions of singly ionized hydrogen. A classical picture of an H II region is presented by Strömgren (1939): a sphere filled with gas of singly ionized hydrogen, with the ionizing star in the center. The size of the H II region depends on the ionizing flux a star can produce; the edge of an H II region occurs when the equilibrium between ionization and recombination shifts dramatically to favor neutral gas. This sphere filled with H II gas is also called a Strömgren sphere, and the radius of the ionization front (IF) is known as the Strömgren radius. The Strömgren sphere is completely filled with H II gas of homogeneous density, which is typically of low density ($n_H < 10 \text{ cm}^{-3}$) and the temperature is 7000 to 10,000 K. While the classical view of H II regions is simple and has been widely adopted in studies of ionized gas in external galaxies, inferring the ionizing sources and their ISM properties, many modern observations have revealed that H II regions are much more complicated than Strömgren spheres.

Many H II regions are in fact not perfectly spherical but rather porous. Some have a ‘blister’ appearance and produce ‘champaign flows’ of ionized gas (Whitworth 1979); many smaller dense structures are found inside H II regions, such as evaporating gaseous globules (EGGS) (Hester et al. 1996) seen in M16, which are also known as ‘elephant trunks’ for their elongated pillar-like morphology when viewed edge on, and photoevaporating disks seen in M42 (O’dell et al. 1993). Spatially very compact ($\leq 0.1 \text{ pc}$) H II regions of very high ionized gas density ($\geq 10^4 \text{ cm}^{-3}$) are discovered around very young massive stars (Wood & Churchwell 1989); hot (few million K) X-ray emitting gas is found inside H II regions (Townesley et al. 2003; 2006). None of these features agrees with the classical H II region descriptions, which indicates that in a real H II region, far more physical processes are at work than those predicted in a classical Strömgren sphere.

1.2 Photodissociation Regions

Photodissociation regions (PDRs) are the regions where FUV ($6 \text{ eV} < h\nu < 13.6 \text{ eV}$) photons interact with the neutral interstellar medium, contributing to the thermal balance and chemistry, shaping density structures of the clouds, and regulating star formation. Early observations revealed this region of neutral clouds resides outside of H II regions and is very luminous in the infrared (Melnick et al. 1979; Storey et al. 1979; Russell et al. 1980; 1981). A typical PDR has a layered appearance, starting at the IF, followed by a layer of HI gas, then a H₂-emitting layer, and finally CO emission. PDRs are often associated with atomic gas, but the FUV photons can still affect the chemistry and heating extending to a depth $A_V \sim 10$, where the atomic HI layer typically extends to $A_V \sim 2$ (van Dishoeck & Black 1988). Since most molecular gas is found in giant molecular clouds at $A_V \lesssim 10$, most of the molecular gas and all atomic gas, and thus their dust content, are in PDRs and under strong influence of the FUV radiation (Hollenbach & Tielens 1997). Therefore the physical and chemical processes in PDRs, such as the FUV radiation field strength, clumpiness of the clouds, heating and cooling processes, element abundances, emission line spectra, bear useful information in regulating molecular cloud properties and star formation.

1.3 Topics in the Thesis

While H II region and PDR studies cover a very broad spectrum of research, for the vast topics of physics and chemistry involved in shaping these regions, we focus on two major topics as follows: (1) understanding the role of radiation pressure and stellar wind pressure produced by young massive star clusters, and their impact on shaping H II region density structures and thus emission line spectra of the region, and their implications on star-forming galaxies, and (2) the morphology and physical properties of the PDRs in the 30 Doradus nebula via H₂ and Br γ emission lines, using

the observations we have conducted using the NOAO Extreme Wide Field Infrared Imager on the CTIO 4-meter telescope.

The first part is investigated, theoretically, through analytical methods combined with 1-D photoionization numerical models, focusing on H II region structure studies. The second part is explored through observational approaches, using the NIR imaging data of the nebula to investigate physical properties at the interface between H II region and PDR of 30 Doradus.

1.3.1 Part I: Theoretical Work

Feedback of radiation pressure in an H II region can be detected by measuring the ionization parameter \mathcal{U} . This dimensionless parameter is defined as the ratio of ionizing photon density to hydrogen density, $n_{\gamma,i}/n_H$, which also indicates the ratio of radiation pressure to gas pressure (Krolik 1999) and the ionization state of the gas (Tarter et al. 1969). This parameter can also be determined from observations of forbidden line ratios. Therefore, it is important to understand the physical and observational effects which influence the values of \mathcal{U} . Individually resolved starburst H II regions never reach arbitrarily high \mathcal{U} values, in contrast to the conventional H II region model that \mathcal{U} should reach very high values when the ionizing source produces high ionizing luminosity thus high $n_{\gamma,i}$. On the other hand, starburst galaxies often display a saturated ionization parameter value $\log_{10} \mathcal{U} \simeq -2.3$ (see Figure 2.12 in Chapter 2). These indicate that there must be physical mechanisms at work that limit \mathcal{U} and the ionized gas state in single H II regions and H II regions on the galactic scale. In Chapter 2, we explore several physical mechanisms within H II regions, including radiation pressure, stellar wind pressure, and photoevaporative flows of clumpy ISM. Combining both analytical considerations and numerical models, we also assess the potential of using \mathcal{U} as a useful tool to measure radiation pressure feedback in H II regions and in distant galaxies.

Following the work above, we extend the studies to understanding H II regions' optical line emission diagnostics in $[\text{O III}]_{\lambda 5007}/\text{H}\beta$ and $[\text{N II}]_{\lambda 6584}/\text{H}\alpha$ using the Baldwin-Phillips-Terlevich (BPT) diagram (Baldwin et al. 1981; Veilleux & Osterbrock 1987). The BPT diagram is commonly adopted to empirically distinguish star-forming galaxies from active galactic nuclei (AGNs). The different ionization mechanisms in the two types of objects give rise to characteristic $[\text{O III}]/\text{H}\beta$ and $[\text{N II}]/\text{H}\alpha$ line ratios, placing star-forming galaxies and AGNs on the lower left and upper right of the BPT diagram, respectively. While local star-forming galaxies obey a tight correlation on such a diagram, high-redshift star-forming galaxies display a curious offset in the diagram, which is distinct from local galaxies but they do not fall into the AGN regime (e.g., see Figure 1 in Erb et al. 2006). In order to understand the physical mechanisms which give rise to distinct line ratios of high-redshift galaxies, we first modeled quasi-static H II regions with combinations of radiation pressure and stellar winds, discuss each different regions and their implications on the BPT diagram. In a collaborative work (Verdolini et al. 2012, in prep.), our quasi-static models are adopted into H II region dynamical models, which take into account the expansion of H II regions and meant to represent the entire galaxy.

1.3.2 Part II: Observational Work

Next we explore feedback from massive stars observationally. It is crucially important to understand the FUV radiation field strength in PDRs, as it controls the heating processes and affects chemistry and structure of the PDR. H_2 emission line ratios of ro-vibrational transitions will reveal the excitation mechanisms of those lines in the PDR, thus providing useful information on the FUV radiation field and the PDR density structures. 30 Doradus is the best target for carrying out detailed studies of massive star feedback in H II regions and PDRs. Unlike distant starburst galaxies, 30 Doradus hosts one single very young (2 Myr) and massive star cluster R136 which

produces ionizing flux equivalent to that produced by 50 O3 stars. Its close proximity (50 kpc) also delivers high spatial resolution ($1'' = 0.2$ pc). Therefore 30 Doradus offers unique opportunities for detailed studies of massive star feedback, and it is the Rosetta stone for understanding feedback in distant starburst galaxies. We carried out wide-field of view observations of H_2 1–0 S(1) and $Br\gamma$ emission lines in the near IR in the 30 Doradus nebula. We produced the very first fully calibrated H_2 image, which was missing in the wealth of multi-wavelength studies of 30 Doradus but carries crucial information of warm molecular gas and the PDRs. Combining the observed line intensities and morphologies of H_2 and $Br\gamma$, together with numerical modeling efforts, we explore the origin of the H_2 line emission, densities of the PDR, and its spatial relations with the H II region. We further assess the impact of radiation pressure and 30 Doradus' observed \mathcal{U} values, using our understanding of radiation feedback based on our theoretical work.

Chapter 2

Ionization Parameter as a Diagnostic of Radiation and Wind Pressures in HII Regions and Starburst Galaxies

2.1 Chapter Overview

The ionization parameter \mathcal{U} is potentially useful as a tool to measure radiation pressure feedback from massive star clusters, as it directly reflects the ratio of radiation to gas pressure and is readily derived from mid-infrared line ratios. We consider a number of physical effects which combine to determine the apparent value of \mathcal{U} in observations encompassing one or many HII regions. An upper limit is set by the compression of gas by radiation pressure, when this is important. The pressure of shocked stellar winds and the presence of neutral clumps both tend to reduce \mathcal{U} for a given intensity of irradiation. The most intensely irradiated regions are selectively dimmed by internal dust absorption of ionizing photons, leading to a bias for observations on galactic scales. We explore these effects in analytical and numerical models for dusty HII regions and use them to interpret previous observational results. We find that radiation pressure confinement sets the upper limit $\log_{10}\mathcal{U} \simeq -1$ seen in individual regions.

Unresolved starbursts are known to display a maximum value of $\simeq -2.3$. While lower, this is also consistent with a large portion of their H II regions being radiation pressure dominated, given the different technique used to interpret unresolved regions, and given the bias caused by dust absorption. We infer that many individual, strongly illuminated regions cannot be significantly overpressured by stellar winds, and that even when averaged on galactic scales, the shocked wind pressure cannot be large compared to radiation pressure. Therefore, most H II regions cannot be adiabatic wind bubbles. Our models imply a metallicity dependence in the physical structure and dust attenuation of radiation-dominated regions, both of which should vary strongly across a critical metallicity of about one-twentieth solar. Material in this chapter was published as Yeh & Matzner 2012, *ApJ*, 757, 108.

2.2 Introduction

Forbidden line ratios are often employed to determine the hardness of the radiation field and the composition and physical state of irradiated gas within star-forming galaxies. Of the quantities revealed by these ratios, the ionization parameter $\mathcal{U} = n_{\gamma,i}/n_H$ – the ratio of ionizing photon density to hydrogen density – is of special interest, as it measures the dimensionless intensity of ionizing radiation. Because \mathcal{U} controls the ionization state (e.g., Tarter et al. 1969), it is easily disentangled from other parameters (Dopita et al. 2000); and because it indicates the ratio of ionizing radiation pressure to gas pressure (e.g., Krolik 1999), it encodes information about the relative importance of these forces in star formation feedback.

It is important, therefore, to understand the physical and observational effects which influence our estimates of \mathcal{U} in distant galaxies. When determined on kiloparsec scales, $\log_{10} \mathcal{U}$ appears to reach a maximum value of about -2.3 in starburst environments, and indeed holds this value throughout the inner 500 pc of M82 (Thornley et al. 2000; Förster Schreiber et al. 2001; Carral et al. 1994; Smith et al. 2006; Westmoquette

et al. 2007). These points led Thornley et al. (2000) to argue that this maximum $\log_{10} \mathcal{U}$ is a property of the starburst phenomenon. However, higher values (up to about -1) are sometimes seen in cases where H II regions are individually resolved (Snijders et al. 2007; Indebetouw et al. 2009).

Why do individual H II regions not exhibit arbitrarily high ionization parameter, and why are starburst determinations limited to $\log_{10} \mathcal{U} \leq -2.3$? Both limits strongly suggest the operation of a saturation mechanism. We know of four possibilities:

Dynamics. The characteristic values of \mathcal{U} could originate in the dynamics of expanding H II regions. Dopita et al. (2005, hereafter D05), in particular, explain the saturation of \mathcal{U} in terms of the ‘stalling’ of expanding H II regions as they decelerate to the ambient sound speed. Under a specific set of assumptions about the dynamics of H II regions and their interaction with ambient gas, this implies a unique value of \mathcal{U} at the time of stalling, which imprints itself on the line ratios integrated over an entire galaxy. However, there are two problems with the assumptions that enter this explanation.

First, D05 follow Weaver et al. (1977) in modeling H II regions as though they were enclosed stellar wind bubbles and therefore use the Weaver et al. model to describe their motions. Two pieces of evidence indicate that wind energy escapes H II regions, contrary to this assumption. Trapped wind would produce x-ray luminosities as much as two orders of magnitude higher than what is observed (e.g., in the Carina Nebula: Harper-Clark & Murray 2009). Moreover, D05 find that the wind luminosity must be drastically scaled down to reproduce the observed range of \mathcal{U} values. (We revisit this issue below in §2.4.1 and §2.8.)

Second, D05 assume that the ambient gas is the warm (ionized or neutral) component of the ISM, and therefore has a unique sound speed of roughly 10 km s^{-1} . Although this is plausible, many of the ionizing photons will be consumed as the dense molecular material or cold neutral hydrogen is being cleared away. As the

thermal sound speed of this matter is quite low, the appropriate stalling criterion involves the total (turbulent, magnetic and thermal) ambient pressure (e.g., Slavin & Cox 1993; Matzner 2002).

Homogeneous mixtures. A separate explanation has been provided by Förster Schreiber et al. (2001, FS01) in the context of the central 500 pc starburst core of M82, where their and later observations (Smith et al. 2006; Westmoquette et al. 2007) demonstrate that \mathcal{U} is remarkably uniform. The FS01 model invokes an ensemble of neutral clouds with ionized outer layers, scattered among newly formed stars. The uniformity of \mathcal{U} must therefore be sought in the properties of this mixture, which are not part of the Förster Schreiber et al. model. For this reason we do not investigate mixture models further, except to point out that most physical mechanisms limiting \mathcal{U} in individual H II regions would also operate here.

Radiation pressure confinement. Another physical mechanism for the saturation of \mathcal{U} was introduced by Binette et al. (1997) and elaborated by Dopita et al. (2002, D02) in the context of narrow-line regions in active galactic nuclei. When irradiation is sufficiently intense, ionized gas develops a pressure gradient to oppose the force of photons caught by neutral atoms and dust grains, and is squeezed into a thin layer near the ionization front (IF). This prevents gas pressure from becoming small compared to the ionizing radiation pressure (as previously argued by Ferland & Elitzur 1984). The corresponding upper limit on $\log_{10} \mathcal{U}$ depends on the ionizing spectrum and the lines used to infer ionization; a rough estimate based on pressure equilibrium gives -1.5. While this is significantly above the value of -2.3 seen in starbursts, the details of line formation, among other effects, can reduce \mathcal{U} to about its observed maximum.

Dust-limited H II regions. Finally, the observed saturation could simply be a selection effect, caused by the fact that dust absorbs most of the ionizing starlight in regions with $\log_{10} \mathcal{U} \gtrsim -2$, suppressing their line emission. Because extragalactic observations inevitably integrate over a wide range of local conditions, the inferred \mathcal{U} will be

weighted toward regions of lower intensity. Such a ‘dust-limited’ state has been shown to successfully reproduce the suppression of fine structure lines relative to far-infrared luminosity in ultra-luminous infrared galaxies (Voit 1992; Bottorff et al. 1998; Abel et al. 2009).

Our goal in this chapter is to evaluate these possibilities and, in the process, to assess whether \mathcal{U} can be a useful proxy to measure radiation pressure feedback in HII regions in external galaxies. We review the physical effects which control the state of ionized gas and the values of \mathcal{U} inferred from forbidden line ratios, focusing on its saturation in starburst galaxies and the relevance of the last two mechanisms. Because radiation pressure and dust opacity are both proportional to \mathcal{U} , they occur simultaneously. But, since they are truly two separate physical mechanisms, we take care not to conflate them. In this chapter we concentrate on the internal structures of HII regions, only evaluating a very simple model for their dynamics and galactic populations (§2.5). A companion paper (Verdolini et al. 2012, in prep., also see Chapter 3) presents a new suite of models for the emission from galactic populations of HII regions evolved with more sophisticated internal dynamics.

We begin in § 2.3 by reviewing the parameters of quasi-static, dusty, spherical HII regions. We draw here on the models of Draine (2011, hereafter Dr11), examining in detail their planar, radiation-confined limit (Appendix 7.2), but we also introduce a new parameter to account for an inner, pressurized region of shocked stellar wind. We discuss the scales of dust opacity and radiation pressure in § 2.3.1, confinement by radiation pressure and the maximum \mathcal{U} in § 2.3.2, and the influence of an inner bounding pressure in § 2.3.3.

In § 2.4 we focus on the extra effects which can reduce the maximum value of \mathcal{U} , including stellar winds and neutral clumps in the region. Magnetic fields can in principle allow \mathcal{U} to violate its nonmagnetic upper limit, but this turns out to be difficult to arrange. We discuss the effects of internal and external dust extinctions

on limiting \mathcal{U} in § 2.5. In § 2.6, we provide a survey of \mathcal{U} values obtained from modeled MIR line ratios within static and internally pressurized dusty H II regions, and demonstrate how stellar winds act to suppress \mathcal{U}_{obs} . In § 2.7, we use our results to interpret observations on the scales of individual H II regions and entire galaxies.

2.3 Quasi-Static HII regions: Parameters, Properties, and Saturation of \mathcal{U}_{obs}

In the static or quasi-static state, H II regions have several well-known limits: classical H II regions (Strömgen 1939), which lack significant radiation pressure or dust opacity; dusty H II regions (Mathis 1971; Petrosian et al. 1972) in which radiation pressure is negligible; and radiation-confined H II regions (Binette et al. 1997; Dopita et al. 2002) in which both radiation pressure and dust opacity are generally important. Recently, Dr11 has thoroughly explored the parameter space of dusty H II regions with radiation pressure, demonstrating a three-parameter family of models which takes all of these limits.

Ionization and force balance within spherical H II regions are especially simple under the following set of idealizations (Dr11): the ionized gas temperature T , the mean energy of ionizing photons $\bar{\epsilon}_i = \langle h\nu \rangle_i$, the effective dust opacity per H atom σ_d , and the effective recombination coefficient α , are all uniform constants; pressure from reprocessed radiation, such as the Lyman α line, is unimportant; the flow is static, so forces must balance; the pressure from stellar winds is neglected (which we will relax below in §2.3.3 and §2.4.1); and there are no additional forces from gravity or magnetic fields.

With these idealizations, H II regions are described by seven dimensional parameters: S , the central output of ionizing photons per second; L_i/c and L_n/c , the total

force of ionizing and non-ionizing photons¹; α , the effective recombination coefficient; $P/n_H = 2.2k_B T$, the thermal pressure² per H density; P_{IF} , the pressure at the ionization front; and σ_d .

Other dimensional parameters of interest, determined by the seven above, include: $n_{i*} = P_{\text{IF}}/(2.2k_B T)$, the H density at the ionization front; $R_{\text{St}} = [3S/(4\pi\alpha n_{i*})]^{1/3}$, the radius of a dust-free Strömngren sphere of uniform density n_{i*} ; n_{em} , the recombination-weighted ion density (eq. 2.26), and

$$\tilde{r}_{\text{ch}} = \frac{\alpha L^2}{12\pi(2.2k_B T c)^2 S'} \quad (2.1)$$

the radius of a uniform-density, dust-free Strömngren sphere whose gas pressure equals the total, unattenuated radiation pressure $L/(4\pi R_{\text{St}}^2 c)$ at its boundary. (Our \tilde{r}_{ch} differs from Krumholz & Matzner 2009, hereafter KM09's r_{ch} in that it accounts neither for the effects of dust extinction, nor for the additional pressure from stellar winds.) Yet another is R_{IF} , the ionization front radius.

We focus on three dimensionless ratios which control the structure and appearance of the HII region.³ First of these is the characteristic ratio of ionizing radiation pressure to gas pressure in a classical Strömngren sphere,

$$\begin{aligned} \Gamma &\equiv \frac{S \bar{e}_i}{4\pi R_{\text{St}}^2 c (2.2 n_{i*} k_B T)} = \frac{L_i}{L} \left(\frac{\tilde{r}_{\text{ch}}}{R_{\text{St}}} \right)^{1/2} \\ &\simeq \frac{0.93}{T_4^{1.53}} (S_{51} n_{i*,4})^{1/3}, \end{aligned} \quad (2.2)$$

where $n_{i*} = 10^4 n_{i*,4} \text{ cm}^{-3}$, $S = 10^{51} S_{51} \text{ s}^{-1}$, and we have used $\alpha = 2.54 \times 10^{-13} T_4^{-0.81} \text{ cm}^3 \text{ s}^{-1}$ (Storey & Hummer 1995). Here and elsewhere, we use the subscript 'St' to denote conditions in a classical, uniform Strömngren sphere without attenuation, rather than the actual HII region.

¹ L_n refers to the frequency range where the dust opacity is still $\simeq \sigma_d$; Dr11 assumes that the two opacities are equal.

²Ignoring helium, Dr11 takes this coefficient to be 2; our value of 2.2 assumes He is singly-ionized everywhere.

³A fourth, the total number of H atoms in the classical Strömngren sphere, is unimportant.

An alternative to Γ foregoes R_{St} as a dimensional scale in favor of the actual ionization front radius R_{IF} ;

$$\Psi \equiv \frac{R_{\text{IF}}}{\tilde{r}_{\text{ch}}}. \quad (2.3)$$

This is useful if R_{IF} is observed or derived from the dynamics of the region (KM09); we use Ψ to parameterize our simulation output in § 2.6. Bear in mind that Ψ decreases as radiation pressure becomes more important, whereas Γ increases.

Our second parameter is the dust opacity in a classical HII region,

$$\tau_{d,\text{St}} = \sigma_d n_{i^*} R_{\text{St}}. \quad (2.4)$$

Both Γ and $\tau_{d,\text{St}}$ are proportional to $(Sn_{i^*})^{1/3}$; as a result $\tau_d \propto \mathcal{U}$ in uniform HII regions.

The third parameter is the *dust discriminant*

$$\begin{aligned} \gamma &\equiv \frac{2.2k_b T}{\bar{e}_i} \frac{\sigma_d c}{\alpha} = \frac{\tau_{d,\text{St}}}{3\Gamma} \\ &= 16.3 \sigma_{d,-21} T_4^{1.8} \frac{13.6 \text{ eV}}{\bar{e}_i} \end{aligned} \quad (2.5)$$

where $\sigma_d = 10^{-21} \sigma_{d,-21} \text{ cm}^2$. This sets the relative importance of dust and neutral H atoms in absorbing ionizing photons when radiation pressure confines the gas: in a situation where gas pressure matches the ionizing radiation pressure, the dust absorbs a fraction $\gamma/(1 + \gamma)$ of all ionizing photons. Fiducial parameters ($\sigma_{d,-21} = 1, T_4 = 0.8, \bar{e}_i = 20 \text{ eV}$) give $\gamma = 7.4$.

Additional parameters are required to capture the spectral form of the incident starlight and dust opacity, the most relevant of which, β , compares the radiation force of non-ionizing starlight to that of ionizing starlight; see Dr11 and Appendix 7.2.

For emission in a given line, and therefore for the determination of line ratios and electron temperatures, the ratio of the characteristic density n_{i^*} to the transition's critical density n_{crit} is a significant additional parameter. So long as this ratio is small for all of the lines which are either observed or contribute to the collisional cooling of

the region, the density parameter will not be important. We return to this point in §2.6.

Although the above idealization of H II regions is reasonable and admits a simple parameter space, we wish to relax its approximations and assumptions when considering observational constraints. Microphysical assumptions, such as the constancy of T , can be relaxed through the use of a modern photoionization code like Cloudy or MAPPINGS; we take this approach in § 2.6. Macrophysical issues, such as stellar winds and bulk flow, must be addressed separately (§ 2.4).

2.3.1 Ionization Parameter, Radiation Pressure, and Dust Opacity

We are especially interested in observational measures of the ionization parameter $\mathcal{U}(\mathbf{r}) = n_{\gamma i}/n_H$. This is directly related to the ionizing radiation-to-gas pressure ratio

$$\begin{aligned}\Xi_i(\mathbf{r}) &\equiv \frac{P_{\text{rad},i}(\mathbf{r})}{P_{\text{gas}}(\mathbf{r})} \\ &= \mathcal{U}(\mathbf{r}) \frac{\bar{e}_i}{2.2k_B T}.\end{aligned}\tag{2.6}$$

These are both functions of position \mathbf{r} , and are each observable only in an integral sense within the region. Whereas $\mathcal{U}(\mathbf{r})$ and the ionizing spectrum set the local ionization structure and recombination spectrum, any recombination line ratio will depend on an average of \mathcal{U} weighted by the emissivities of the species involved. The value \mathcal{U}_{obs} inferred from such line ratios will naturally reflect this weighting. One observationally relevant proxy is therefore the recombination-weighted average

$$\mathcal{U}_{\text{em}} = \frac{\int n_H^2 \mathcal{U} dV}{\int n_H^2 dV},\tag{2.7}$$

where both integrals are over the entire H II region. Another commonly-used proxy is a ‘geometrical’ estimate which relies on an observational determination of the characteristic ionized hydrogen density:

$$\mathcal{U}_{\text{geom}} = \frac{S}{4\pi R_{\text{IF}}^2 n_{i,\text{obs}} c}.\tag{2.8}$$

Table 2.1. Definitions

Symbol	Definition	Reference	Note
$[\Xi, \Xi_i](\mathbf{r})$	Ratio of [total, ionizing] radiation pressure to gas pressure	Eq. (2.6)	Position dependent
$\mathcal{U}(\mathbf{r})$	Ionization parameter $n_{\gamma,i}/n$...	Position dependent
$\mathcal{U}_{\text{geom}}$	Geometric estimate $S/(4\pi R_{\text{IF}}^2 n_{\text{obs}} c)$	Eq. (2.8)	
\mathcal{U}_{obs}	Observational estimate of \mathcal{U} for individual HII region or line of sight	...	Tracer dependent
$\mathcal{U}_{\text{obs,max}}$	Maximum value of \mathcal{U}_{obs} in a quasi-static, unmagnetized layer	...	Tracer dependent
$\langle \mathcal{U}_{\text{obs}} \rangle_{\text{gal}}$	Obs. estimate of \mathcal{U} for beams spanning many HII regions	Eq. (2.23)	Biased by dust
\mathcal{U}_{em}	Recombination-weighted average of \mathcal{U}	Eq. (2.7)	Theoretical proxy for \mathcal{U}_{obs}
\bar{r}_{ch}	Char. radius for radiation-gas pressure equality	Eq. (2.1)	Similar to r_{ch} in KM09
Ψ	Radiation pressure parameter, $R_{\text{IF}}/\bar{r}_{\text{ch}}$	Eq. (2.3)	$\Psi \gg 1$ implies $P_{\text{rad}} \ll P$
Γ	Ionizing radiation pressure parameter, $\Psi^{-1/2} L_i/L$	Eq. (2.2)	$\Gamma \ll 1$ implies $P_{\text{rad}} \ll P$
Ω	Wind pressure parameter, $P_{\text{in}} V_{\text{in}} / (P_{\text{IF}} V_{\text{IF}} - P_{\text{in}} V_{\text{in}})$	Eq. (2.13)	$\Omega \gg 1$ implies $P_{\text{rad}} \ll P$
$f_{\text{trap},w}$	Wind pressure parameter, $4\pi R_{\text{in}}^2 P_{\text{in}} c/L$	KM09	
f_w	Wind force parameter $\dot{M}_w v_w c/L$...	
f_{ion}	Fraction of ionizing photons absorbed by gas rather than dust	Dr11	
τ_d	Dust optical depth to ion. photons from source to ionization front	Eq. (2.4)	$\tau_d > 1$: dust-limited HII region
γ	Dust discriminant, $\propto \sigma_d T / (\bar{\epsilon}_i \alpha)$	Eq. (2.5), Dr11	$\gamma > 1$ implies $\tau_d > 1$ when rad-confined
β	Effective ratio of non-ionizing to ionizing radiation force	Dr11	See note in Table 2.3
n_{em}	Recombination-weighted average density	Eq. (2.26)	Proxy for observed density

We also define $[\Xi_{i,\text{em}}, \Xi_{i,\text{geom}}] = (\bar{\epsilon}_i / 2.2 k_B T) [\mathcal{U}_{\text{em}}, \mathcal{U}_{\text{geom}}]$ for consistency. In a classical HII region (uniform density, negligible dust absorption, radius R_{St}),

$$\Xi_{i,\text{em}} = \frac{9}{4} \Gamma. \quad (2.9)$$

and, in such a region, $\Xi_{i,\text{geom}} = \Gamma$ by definition.

These emission-weighted averages are directly related to the dust opacity, as the following argument shows. Following Dr11, we define the local ionizing photon density to be $S\phi(r)/(4\pi r^2 c)$, and the integrated recombination rate to be $\int \alpha n^2 dV = f_{\text{ion}} S$, where $f_{\text{ion}} = 1 - f_{\text{dust}}$ is the fraction of ionizing radiation absorbed by hydrogen rather than dust. Rewriting both the numerator and denominator of equation (2.7),

we find

$$\Xi_{i,\text{em}} = \mathcal{U}_{\text{em}} \frac{\bar{e}_i}{2.2k_B T} = \frac{\phi_d}{\gamma f_{\text{ion}}} \tau_d \quad (2.10)$$

where

$$\phi_d = \frac{\int \phi(r) \sigma_d n_H dr}{\int \sigma_d n_H dr} \quad (2.11)$$

is a dust absorption-weighted average of $\phi(r)$.

Equation (2.10) is remarkable, because it relates a region's dust optical depth to its ionizing photon-to-gas pressure ratio in terms of the dust discriminant γ , and the order-unity parameters f_{ion} and ϕ take definite forms in each of the limiting regimes of static H II regions. In the context of radiation-confined H II regions, which we now discuss, γ determines the importance of dust absorption.

2.3.2 Radiation Confinement and Saturation of \mathcal{U}_{obs}

In a classical H II region ($\Gamma \ll 1, \Psi \gg 1$), except for a small region near the ionizing source (Mathews 1967), radiation pressure is negligible and has no practical effect on the distribution of ionized gas. In this case the recombination-weighted radiation pressure parameter $\Xi_{\text{em}} = (1 + \beta)\Xi_{i,\text{em}}$ is much less than unity, as can be seen from equation (2.9).

This ceases to be true as the illumination becomes more intense. All of the momentum in ionizing starlight, and (thanks to dust) some of the momentum in non-ionizing starlight, is transferred to the ionized gas. In a quasi-static region without other forces, the radiation force must be balanced by a gas pressure gradient. Many have pointed out that when radiation pressure is significant ($\Gamma \gg 1, \Psi \ll 1$), ionized gas can be effectively excluded from the interior (Elitzur & Ferland 1986) and confined to a thin shell near the IF (Binette et al. 1997; Dopita et al. 2002; Draine 2011). Within this shell the total pressure is nearly constant, as we show in Appendix 7.1, so the rise in gas pressure matches the drop in radiation pressure. Although the ratio of radiation and gas pressures varies throughout the region, its characteristic value

records a state of pressure balance – either $\Xi_{i,\text{em}} \simeq 1$, if dust absorption is negligible ($\gamma < 1$), or $\Xi_{\text{em}} \simeq 1$ if it is not ($\gamma > 1$). We explore the radiation-confined limit more quantitatively in Appendix 7.2.

Because Ξ_{em} reaches its maximum value of around unity in radiation-confined layers, the recombination-weighted ionization parameter \mathcal{U}_{em} does as well (Dr11): in a dusty layer with $\Xi_{\text{em}} \simeq 1$, we expect $\mathcal{U}_{\text{em}} = 2.2k_B T \Xi_{i,\text{em}} / [(1 + \beta)\bar{e}_i] \simeq 10^{-1.5}$. (This estimate rises to 10^{-1} in low-dust regions with $\gamma < 1$, because of the factor of $\Xi/\Xi_i = 1 + \beta$.) Moreover, the structure of the ionized zone becomes nearly independent of the strength of the illumination, apart from an overall scale, so long as $\Gamma \gg 1$.

Any ratio of forbidden lines, which are all well above or well below their critical densities, therefore saturates at a finite value in this radiation-confined limit (e.g. Binette et al. 1997). The ionization parameter \mathcal{U}_{obs} which would be inferred from a specific set of line ratios tends to be close, but not equal, to \mathcal{U}_{em} . Because the radiation force causes $\mathcal{U}(r)$ to be strongly stratified, there exists a diffuse inner region where lines preferentially form that require a higher ionization state (Dopita et al. 2002). Conversely, low-ionization transitions form in outer regions of lower \mathcal{U} . The observationally-inferred value \mathcal{U}_{obs} therefore limits to a maximum value which depends on the lines being observed in addition to all the parameters apart from the strength of illumination: the chemical abundances, dust properties, and incident spectrum. In other words

$$\mathcal{U}_{\text{obs}} \leq \mathcal{U}_{\text{obs,max}}, \quad (2.12)$$

where $\mathcal{U}_{\text{obs,max}}$ depends on the lines in question and these other parameters, but not on the radiation intensity (unless radiation pressure leads the density to cross one of its critical values). Likewise, if density-dependent tracers are used to derive $n_{i,\text{obs}}$ and $\mathcal{U}_{\text{geom}}$, then this will exhibit an upper limit in the vicinity of $\max(\mathcal{U}_{\text{em}}) \simeq 10^{-1.5}$ in the radiation-confined state. In § 2.6 we demonstrate the saturation of \mathcal{U}_{obs} for a

selection of mid-infrared emission lines with high critical densities using the Cloudy code. We find in Figure 2.8 that \mathcal{U}_{obs} derived from a particular $[\text{Ne III}]/[\text{Ne II}]$ line ratio exhibits a maximum at $10^{-1.97}$ for our fiducial parameters.

Because of the effects just described, the saturation of emission line ratios is a feature of the radiation-confined state in which photon momentum dominates over gas pressure gradients in the structure and dynamics of H II regions. As we shall see in §2.5, however, a selection effect due to dust attenuation (§ 2.5) also modulates the apparent value of \mathcal{U}_{obs} in large-scale observations of dusty galaxies ($\gamma > 1$). Both effects are important in the interpretation of galactic line ratios.

In Appendix 7.2 and Figures 7.1 and 7.2, we present the properties of H II regions in the radiation-confined state, i.e., the planar limit of Dr11’s equations in the absence of a finite pressure at the inner boundary. This limit, which corresponds to $\Gamma \gg 1$ (and $\Omega \ll 1$ in the definitions of §2.3.3), is parameterized only by the dust discriminant γ and the spectral parameter β , which quantifies the non-ionizing radiation pressure. Although these solutions are only a subset of Dr11’s three-parameter model family, they improve upon the treatment by Dopita et al. (2003) by accounting for the gas density gradient induced by radiation pressure. They show that: (1) $\Xi_{i,\text{em}}$ saturates at a value which is near unity and only logarithmically dependent on γ . (2) Dust absorbs most ionizing radiation, so $\tau_d \sim 1 - 3$ for astrophysically relevant values of γ . As Dr11 discusses, $\gamma \sim 10$ at solar metallicity unless dust is effectively removed. Therefore radiation-confined H II regions are also marginally ‘dust-limited’; see §2.5.1. (3) For relatively dust-free gas with $\gamma < 1$, the planar solution is not compact in radius. It must either be bounded inward by a bubble of hot gas, or be matched to a spherical solution (as in Dr11).⁴

In the radiation-confined shell, the column density of ionized gas takes a charac-

⁴Along with the relatively short dust drift time scale (Dr11), this suggests that dust-free gas may escape inward of the dusty layer even when γ is initially large. We do not account for this effect in our equations and models, as we assume a uniform mixture of gas and dust.

teristic maximum value: either $\simeq 2.2k_B Tc/(\alpha\bar{e}_i)$ if dust absorption is negligible, or several times σ_d^{-1} if it is not. What happens if the mean column density of the ambient medium is less than four times this shell column, so there is not enough matter to achieve it? In this case, it is easy to show that the initial Strömgen sphere forms outside \tilde{r}_{ch} , so that $\Psi > 1$ and $\Gamma < 1$: the radiation-dominated phase never occurs.

2.3.3 Pressurized Inner Boundary

The ionizing sources of H II regions (typically stars, star clusters, or AGN) often produce fast outflows which decelerate or are deflected before they reach the IF, thereby creating regions of hot and pressurized gas within the photo-ionized zone. What new parameter should we introduce to capture the effect of such zones on the H II regions' emission? The ratio of outer to inner pressures is not appropriate, because the two are equal in a classical H II region and also in a wind-confined shell. Neither is the volume fraction of the interior zone, because photo-ionized gas can be confined to a thin shell by radiation pressure just as well. Instead we choose

$$\Omega \equiv \frac{P_{\text{in}}V_{\text{in}}}{P_{\text{IF}}V_{\text{IF}} - P_{\text{in}}V_{\text{in}}} \quad , \quad (2.13)$$

where $P_{\text{IF}}V_{\text{IF}} - P_{\text{in}}V_{\text{in}}$ is the difference of the product of pressure and volume between the IF and the inner edge of the H II region (the outer edge of a pressurized bubble). This combination reflects the strength of the interior pressure, both for classical and radiation-dominated H II regions. In fact Ω directly reflects the contribution of the interior bubble to the total kinetic energy of the region, which, according to the virial theorem (McKee & Zweibel 1992), controls the expansion of it and any shell of neutral matter it pushes outward (e.g., KM09).

In Figure 2.1 we indicate the physical regimes of spherical, quasi-static, dusty H II regions surrounding a central wind bubble.

Quasi-static H II regions typically have an inward gradient of \mathcal{U} . For classical H II regions this is simply because the ionizing flux is greater at smaller radii, while

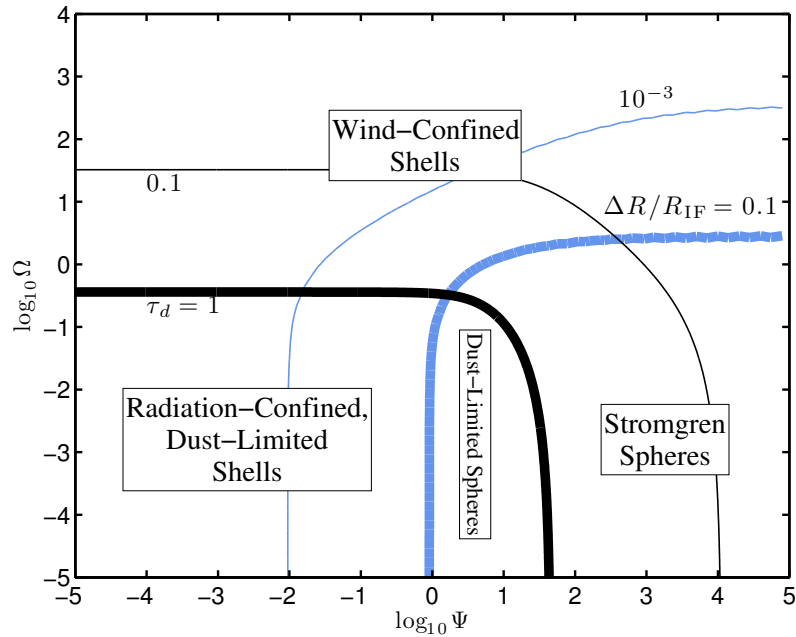


Figure 2.1: Parameter space of quasi-static, spherical, unmagnetized, dusty HII regions surrounding central wind bubbles. Wind-confined, radiation-confined, dust-limited, and classical (Strömgen) regions are indicated. Black contours denote the radial dust optical depth τ_d from the source to the ionization front; blue contours indicate the radial thickness of the ionized zone, $\Delta R / R_{IF}$. We use thick contours to separate fiducial regimes. For this figure we adopt $\beta = 1$, $\gamma = 7.4$; the radiation-confined state is encompassed by the dust-limited state so long as $\gamma > 1$.

for radiation-confined regions it is due to the gas density gradient. In either case, replacing a region's inner portion with hot gas has the effect of removing its most highly photo-ionized zone. This effect will be greatest for those lines more which form preferentially in regions of highest \mathcal{U} . See §2.4.1 for a discussion of the effect on \mathcal{U}_{obs} .

In radiation-dominated ($\Gamma \gg 1$) and relatively dust free ($\gamma \leq 1$) regions, low-density ionized gas fills the interior (Appendix 7.2). Because this low-density gas is ideal for the formation of lines sensitive to regions of high \mathcal{U} , we expect these line ratios to be especially sensitive to interior pressure when $\Gamma \gg 1$ and $\gamma \leq 1$.

2.4 Factors affecting \mathcal{U}_{obs} in individual HII regions

Several physical effects modify \mathcal{U}_{obs} relative to its theoretical maximum value $\mathcal{U}_{\text{obs,max}}$ within an individual HII region. In the following subsections we consider stellar winds, neutral clumps, dust absorption of non-ionizing light, and magnetic fields. Of these, only magnetic fields act to raise \mathcal{U}_{obs} relative to $\mathcal{U}_{\text{obs,max}}$. Although highly-magnetized regions can in principle have $\mathcal{U}_{\text{obs}} > \mathcal{U}_{\text{obs,max}}$, we shall see that this is very difficult to arrange in practice.

2.4.1 Pressurization by Shocked Stellar Winds

As discussed above in § 2.3.3, any force which clears ionized gas from the interior of an HII region will have the effect of reducing the characteristic value of \mathcal{U}_{obs} , especially for those lines which form in regions of highest \mathcal{U} . The most relevant force is the pressure of a shocked wind produced by the same source that ionizes the region. Most such regions are ionized by hot stars, which inject fast line-driven winds. However the significance of stellar wind pressure depends on the wind strength, e.g. the ratio $f_w = \dot{M}_w v_w c / L$ between the momentum fluxes of winds and starlight, and

the trapping of wind energy within the region. KM09 combine these into a single parameter $f_{\text{trap},w} \equiv 4\pi P_{\text{in}} R_{\text{in}}^2 c / L \geq f_w$ which encapsulates the contribution from shocked winds relative to the direct momentum flux of starlight.

So long as the combined force of winds and radiation compresses the ionized layer into a thin shell, the enclosed volume is constant and Ω reduces to a comparison of pressures. Since $P_{\text{IF}} \simeq P_{\text{in}} + L / (4\pi r^2 c)$ in this case (Appendix 7.1, ignoring on the last term the factor $[1 + \beta(1 - e^{-\tau_d})] / (1 + \beta)$ which accounts for incomplete absorption), we expect

$$\Omega \simeq 4\pi r^2 c P_{\text{in}} / L = f_{\text{trap},w}. \quad (2.14)$$

Further, if we consider a typical location where half of the incident radiation has been absorbed and its pressure applied to the gas, the same approximations lead to the estimate

$$\Xi \simeq \frac{1}{2f_{\text{trap},w} + 1}, \quad (2.15)$$

although, in the case where confinement is accomplished by radiation alone ($f_{\text{trap},w} \ll 1$), the values of Ξ_{em} plotted in Figure 7.2 are more accurate.

We refer to section 3.1 of KM09 for a detailed discussion of the characteristic values of f_w and $f_{\text{trap},w}$ one might expect around massive star clusters. For our purposes, it suffices to consider three limiting cases: (1) perfectly trapped, adiabatic bubbles of shocked wind, as envisioned in the models of Weaver et al. (1977) and Koo & McKee (1992) and employed by Dopita et al. (2005; 2006), which have $f_{\text{trap},w} \sim f_w v_w / \dot{R}_{\text{IF}} \gg 1$; (2) leaky wind bubbles (Harper-Clark & Murray 2009, KM09), for which $f_{\text{trap},w} \sim 1$ in the case of a very massive cluster of solar metallicity (KM09); and (3) very weak wind bubbles with $f_{\text{trap},w} \ll 1$, such as one might expect if the central source consists of low-metallicity or lower-mass main sequence stars.

In the first case (adiabatic wind bubbles) $\Omega \gg 1$ and \mathcal{U}_{obs} will be limited to values well below $\mathcal{U}_{\text{obs,max}}$. Indeed, $\mathcal{U}_{\text{geom}}$ can easily be computed from the self-similar solutions of Koo & McKee (1992): using $L = (1 + \beta) S \bar{\epsilon}_i$ and evaluating for the case of

a steady wind in a uniform medium (Weaver et al. 1977),

$$\mathcal{U}_{\text{geom}} = 2\mathcal{U}_{\text{em}} = \frac{2.2k_B T_i}{3(1 + \beta)\bar{e}_i} \frac{\dot{R}_{\text{IF}}}{f_w v_w}. \quad (2.16)$$

The factor of two in the first equality arises because a pressure-confined ionized layer is nearly uniform and optically thin to dust; therefore \mathcal{U} drops linearly in radius from the value $\mathcal{U}_{\text{geom}}$ at its inner edge. Since $v_w \simeq 10^3 \text{ km s}^{-1}$ from a young cluster which fully samples the IMF, equation (2.16) yields $\mathcal{U}_{\text{geom}} \simeq 10^{-3.8} f_w^{-1} (\dot{R}_{\text{IF}}/10 \text{ km s}^{-1})$. Equation (2.16) assumes the ionization front is trapped within the swept-up ambient matter, which requires

$$S_{49} n_{H0} > 1.5 \frac{T_4^{3.6} \dot{R}_{\text{IF}6}^5}{(1 + \beta)^3 f_w^3 v_{w8}^3} \left(\frac{20 \text{ eV}}{\bar{e}_i} \right)^3 \quad (2.17)$$

where n_{H0} is the ambient H density in cm^{-3} , $\dot{R}_{\text{IF}} = 10\dot{R}_{\text{IF}6} \text{ km s}^{-1}$, and $v_w = 10^3 v_{w8} \text{ km s}^{-1}$.

In the second case (leaky bubbles), the wind force is of order $f_{\text{trap},w} L/c$ and is therefore significant when $f_{\text{trap},w}$ exceeds unity. So long as the ionized layer is thin, the suppression of \mathcal{U}_{obs} relative to $\mathcal{U}_{\text{obs,max}}$ is of order Ξ as given by equation (2.15).

In the last case (very weak winds), \mathcal{U}_{obs} will be unaffected by their presence, although high- \mathcal{U} lines from the innermost regions may be (especially when $\gamma \leq 1$). In our modeling effort (§ 2.6), we consider a wide range of possible values for Ω .

Spherically symmetric, partially-radiative bubbles (Koo & McKee 1992; ?), which have $f_{\text{trap},w}$ lower than the adiabatic case but well above unity, are not especially relevant here because they require slower winds than is typical of ionizing stars. Fast-wind bubbles can also become radiative, however, because of mass entrainment from evaporating clumps (see §2.4.2). Note that McKee et al. (1984) argued that this effect prevents the filling factor of shocked wind, and therefore also $f_{\text{trap},w}$, from exceeding unity.

As an aside, we note that some ultracompact H II regions are probably formed in quasi-static layers confined by the ram pressure of protostellar winds, which are both

highly collimated and much stronger than radiation pressure. Combining the outflow force-luminosity correlation reported by Wu et al. (2004) with the collimation model of Matzner & McKee (1999),

$$f_w \simeq 7.4 \frac{(10^4 L_\odot / L)^{0.35}}{\sin(\theta)^2 + 10^{-4}} \quad (2.18)$$

for an angle θ from the wind axis and a bolometric source luminosity L . Such regions are typically in the first, wind-dominated regime, even well away from the wind axis. This ram-pressure confined phase can only exist in directions where the wind itself is fully ionized. The alternate case, in which the IF forms in the wind, was considered by Tan & McKee (2003). It is inertially-confined in the sense of §2.4.4 below, and can exhibit $\mathcal{U}_{\text{obs}} > \mathcal{U}_{\text{obs,max}}$.

2.4.2 Clumps Within HII Regions

HII regions are often porous and clumpy instead of spherical, as we invoked above in the context of wind trapping. Here we wish to point out that clumpiness reduces the inferred \mathcal{U}_{obs} relative to a spherical region of the same radius. The net effect is therefore to reduce \mathcal{U}_{obs} relative to $\mathcal{U}_{\text{obs,max}}$, although the upper limit does not necessarily change.

In the absence of significant radiation pressure, a clump subjected to ionizing radiation is first crushed by the recoil of its photo-evaporative flow (Bertoldi 1989). If the clump is dense enough to survive the first implosion phase, it comes into a quasi-static equilibrium with the induced pressure (Bertoldi & McKee 1990), in which its radius of curvature is r_c (on the symmetry axis, or the point most directly illuminated by starlight). Ionization balance in the presence of this accelerating and diverging photoionized flow implies

$$\frac{S}{4\pi R_c^2} = \omega \alpha n_{ic}^2 r_c$$

where n_{ic} is the ionized gas density just outside the clump IF at this point, R_c is the distance from the clump to the central source, and $\omega = 0.1 - 0.2$ (Bertoldi & McKee 1990) The parameter which describes the characteristic ionizing radiation-to-gas pressure ratio (Ξ_i) for this outflow is therefore

$$\Gamma_c = \frac{\bar{e}_i}{2.2kT_c} \left(\frac{\omega\alpha R_c S}{4\pi r^2} \right)^{1/2}. \quad (2.19)$$

Compared to conditions at a spherical IF of radius R_{IF} ,

$$\frac{\Gamma_c^2}{\Gamma_{IF}^2} = 3\omega \frac{r_c R_{IF}}{R_c^2}. \quad (2.20)$$

A clump generally has a smaller value of Γ , and therefore \mathcal{U} , than its parent region, because its radius of curvature r_c is significantly less than the ionization front radius R_{IF} of the region.

A clump's photoevaporation flow ends at a deceleration shock caused by the pressure from ionized gas in the parent region, stellar winds, or radiation. As Γ_c increases toward unity, radiation pressure requires that the shock approach the sonic point of the photoevaporation flow, and when $\Gamma_c > 1$, radiation impedes the outflow of ionized gas. For $\Gamma_c \gg 1$, the ionized gas is confined by radiation pressure to a thin layer on the surface of the clump, leading to a saturation of $\Xi_{i,em}$ and \mathcal{U}_{obs} , exactly as described in § 2.3.2 and Appendix 7.2. Just as before, dust opacity will be significant so long as $\gamma > 1$. Dopita et al. (2002) sketch the flow for $\Gamma_c \lesssim 1$.

However there is one significant difference between the effects of clumpiness and stellar winds. The ionized layer of a clump cannot be hydrostatic: it must either evaporate away, or be dragged along the clump surface by the tangential component of the radiation momentum flux, and also possibly by the stress from a turbulent boundary layer between photoionized clump gas and shocked stellar winds. Such wind and photon-driven flows are a plausible source of supersonic line widths in giant HII regions, for photoevaporative flows only produce motions of up to about twice the ionized sound speed (Bertoldi & McKee 1990). It is not at all clear that a

dynamical equilibrium exists which would prevent a clump with $\Gamma_c > 1$ from being dynamically disrupted, although a magnetic buffer zone may allow this (e.g., Dursi 2007).

2.4.3 Magnetic Fields

Magnetic fields supply an additional form of pressure which is available to balance the force of radiation, and therefore have the potential to raise \mathcal{U}_{obs} above $\mathcal{U}_{\text{obs,max}}$. However this is somewhat difficult to arrange.

Consider a planar shock of speed v_s running into a medium of hydrogen density n_0 , magnetic field perpendicular to the shock normal $B_{\perp 0}$ and Alfvén speed $v_{A0} = B_{\perp 0}/(4\pi\mu_H n_0)^{1/2}$. The post-shocked fluid is in contact with (and driven forward by the pressure of) an ionized layer. Ignoring any change in pressure across the post-shocked layer as well as streaming of the ionized gas (both of which can be order-unity effects), the density of ionized gas at the contact discontinuity is $(v_s/v_{A0})^2 n_0$ if it is pressure-supported, and $\sqrt{2}(v_s/v_{A0})n_0$ if it is magnetically supported. Magnetic pressure support therefore requires

$$v_s v_{A0} > \sqrt{2} c_i^2 \quad (2.21)$$

where $c_i \simeq 10 \text{ km s}^{-1}$ is the ionized sound speed. Magnetic support is therefore only relevant for shock speeds in excess of about $35(n_0/100 \text{ cm}^{-3})^{1/2} T_{i,4} (30 \mu\text{G}/B_{\perp 0}) \text{ km s}^{-1}$.

Magnetic fields should be relatively more important within clumpy regions, because of the tendency for streaming and turbulent flows to amplify them toward equipartition with the kinetic energy.

2.4.4 Inertially-Confined and Impulsive Regions

Our discussion so far has focused on regions which are in force balance because ionized gas resides within them for long enough to be crossed by sound waves. However,

some regions will be too young (or have crossing times too long) to develop into this state, such as the regions created in cosmological reionization. In others, ionized gas flows through the region at speeds well in excess of the ionized sound speed; these include ionized winds and jets, ionized ejecta, ionized zones of supersonic turbulence, and H II regions around runaway stars. Indeed, champagne flows (Whitworth 1979) are density-bounded to one side and are only approximately in force balance on the side toward the ionization front. None of these impulsive or inertially-confined flows is limited to $\Xi \lesssim 1$ and $U_{\text{obs}} < U_{\text{obs,max}}$ for the reasons we have outlined: therefore, higher values of U_{obs} could be taken as spectral evidence of this state.

Loosely speaking, an observation of U_{obs} above $U_{\text{obs,max}}$ implies that either a non-thermal form of pressure, such as ram pressure or magnetic fields, balances radiation pressure, that another force (such as gravity) is at play, or that there has not been time to establish equilibrium.

2.4.5 Additional Effects: Recombination Line Pressure and Photoelectric Heating

It is worth noting a couple additional effects involving the interaction among light gas, and dust:

Lyman- α trapping and dust absorption. In the absence of dust, photons from the Ly- α line scatter many times before escaping. Once the scattered line radiation is sufficiently strong its pressure will augment gas pressure, leading to an *increase* of $U_{\text{obs,max}}$ (See Elitzur & Ferland 1986, for an analysis of line pressure in the AGN context). The effect is analogous to the role of magnetic fields, except that the line pressure is proportional to the ionizing radiation pressure. At solar metallicity, a typical grain population limits the Ly- α line pressure within the ionized zone to only $\sim 6\%$ of the ionized gas pressure (Henney & Arthur 1998), but line pressure is significant at low metallicity or in regions cleared of dust. Even in the absence of dust, the dynamical effect of line

Table 2.2. Mid-Infrared Forbidden Lines^a

Species	λ (μm)	IP (eV)	n_{crit} (cm^{-3})
[Ar II]	6.99	15.76	2.0×10^5
[Ar III]	8.99	27.63	3.0×10^5
[Ne II]	12.81	21.56	6.5×10^5
[Ne III]	15.55	40.96	1.3×10^5
[S III]]	18.71	23.34	2.0×10^4
[S IV]	10.51	34.79	6.0×10^4

^aValues taken from Dopita & Sutherland (2003).

pressure limits $\log_{10} \mathcal{U} \lesssim -\infty$ within quasi-static regions (Williams 1972; Ferland & Elitzur 1984).

Dust photoelectric effect. Photoelectrons ejected from dust grains represent an additional sources of heat and ionization, while collisions and recombinations with dust grains are (less significant) sinks. These processes, considered in detail by van Hoof et al. (2004), Groves et al. (2004), and others, are fully accounted for within the Cloudy code. They depend both on the grain abundance (captured here by γ) and the grain size distribution.

Of these, trapped line radiation tends to make $\mathcal{U}_{\text{obs,max}}$ to decrease as γ increases, whereas photoelectric heating has the opposite effect by raising the ionized gas temperature in dustier gas.

2.5 Dust-bounded Regions and Saturation of \mathcal{U} from Selective Dust Attenuation

Emission lines usually arise from regions large enough to encompass many local environments, so their ratios reflect an average of the local conditions. Dust absorption has the effect of dimming high- \mathcal{U} regions, suppressing their contribution to the average and causing a saturation of the apparent ionization level. This bias arises from the dust absorption of ionizing radiation within H II regions, and from the absorption of the forbidden lines themselves, predominantly outside the regions themselves.

2.5.1 Internal Dust Extinction

If a region is sufficiently dusty, then the dust optical depth will exceed unity before radiation pressure becomes important. The critical value of the dust discriminant γ is apparent if we combine its definition (eq. 2.5) with the characteristic ionizing radiation-to-gas pressure ratio in a classical Strömngren sphere (Eq. 2.9):

$$\frac{\tau_{d,St}}{\Xi_{i,em}} = \frac{4\gamma}{3}. \quad (2.22)$$

Although this refers to the classical case of a filled Strömngren sphere, for which both $\tau_{d,St} \ll 1$ and $\Xi_{i,em} \ll 1$, it demonstrates that, when $\gamma \gtrsim 3/4$, dust extinction of ionizing photons is significant even for some regions which are not radiation dominated. Conversely, when $\gamma \lesssim 3/4$, radiation pressure confinement can occur when dust extinction is not strong. The former scenario (dust-limited regions) is consistent with our expectations of Milky Way conditions, so long as dust is not cleared from the gas; Figure 2.1 maps the physical regimes in this case. The latter applies to low-metallicity environments, or more broadly if dust clearing is effective. (We will not distinguish the critical γ from unity in our following discussion.)

Because recombination light is always redder than the photons which ionize an H II region, and because dust opacity increases with frequency, the line photons of interest

tend to escape the ionized gas relatively unabsorbed. Nevertheless, because dust consumes ionizing photons, the rate of recombinations is reduced in dust-dominated regions. The ionization efficiency f_{ion} drops from unity (for a classical HII region) to an asymptotic value of order $(1 + \beta)\tau_d/(\gamma - 1)$ (in the planar limit, when $\gamma > 1$: Appendix 7.2) as radiation pressure and dust extinction become significant; see Dr11's Eq. (21). For the parameters of interest, the minimum value of f_{ion} is about 0.3.

Because of this, recombination light from the regions of highest \mathcal{U}_{obs} is suppressed by the factor f_{ion} – so that, on a galactic scale, \mathcal{U}_{obs} is reduced relative to $\mathcal{U}_{\text{obs,max}}$. Specifically, so long as the extinction of line photons (§2.5.2) is negligible, the inferred value of \mathcal{U}_{obs} on galactic scales will be approximately the emission-weighted average of all the regions encompassed by the observation: we call this $\langle \mathcal{U}_{\text{obs}} \rangle_{\text{gal}}$. If we label a population of \mathcal{N} regions by their ionizing luminosities and apparent ionization parameters, then

$$\langle \mathcal{U}_{\text{obs}} \rangle_{\text{gal}} = \frac{\int \mathcal{U}_{\text{obs}} \{_{\text{ion}}\mathcal{S}[\mathcal{N}] d \ln S}{\int \{_{\text{ion}}\mathcal{S}[\mathcal{N}] d \ln S} = \frac{\int S^{\zeta} \langle f_{\text{ion}} \mathcal{U}_{\text{obs}} \rangle_S d \ln S}{\int S^{\zeta} \langle f_{\text{ion}} \rangle_S d \ln S}, \quad (2.23)$$

where in the second equality we assume $d\mathcal{N}/d \ln S \propto S^{\zeta-1}$ and define $\langle x \rangle_S$ to be the average of x among regions whose ionization rates lie in a narrow range around S . Galactic HII region luminosity functions obey $\zeta \simeq 0$ at high S , but are significantly shallower at lower luminosities ($S \lesssim 10^{50} \text{ s}^{-1}$, where the IMF sampling is incomplete; Kennicutt et al. 1989). Each decade of S above this break therefore contributes about equally to $\langle \mathcal{U}_{\text{obs}} \rangle_{\text{gal}}$, while those below it are increasingly insignificant.

In general, a galaxy with more massive star clusters (a population extending to higher S) and a denser circum-cluster medium (so that regions are more compact) will have regions characterized by higher values of \mathcal{U}_{obs} and therefore attain a higher $\langle \mathcal{U}_{\text{obs}} \rangle_{\text{gal}}$. However, the decline in f_{ion} accompanying the increase in $\tau_{d,\text{St}}$ suppresses the contribution of those regions with highest \mathcal{U}_{obs} . So long as the HII region population includes a range of intensities and a significant range of τ_d and f_{ion} , the net effect will be that $\langle \mathcal{U}_{\text{obs}} \rangle_{\text{gal}}$ is an underrepresentation of the starlight-weighted

average of \mathcal{U}_{obs} (the result of taking $f_{\text{ion}} \rightarrow 1$ in eq. 2.23). In particular, $\langle \mathcal{U}_{\text{obs}} \rangle_{\text{gal}}$ will be closer to the value it has when $\tau_{d,\text{St}} = 1$,

$$\frac{3}{4\gamma} \frac{2.2k_B T_i}{\bar{e}_i} = 10^{-2.25} \frac{10}{\gamma} \frac{T_4}{0.8} \frac{20 \text{ eV}}{\bar{e}_i}. \quad (2.24)$$

It is important to remember that this selection effect does not apply to individual H II regions, or parts thereof, which saturate at a higher value ($\mathcal{U}_{\text{obs,max}}$, §2.3.2). It operates only when starlight photons are distributed rather evenly across environments with a range of \mathcal{U}_{obs} and f_{ion} , so that variations of f_{ion} can affect the apparent value of \mathcal{U}_{obs} . For this reason, it does not prevent $\langle \mathcal{U}_{\text{obs}} \rangle_{\text{gal}}$ from limiting $\mathcal{U}_{\text{obs,max}}$ if *all* the H II regions in a galaxy are radiation-confined.

We demonstrate these points in Figure 2.2, for which we generate a toy model of the H II region distribution within a galaxy. We start by examining a population of 10^6 associations generated for a prior work (Matzner 2002, based on McKee & Williams 1997, in which $\zeta = 0$ at high S), extracting from it the luminosity function $d\mathcal{N}/d \ln S$ and the typical ionizing lifetime $\langle t_{\text{ion}} \rangle_S$ as functions of S . We then realize a scenario in which all H II regions expand into density profiles with $\rho \propto r^{-1}$, taking the mean column density $\Sigma = 2r\rho$ to be constant and the same for all regions. (For simplicity, we neither vary Σ with S , nor alter the upper limit of S with Σ – although both effects are likely to occur in real galaxies.) In each luminosity bin we evaluate the time evolution $\Psi(t)$ using KM09’s equation (13), which accounts for the combined force due to radiation, partially trapped winds (if any), and photo-ionized gas. We limit regions’ growth according to their finite initial size and stalling in the finite hydrostatic pressure of the environment (KM09’s § 2.3). We assume for this model that stellar winds are weak: $\log_{10} \Omega = -1.5$. With this assumption, we can construct $f_{\text{ion}}(S, t)$ and $\mathcal{U}_{\text{obs}}(S, \square)$ (from the Ne III / Ne II line ratio) using our own numerical models (§2.6). Taking the time average for $0 < t < \langle t_{\text{ion}} \rangle_S$ to get $\langle f_{\text{ion}} \rangle_S$ and $\langle f_{\text{ion}} \mathcal{U}_{\text{obs}} \rangle_S$, we arrive at $\langle \mathcal{U}_{\text{obs}} \rangle_{\text{gal}}$. For comparison we also plot the starlight-weighted averages of \mathcal{U}_{obs} , f_{ion} , and the radiation-to-gas force ratio $F_{\text{rad}}/F_{\text{tot}} = (1 + \Psi^{1/2})^{-1}$ (see KM09 eq.

10). Although the dust selection effect is not strong in our toy model, amounting to a suppression of $\langle \mathcal{U}_{\text{obs}} \rangle_{\text{gal}}$ by only $\sim 7 - 12\%$ over a relevant range of Σ , we suspect it might be more significant if some of our toy model assumptions were relaxed.

Our toy model does not account for heterogeneity of the ambient medium, which permits the existence of a diffuse ionized component; it is likely to under-estimate $\langle f_{\text{ion}} \rangle_{\text{gal}}$ and over-estimate $\langle \mathcal{U}_{\text{obs}} \rangle_{\text{gal}}$ for this reason.

2.5.2 External Dust Extinction

In the expansion of an H II region, most of the ambient medium is swept before the ionized gas rather than being ionized itself. Therefore, although dust within the H II region does not severely attenuate recombination line photons, the surrounding matter poses a thicker barrier. This external dust extinction is also an increasing function of \mathcal{U}_{obs} , as the following argument shows.

Suppose that each star cluster, of mass M , forms within an overdensity of radial profile $\rho = \rho_0 r^{-k}$, and moreover that, statistically speaking, $\rho_0 \propto M^j$. The toy model of § 2.5.1 adopted $k = 1$ and $j = 0$, but k could be as low as 0 or as high as 2, and j is likely to be positive. For the star clusters massive enough to sample the IMF, $L \propto S \propto M$.

How then does the dust optical depth of the neutral matter outside an H II region scale with \mathcal{U} within it? We restrict attention to $k > 1$, so that optical depth varies significantly with radius. When the region size is R_{IF} , the external dust optical depth at any frequency is then $\tau_{d,\text{ext}} \propto R_{\text{IF}} \rho(R_{\text{IF}}) = \rho_0 R_{\text{IF}}^{1-k}$; at the same time, the radiation pressure parameter $\Psi \propto R_{\text{IF}}/S$, so that

$$\tau_{d,\text{ext}} \propto S^{j+1-k} \Psi^{1-k} \quad (2.25)$$

for massive clusters. When $k > 1$, regions of a given S are most enshrouded when they are most radiation-dominated (i.e., when Ψ is lowest). The region luminosity

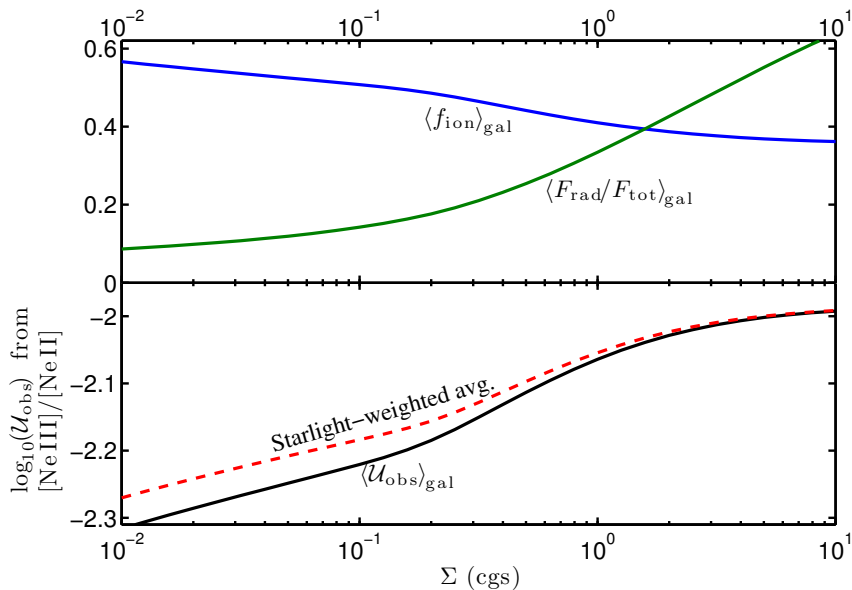


Figure 2.2: Influence of internal dust absorption on the fraction of ionizing photons caught by H atoms rather than dust ($\langle f_{\text{ion}} \rangle_{\text{gal}}$, top panel), galaxy-averaged ratio of radiation to total (gas+radiation) force ($\langle F_{\text{rad}}/F_{\text{tot}} \rangle_{\text{gal}}$, top panel) and apparent ionization parameter ($\langle \mathcal{U}_{\text{obs}} \rangle_{\text{gal}}$, bottom panel), in a toy model for a galactic population of H II regions (§2.5.1). For comparison we also plot the starlight-averaged value of \mathcal{U}_{obs} (eq. 2.23 with $f_{\text{ion}} \rightarrow 1$). In this model, the luminosity function and lifetimes of the driving associations are derived from Monte-Carlo modeling by sampling the stellar IMF (Matzner 2002). Regions expand due to a combination of radiation and photoionized gas pressures (Krumholz & Matzner 2009) in a medium of definite column density Σ , and are taken to absorb and emit light as in the numerical models of §2.6.

increases or decreases τ_d at *fixed* Ψ , depending on whether $j > k - 1$ or not. However, regions with higher S tend to also be more radiation dominated (i.e., have lower Ψ). When $j > k - 1$ it is clear that τ_d decreases as Ψ increases. Insofar as this external dust is optically thick at the frequencies of the lines being observed, this will tend to suppress emission from high- \mathcal{U}_{obs} regions, reducing this quantity relative to its theoretical maximum value. Note that, as we saw in § 2.3.2, the radiation dominated state which produces $\mathcal{U}_{\text{obs,max}}$ is in fact impossible if the column density of the ambient medium is too low.

The external attenuation of line photons is minimized by considering the longest possible transition wavelengths; we focus on mid-infrared lines in § 2.6. It should also be mitigated by holes in the swept-up neutral shell, as well as clumpiness of the ambient dust distribution (e.g., Fischera & Dopita 2005).

2.6 Numerical Models of Quasi-Static HII Regions

In this section we present numerical results for spherical, dusty, quasi-static HII regions. Our goal is to account explicitly for the possibility of an inner boundary pressure due to shocked wind (as parameterized by Ω) and to demonstrate the saturation of line ratios and inferred \mathcal{U}_{obs} due to radiation pressure confinement. We consider only a few ionizing spectra and do not vary the composition of gas or the grain population; a full exploration of these parameters is beyond the scope of this work.

We use Cloudy version 08.00, last described by Ferland et al. (1998), to account for many important microphysical effects including the photoelectric effect, collisional cooling, and the pressure due to optically thick recombination lines. However we consider only quasi-static regions in perfect force balance, and do not account for secular effects, such as grain drift, which might lead to inhomogeneities in the composition.

2.6.1 Spectral synthesis and photoionization models

Using Starburst99 (Leitherer et al. 1999), we generate the ionizing continua from coeval star clusters of different ages, all of which we assume are massive enough to fully sample the stellar initial mass function, which we take to have exponents -1.3 and -2.3 between stellar mass boundaries 0.1, 0.5, and $120 M_{\odot}$. We employ the Geneva high mass-loss evolutionary tracks with solar metallicity. These are optimized for modeling atmospheres of high mass stars and are recommended by Maeder & Meynet (1994). We adopt Pauldrach/Hillier atmospheres, as these include non-LTE and line-blanketing effects (Smith et al. 2002) for O stars (Pauldrach et al. 2001) and Wolf-Rayet stars (Hillier & Miller 1998). The combination of the Geneva high mass-loss tracks and Pauldrach/Hillier atmosphere is recommended when Wolf-Rayet stars are important (Vázquez & Leitherer 2005). Starburst99 output spectra are recorded from 0 to 11 Myr with 0.5 Myr steps.

Starburst99 output continuum spectra are fed into Cloudy as the ionizing continuum of each simulated HII region. Each HII region is spherical and in perfect force balance; we allow radiation pressure to exceed gas pressure, in contrast to Cloudy's default setting. We adopt Cloudy's default ISM abundances and dust grain size distributions. Each calculation stops where temperature drops to 100 K, and so encapsulates the IF. Each set of the simulations outputs the integrated luminosity of selected MIR emission lines from Table 2.2, including $[\text{Ar III}]_{\lambda 9.0\mu\text{m}}$, $[\text{Ar II}]_{\lambda 7.0\mu\text{m}}$, $[\text{Ne III}]_{\lambda 15.5\mu\text{m}}$, $[\text{Ne II}]_{\lambda 12.8\mu\text{m}}$, $[\text{S III}]_{\lambda 18.7\mu\text{m}}$, and $[\text{S IV}]_{\lambda 10.5\mu\text{m}}$.

2.6.2 Mapping Line Ratios to \mathcal{U}_{obs}

In both observational and theoretical studies it is necessary to translate some observed line ratios into a set of physical parameters, including \mathcal{U} ; as we have already discussed, we use \mathcal{U}_{obs} to designate the apparent \mathcal{U} which characterizes a single region. A standard definition for \mathcal{U}_{obs} is the value of \mathcal{U} at the inner boundary of an (often

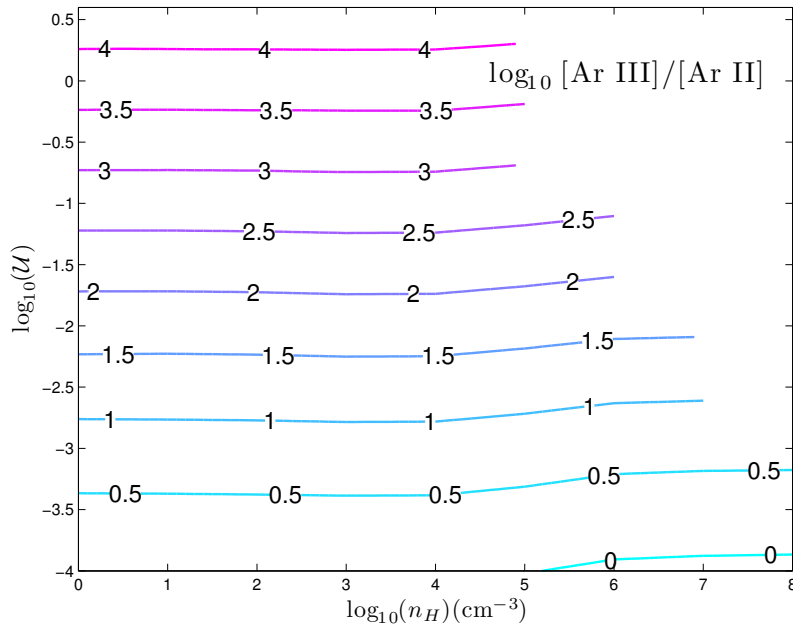


Figure 2.3: Ratio of Ar III $_{8.99\mu\text{m}}$ to Ar II $_{6.99\mu\text{m}}$ luminosities as a function of \mathcal{U} and n_H in homogeneous mixtures of solar metallicity gas with the ionizing spectrum of a fully sampled coeval star cluster at 2 Myr age. The change in line ratio across the critical densities of $2 - 3 \times 10^5 \text{ cm}^{-3}$ is clearly visible if not dramatic.

uniform) slab which reproduces the observed lines; however this has pitfalls both for low and high \mathcal{U} (§2.8), and ignores the possible role of wind pressurization. We choose instead to associate \mathcal{U}_{obs} with the value of \mathcal{U} within a *homogeneous* mixture of gas and radiation. To do so, we require a library of the line luminosities emitted by such homogeneous mixtures, in which physical parameters such as \mathcal{U} , n , and input spectrum are varied. We construct this library using the very innermost zone of a sequence of Cloudy models. Selected results are presented in figures 2.3 to 2.5. Figure 2.7 demonstrates how well the $[\text{Ne III}]/[\text{Ne II}]$ ratio reflects \mathcal{U} . Other line ratios, $[\text{Ar III}]_{\lambda 8.99\mu\text{m}}/[\text{Ar II}]_{\lambda 6.99\mu\text{m}}$ and $[\text{S IV}]_{\lambda 10.5\mu\text{m}}/[\text{S III}]_{\lambda 18.7\mu\text{m}}$, are also most sensitive to the intensity of radiation field, i.e., to \mathcal{U} .

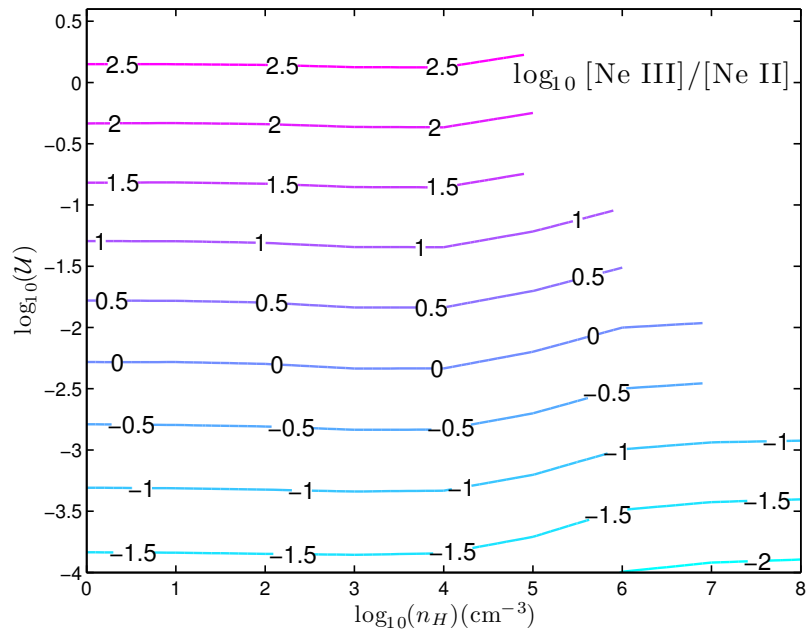


Figure 2.4: As in figure 2.3, but for Ne III $15.55\ \mu\text{m}$ / Ne II $12.81\ \mu\text{m}$.

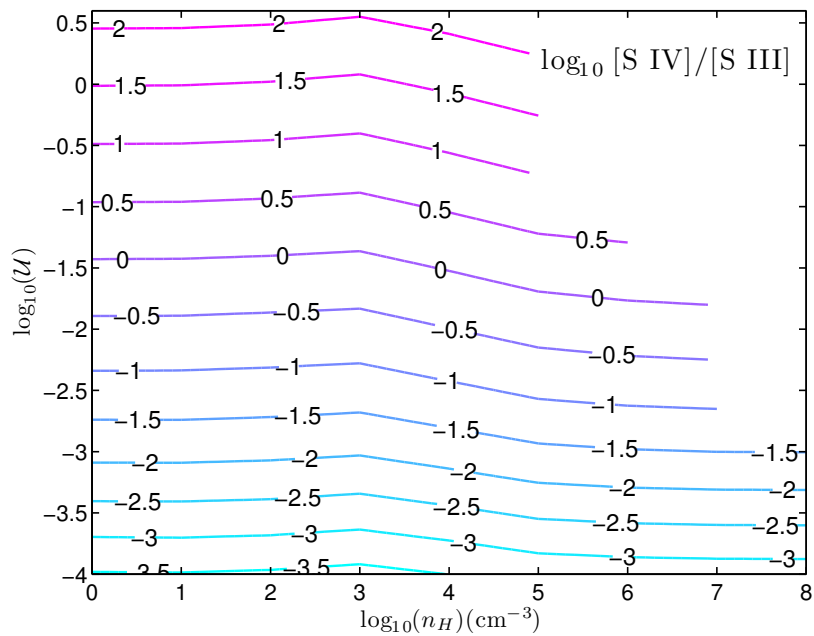


Figure 2.5: As in figure 2.3, but for S IV $10.51\ \mu\text{m}$ / S III $18.71\ \mu\text{m}$.

Table 2.3. Coeval Massive Cluster Ionizing Spectra

Age (Myr)	\bar{e}_i (eV)	L_n/L_i	β^a	$\log_{10} \sigma_d$	γ
0	20.6	0.61	0.61	-20.9	11.2
2	19.1	1.25	1.12	-20.8	13.8
4	19.2	2.81	2.51	-20.8	13.2
6	16.7	16.7	11.3	-20.7	19.3

^aFor β we list the ratio of non-ionizing to ionizing radiation *force* transferred to the dust grains by an unattenuated input spectrum, differentiating this from L_n/L_i , the definition used by Dr11.

2.6.3 Model Parameters

We work with a fixed dust population and several input spectra corresponding to fully sampled, coeval star clusters of different ages. Therefore, while the ratio β of non-ionizing to ionizing radiation force varies greatly from young (2 Myr) to relatively old (6 Myr) cluster spectra, the dust discriminant γ is almost constant. We list the relevant quantities in Table 2.3. Whenever we are not exploring age dependence, we employ spectra from 2 Myr clusters, as this is halfway through their typical ionizing lifetimes.

For each spectrum our goal is to map the line luminosities, line ratios, and resulting \mathcal{U}_{obs} as function of Ψ and Γ , i.e., to scan the parameter space displayed in Figure 2.1. Practically, we accomplish this by varying the central luminosity and innermost density of the region, at a fixed inner radius. For this study we restrict ourselves to regions with ionized densities well below the critical densities for the transitions

being considered (Table 2.2) so that density does not enter as a third parameter. Our plots in this section should therefore not be used for regions with pressures exceeding $10^8 k_B \text{ cm}^{-3}$ for [S III] and [S IV], or $10^9 k_B \text{ cm}^{-3}$ for the others. Moreover we keep the metallicity of gas and stars fixed, and vary only the age of the stellar population (rather than its IMF or other properties).

In addition to the line luminosities, we compute f_{ion} from the ratio of total H β emission to the amount of H β emission expected in the absence of dust. We also compute Sn_{em} , a useful observational diagnostic of the strength of ionization, where

$$n_{\text{em}} \equiv \frac{\int n^3 dV}{\int n^2 dV'} \quad (2.26)$$

the recombination-averaged density – a proxy for the observationally inferred density n_{obs} . For regions without internal wind bubbles, Sn_{em} determines Γ and τ_d (§2.3, Dr11); but pressurization breaks this relation.

2.6.4 Results

We begin by comparing the physical structures of a radiation-confined shell ($\log_{10} \Psi = -1.09$, $\log_{10} \Omega = -1.56$) with those of a wind-confined shell ($\log_{10} \Psi = 1.71$, $\log_{10} \Omega = 0.85$) in Figure 2.6. As expected, radiation confinement leads to a dramatic gradient of electron density and pressure, whereas wind pressure causes the region to be nearly uniform.

Figures 2.8 to 2.10 show \mathcal{U}_{obs} derived from [Ne III]/[Ne II] ratios for cluster ages 2, 4, and 6 Myr. Immediately apparent is the saturation of \mathcal{U}_{obs} in the radiation-confined state, $\log_{10} \Psi < 0$ and $\log_{10} \Omega < 0$, as is its suppression in wind-confined shells ($\log_{10} \Omega > 0$).

At age 4 Myr, the most massive stars have left the main sequence, so the ionizing flux drops and \mathcal{U}_{obs} values decrease accordingly. The pattern of saturation in the radiation-dominated quadrant is, however, unchanged.

By 6 Myr, only stars with mass $\leq 30 M_{\odot}$ are still on the main sequence, which are responsible for producing only 7.5% of the ionizing flux at zero age. Therefore \mathcal{U}_{obs} values decreased gradually comparing to that at younger ages. Note that \mathcal{U}_{obs} still saturates in the same manner as the 2 Myr and 4 Myr cases.

A second set of contours in the Ψ - Ω plots, labeled with dashed black lines, indicate $\log_{10}(Sn_{\text{em}})$. This quantity increases as Ψ decreases, which implies that dust opacity increases as radiation pressure also becomes more important. This is consistent with the analytical prediction in § 2.3. Sn_{em} values are weakly correlated with Ω in the $\log_{10} \Omega < 1$ regimes where stellar winds are negligible. Then the contours become a linear function of both Ψ and Ω when $\log_{10} \Omega > 1$.

As we have discussed in § 2.5, dust grains absorb a fraction $1 - f_{\text{ion}}$ of the ionizing photons in HII regions. We estimate f_{ion} using the ratio of total H β emission to the dust-free value H β_0 , which we calculate by assuming that all ionizing photons are used for photoionization, and each ionizing photon is responsible for one recombination. The emitted H β luminosity – which we tally zone-by-zone to avoid extinction of the line photons – reflects the suppression of ionizations due to dust absorption of starlight. The variation of H β /H β_0 with Ψ and Ω is shown in Figure 2.11 with solid blue contours, for the ionizing spectrum of a 2 Myr-old cluster. Again, dashed black contours denote $\log_{10}(Sn_{\text{em}})$, providing a calibration with respect to previous \mathcal{U}_{obs} contour plots at the same age. In the quadrant corresponding to radiation-confined shells, the H β /H β_0 line ratio is 0.35. This is consistent with our prediction, in Appendix 7.2, that f_{ion} falls to ~ 0.3 in the limit $\Psi \rightarrow 0, \Omega \rightarrow 0$ for the values of γ and β which characterize a 2 Myr cluster.

Table 2.4. Physical parameters of starburst galaxies

Object	n_e (cm ⁻³)	$\log_{10} S$ (s ⁻¹)	\mathcal{U}_{obs}	References
M82 central 500 pc	10 – 600	54.09	-2.1 – -2.6	a
NGC 253	430^{+290}_{-225}	53.00	-2.2 – -2.6	b, c, d
NGC 3256	≤ 1400	52.30 – 53.78	-2.3	e
Antennae	-1.57	f

^aFörster Schreiber et al. (2001)

^bCarral et al. (1994)

^cEngelbracht et al. (1998)

^dThornley et al. (2000)

^eRoy et al. (2005)

^fSnijders et al. (2007)

2.7 Discussion: implications of \mathcal{U}_{obs} Saturation in Starburst Galaxies

On the basis of the theory developed above, we expect to find that individual HII regions (or regions within them) display line ratios consistent with ionization parameters ranging up to the maximum value corresponding to radiation confinement. Although the same physical process limits the inferred ionization parameter for observations on galactic scales, the value of the upper limit is not the same, because of the different measures used: usually geometric estimates (our $\mathcal{U}_{\text{geom}}$) in resolved regions, as opposed to pure line ratios (our \mathcal{U}_{obs} , or more precisely $\langle \mathcal{U}_{\text{obs}} \rangle_{\text{gal}}$) in unresolved ones. Moreover, averaging over many regions tends to blend together those at $\mathcal{U}_{\text{obs,max}}$ with those below it, and the selective dimming of high- \mathcal{U}_{obs} regions by internal dust absorption favors those below the maximum.

We estimate the upper limit of $\mathcal{U}_{\text{geom}}$ to be roughly 10^{-1} using the solutions of Appendix 7.2, by replacing $n_{i,\text{obs}}$ with the emission-weighted density n_{em} . This is only approximate, as it does not account for the formation of the lines used to derive $n_{i,\text{obs}}$. For unresolved regions we apply $\mathcal{U}_{\text{obs,max}}$, in which we do account for line formation: because most of the observations employ the the [Ne III]/[Ne II] line ratio of figure 2.8, we apply the upper limit of $10^{-1.97}$ we found there. Part of the difference between the two upper limits can be seen in the internal structure of radiation-confined zones, in which Ξ_{geom} is about 0.3 dex higher than the recombination-weighted average $\Xi_{i,\text{em}}$. The rest of the difference is presumably due to the details of line formation.

To test these expectations against observed regions, we plot in Figure 2.12 a sample of observationally-derived ionization parameters from the literature, divided according to the scope of the observations involved and according to the method used. As expected, the data range up to values which are approximately our estimated maximum value for each method. For individually-resolved regions, the observed

upper limit appears to be somewhat higher than our prediction, but we attribute this to the approximate nature of our $\mathcal{U}_{\text{geom,max}}$ (rather than to magnetic fields, say). For galactic-scale observations highest \mathcal{U}_{obs} is slightly lower than our $\mathcal{U}_{\text{obs,max}}$, which could be a product of the averaging process.

These results in hand, we turn to the importance of wind pressure in H II regions.

For a resolved, spherical H II region with well-constrained observations of S , n_e , and \mathcal{U}_{obs} , it is possible to estimate the wind parameter Ω by reference to a plot like our Figure 2.8. With only \mathcal{U}_{obs} or $\mathcal{U}_{\text{geom}}$, one obtains an upper limit on Ω . By this logic, we can state quite firmly that the wind parameter Ω is often small in resolved H II regions: otherwise, our example values of \mathcal{U}_{obs} in the upper panel of Figure 2.12 would be much less than the theoretical maximum.

The same argument applies, if somewhat more weakly, to entire galaxies: for them, $\log_{10} \mathcal{U}_{\text{obs}}$ ranges up to about -2.3 . This is far higher than what would be possible if they were adiabatic wind bubbles (Eq. 2.16) unless they are exceptionally weak. This can be seen, for instance, in Figure 2.8, where we use the values of $\langle \mathcal{U}_{\text{obs}} \rangle_{\text{gal}}$ and the product of *total* S and inferred $n_{i,\text{obs}}$ to place several starburst galaxies within the parameter space of individual H II regions. Because this is an upper limit on the actual values of $S n_{\text{em}}$ within each galaxy's H II regions, and because $\langle \mathcal{U}_{\text{obs}} \rangle_{\text{gal}}$ cannot be higher than the typical values of \mathcal{U}_{obs} in those regions, we infer that the characteristic values of $\log_{10} \Omega$ cannot exceed about 0.25.

While wind-dominated bubbles are likely to exist, we find no evidence for them either in individual regions or on galactic scales. We conclude from this that the leakage of wind energy past the IF, either by advection or radiation, is significant.

2.8 Conclusions

Our primary motivation in this study has been to assess whether the ionization parameter can be used to measure the importance of radiation pressure in the inflation

of HII regions in external galaxies, especially starburst galaxies. We have been interested in how well the observational estimate \mathcal{U}_{obs} reflects the radiation-to-gas pressure ratio Ξ in local conditions and its average over galactic scales. Because $\Xi \propto \mathcal{U}$ in each parcel of gas, and because \mathcal{U} controls the ionization state and therefore the emitted spectrum, it is possible, in principle, to derive the role of photon momentum in the kinematic feedback from young star clusters into the nearby dense neutral gas. (Although supernovae tend to inject more energy, they are thought to couple very poorly to dense, star-forming gas; Matzner 2002.) Because emission line ratios reflect local conditions, this information would be complementary to the global analysis of Andrews & Thompson (2011). To this end we explored the properties of strongly radiation-confined layers using the analytical theory of Dr11 (Appendix 7.2), considered a host of physical effects and scenarios which could affect \mathcal{U}_{obs} in real regions (§ 2.4 and § 2.5), and engaged in a suite of numerical models of dusty HII regions in quasi-static force balance with an interior pressurized wind bubble (§ 2.6). Our models, though not meant to probe the full parameter space of HII regions, are the first to explore a wide range of both the radiation force parameter (Γ or Ψ) and the wind pressure parameter (Ω).

Two effects complicate our plan to measure radiation pressure feedback using the apparent ionization parameter.

First is the fact that strongly radiation-dominated regions compress their ionized gas into thin layers whose internal pressure gradient balances the radiation force (Binnette et al. 1997). The ionization parameter recorded in any line ratio reflects the ratio of radiation to gas pressure where the lines are produced, and in radiation-confined regions \mathcal{U}_{obs} saturates at a maximum value. The resulting values of $\log_{10} \mathcal{U}_{\text{obs,max}}$ depend on the lines in question (§ 2.6) and parameters such as the dustiness of the region and the ionizing spectrum, but are roughly ~ -1.5 , the value for which $\Xi \simeq 1$. For the particular neon line ratio plotted in Figure 2.8, the upper limit is actually -1.97 .

Only significant levels of ram pressure or magnetic pressure, or serious departures from force balance, allow for \mathcal{U}_{obs} to exceed this putative maximum (§2.4.3-2.4.4), and this point may be useful in diagnosing the physical states of unresolved regions. Conversely any significant pressure on its inner boundary, such as the pressure due to shocked stellar winds, reduces Ξ and \mathcal{U}_{obs} (as well as the dust optical depth τ_d) below their maximal values (§ 2.4.1). Our limited compilation of ionization parameters in individual regions (figure 2.12, top panels) is consistent with the proposition that \mathcal{U}_{obs} varies up to the maximum imposed by radiation confinement; for instance, Snijders et al. (2007) find $\log_{10} \mathcal{U}_{\text{obs}} = -1.57$ in individual regions in the Antennae Galaxies.

Another complicating effect is the suppression of the apparent ionization parameter on galactic scales by selective dust absorption of ionizing photons in the regions where \mathcal{U} is highest. Gas in the local Universe is sufficiently dusty ($\gamma \simeq 10$) that the dust optical depth τ_d exceeds the radiation-to-gas pressure ratio Ξ , both of which vary proportionally to \mathcal{U} : all radiation-confined regions (and some others) are dust-limited. Such dust-limited regions convert a large portion of the stellar ultraviolet radiation into far infrared continuum, limiting the efficiency f_{ion} of line production. For observations which span a wide range of local conditions, this biases the inferred estimate of \mathcal{U} (which we call $\langle \mathcal{U}_{\text{obs}} \rangle_{\text{gal}}$ in this case) toward regions of lower $\tau_d \leq 1$ and \mathcal{U}_{obs} .

Within the toy model for galactic HII region populations we present in §2.5.1, it appears this selection effect suppresses $\langle \mathcal{U}_{\text{obs}} \rangle_{\text{gal}}$ by a small amount (< 0.05 dex) relative to an unbiased (i.e., starlight-weighted) average of \mathcal{U}_{obs} , primarily because the line efficiency f_{ion} gradually declines by only 0.5 dex (to a minimum of about 0.35) as radiation confinement becomes strong. Although this result depends on the assumptions in our toy model, it strongly suggests that $\langle \mathcal{U}_{\text{obs}} \rangle_{\text{gal}}$ can be corrected for selective absorption and used to infer the physical characteristics of the galactic HII region population. Chief among these would be the ratio of radiation and gas-pressure forces averaged over a galaxy's ionized zones, a quantity we plot (for the toy model)

in the top panel of figure 2.2.

It has long been appreciated that the dust-bounded state contributes to the suppression of fine-structure cooling lines relative to the far-infrared continuum in ULIRGs (Voit 1992; Bottorff et al. 1998; Abel et al. 2009), and that recombination luminosity under-represents the ionizing luminosity in this state;

these effects provide observational checks on the degree of dust saturation one might infer from recombination line ratios.

The galaxies collected in the bottom panel of figure 2.12 display an upper limit of $\log_{10} \langle \mathcal{U}_{\text{obs}} \rangle_{\text{gal}} \simeq -2.3$, with some uncertainty. This is very close to the upper limit of -1.97 we found for \mathcal{U}_{obs} derived from a $[\text{Ne III}]/[\text{Ne II}]$ line ratio in young H II regions (§2.6), especially considering the bias induced by dust attenuation. We infer, therefore, that radiation pressure strongly modifies the ionized zones in these galaxies.

A result of dust-induced bias is that the upper limit of $\langle \mathcal{U}_{\text{obs}} \rangle_{\text{gal}}$ will be weakly anti-correlated with metallicity. To test this, one must disentangle variations in \mathcal{U} from variations in the incident spectrum due to changes in stellar metallicity, and possible influences of metallicity on the stellar initial mass function (and more subtly, on stellar rotation and multiplicity).

Moreover, our analysis of the radiation-confined state (Appendix 7.2) suggests a change in the properties of radiation-confined H II regions with metallicity above and below about $\log_{10}(Z/Z_{\odot}) = -1.2$,⁵ corresponding to $\gamma = 1$. For higher values of γ , as we have already mentioned, dust absorption is significant in all radiation-confined zones. Further, for $\gamma > 1$ radiation-confined zones are compact (the density scale height is much smaller than the radius) and the Lyman- α line pressure is negligible. None of these is true for $\gamma < 1$: regions with significant radiation pressure extend inward toward the central source, are supported by line pressure as well as gas pressure, and are not significantly attenuated by dust. Moreover, the wind pressure

⁵Estimated assuming $T \propto Z^{-0.2}$, $\bar{e}_i \propto Z^{-0.04}$, and $\sigma_d \propto Z$.

will typically be lower on account of the lower opacity of stellar atmospheres. We leave a full investigation of this transition to future research, but point out that many works on photo-ionization in active galactic nuclei have been carried out in the limit $\gamma = 0$.

We firmly rule out the hypothesis that resolved H II regions are predominantly the ionized shells of energy-conserving wind bubbles (as envisioned for giant H II regions by Oey & Clarke 1997). The pressure of shocked winds in such models lowers \mathcal{U} well below observed values. Although this discrepancy can be remedied by decimating the wind luminosity (Dopita et al. 2005), it is more natural to attribute the reduction in wind pressure to leakage of hot gas beyond the ionization front, either via direct outflow or radiative losses. It is preferable to employ models which explicitly account for such leakage (Harper-Clark & Murray 2009, KM09). Such models form the basis for populations of H II regions in the toy model of §2.5.1 and in a future companion paper (Verdolini et al. in prep., also see Chapter 3), in which line emission by star-forming galaxies will be reconsidered in greater detail than is possible here.

It is possible to interpret entire galaxies in terms of models of individual H II regions, as we discussed in §2.7. This must be done with caution, because observations on galactic scales must necessarily average over a wide range of conditions, and are biased by dust absorption. Acknowledging this, one can nevertheless derive an effective upper limit on the wind pressurization Ω from the fact that a larger value of this parameter would limit $\langle \mathcal{U}_{\text{obs}} \rangle_{\text{gal}}$ below what is observed.

For observational and theoretical studies of the ionization parameter, an important point is that the method used to infer \mathcal{U}_{obs} affects the result, leading to systematic offsets between methods. Traditionally line ratios are compared with suites of simulations in which \mathcal{U}_{obs} represents the interior of an ionized layer (often one of uniform density), a definition which corresponds to our $\mathcal{U}_{\text{geom}}$ so long as the layer is thin. This definition encounters a couple difficulties. First, the incident flux is attenuated by

recombination and dust within the layer so that the characteristic value of \mathcal{U} is lower than the incident value (e.g., equation [2.16]). Second, ionized gas can only be confined to a thin layer by an inner, pressurized region of hot gas, or (when $\gamma > 1$) by strong radiation pressure; however, radiation confinement introduces a pressure and density gradient within the confined layer, and wind confinement limits the maximum values of Ξ and \mathcal{U} well below unity and 0.1, respectively. For these reasons, uniform-slab calculations are physically inconsistent at high values of \mathcal{U} . It is preferable to use suites of simulations involving spherical HII regions in quasi-static force balance, but a single sequence of these excludes the role of a wind pressurization parameter (our Ω).

As an alternate standard, we advocate using, for \mathcal{U}_{obs} , the value of \mathcal{U} within a uniform mixture of gas photons for which the emitted line ratios match those observed.

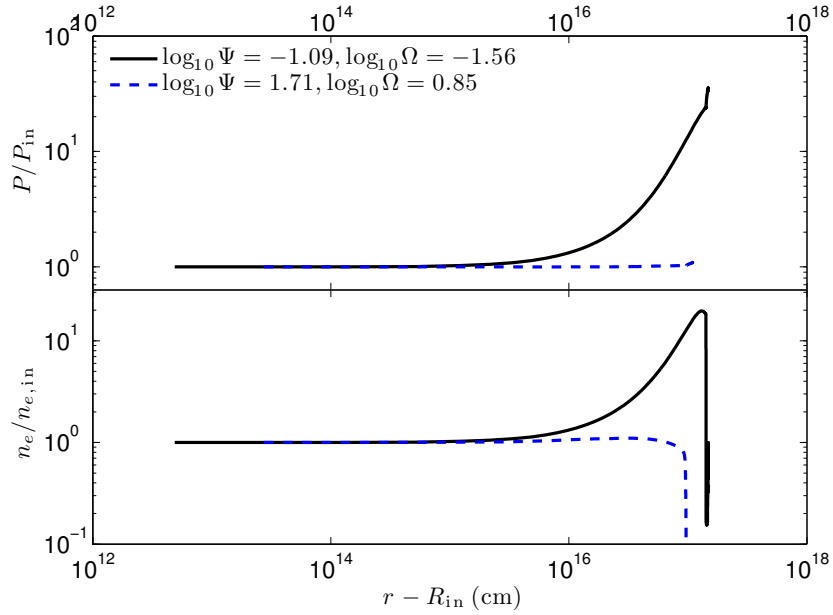


Figure 2.6: Normalized pressure (top) and electron density (bottom) profiles of HII regions, showing the structure of radiation pressure dominated (solid) and wind bubble (dashed) regimes, which were illuminated by the ionizing spectrum of a 2 Myr cluster of $10^{42} \text{ erg s}^{-1}$ and $10^{39} \text{ erg s}^{-1}$ luminosity, respectively. A drop in temperature beyond the ionization front leads to an increase in density which outpaces the declining ionization fraction, causing an uptick in n_e in the outermost zones.

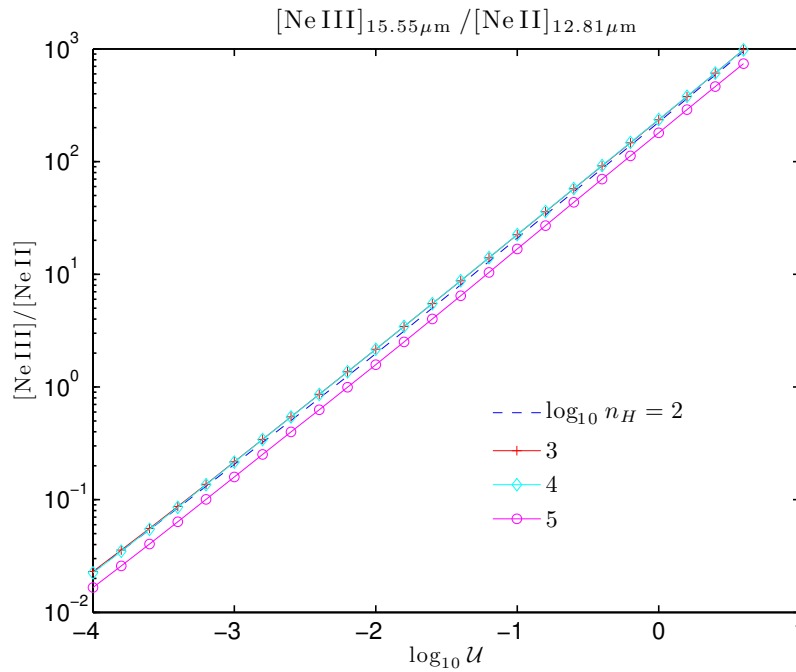


Figure 2.7: One-zone $[\text{Ne III}]/[\text{Ne II}]$ line ratio at various values of $\log_{10} \mathcal{U}$, for hydrogen density $\log_{10} n_H = 2, 3, 4, 5$ (blue dashed line, red crossed line, cyan line with diamonds, magenta line with circles, respectively). Metallicity and ionizing spectrum are held fixed: Z_{\odot} and the spectrum of a 2 Myr cluster. The $[\text{Ne III}]/[\text{Ne II}]$ ratio is sensitive to \mathcal{U} and insensitive to n_H , falling only 37% for densities which approach the critical density of the $[\text{Ne II}]$ line.

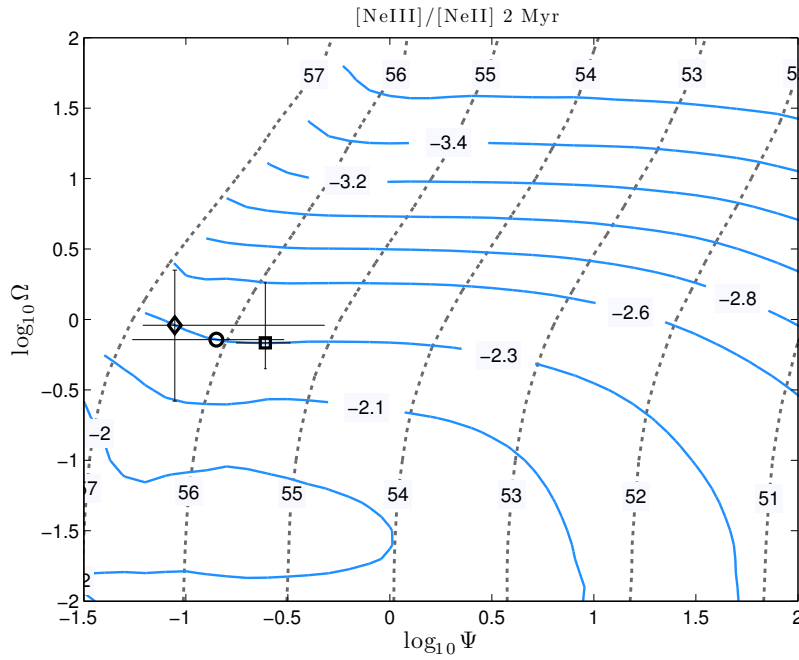


Figure 2.8: Logarithm of ionization parameter (solid blue contours) as a function of $\log_{10} \Psi$ and $\log_{10} \Omega$, for illumination by a 2 Myr-old cluster. The $\log_{10} \mathcal{U}_{\text{obs}}$ values are evaluated from the line ratio $[\text{Ne III}]_{\lambda 15.55 \mu\text{m}}/[\text{Ne II}]_{\lambda 12.81 \mu\text{m}}$. Dashed black contours denote the logarithm of $S n_{em}$. HII region of the central 500 pc of M82, NGC 3256, and NGC 253, are marked by open diamond, circle, and square, respectively. The maximum value corresponds to $\mathcal{U}_{\text{obs,max}} = -1.97$.

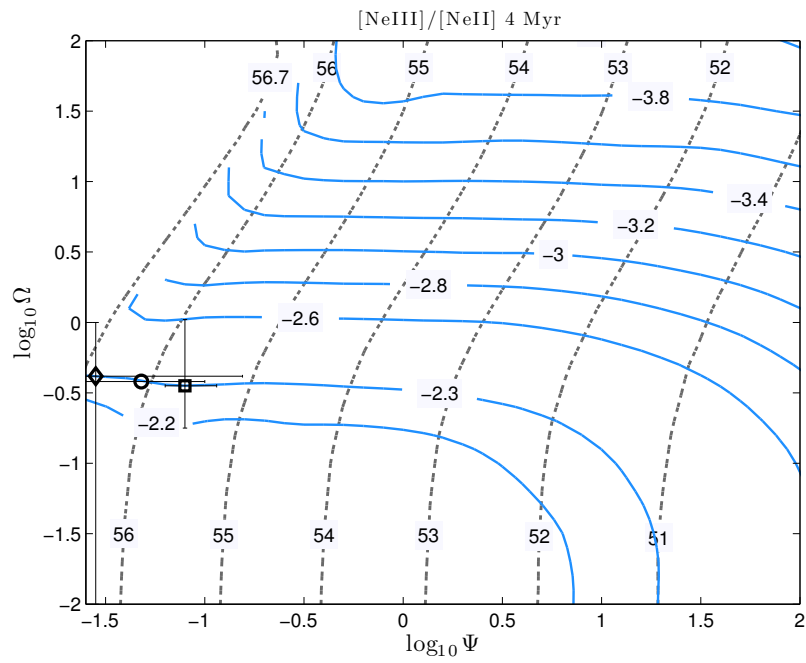


Figure 2.9: Same as in Figure 2.8, but for ionization by a star cluster of age 4 Myr. The $\log_{10} \mathcal{U}_{\text{obs}}$ values are evaluated from the line ratio $[\text{Ne III}]_{\lambda 15.55 \mu\text{m}} / [\text{Ne II}]_{\lambda 12.81 \mu\text{m}}$. Symbols that mark H II regions of M82, NGC 3256, and NGC 253, are the same as in Figure 2.8.

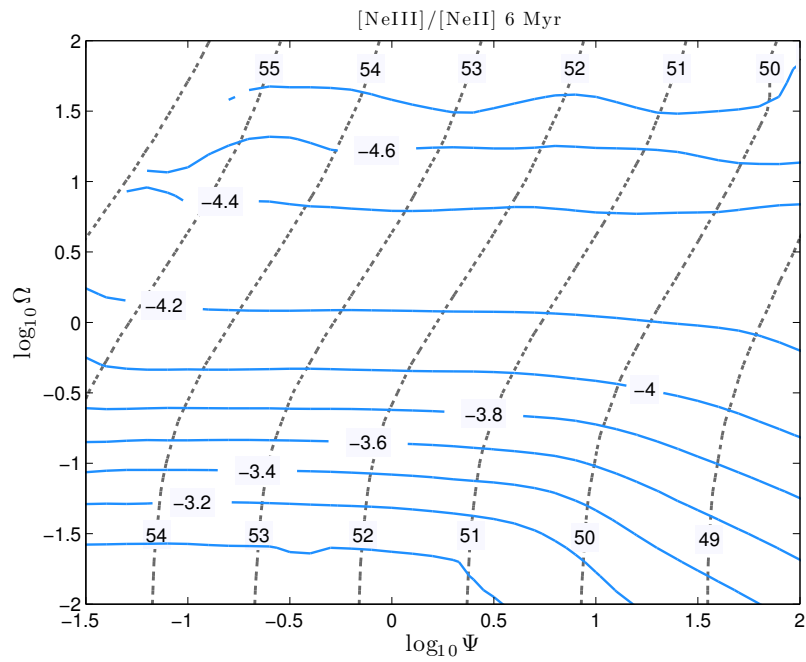


Figure 2.10: As in Figure 2.8, for ionization by a star cluster of 6 Myr age. Values of $\log_{10} \mathcal{U}_{\text{obs}}$ are evaluated from the line ratio $[\text{Ne III}]_{\lambda 15.55 \mu\text{m}}/[\text{Ne II}]_{\lambda 12.81 \mu\text{m}}$.

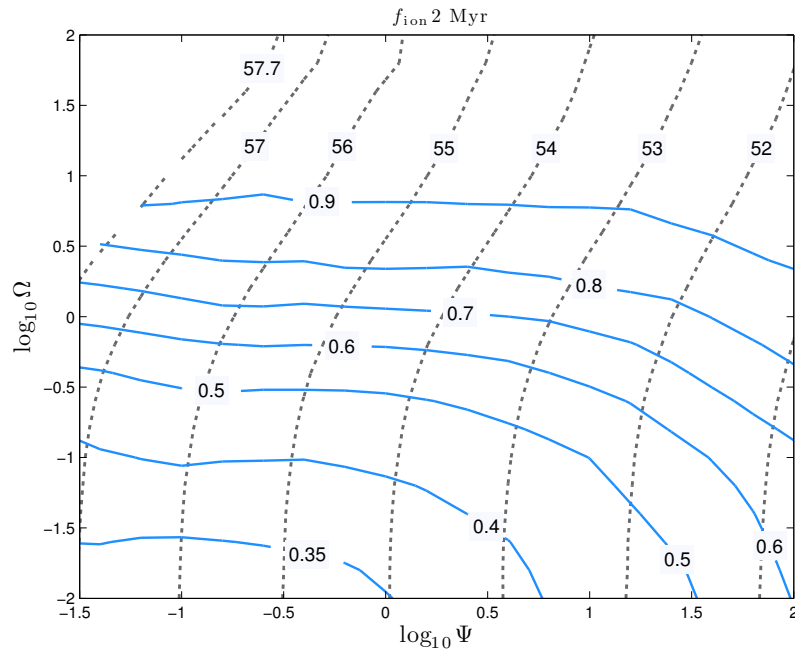


Figure 2.11: Solid blue contours mark f_{ion} , calculated as the ratio of the $\text{H}\beta$ line to $\text{H}\beta_0$, its value in the absence of dust, as a function of $\log_{10} \Psi$ and $\log_{10} \Omega$. Dashed black contours label $\log_{10}(S n_{\text{em}})$ as in previous figures. The ionizing spectrum corresponds to a star cluster age of 2 Myr.

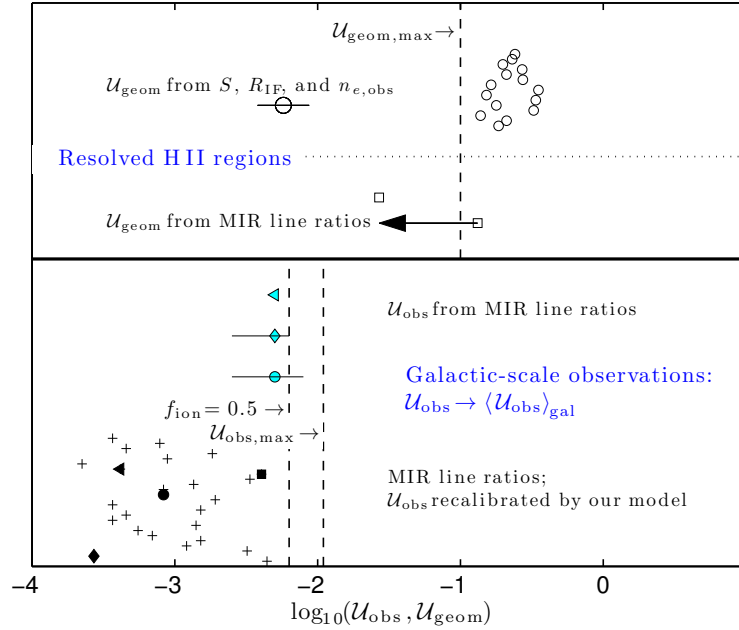


Figure 2.12: Samples of individual H II regions and galactic-scale regions, plotted and divided into groups according to how \mathcal{U}_{obs} is estimated. The thick horizontal line divides individual regions (upper portion) and galactic-scale regions (lower portion). We further distinguish the individual regions into two categories, based on whether \mathcal{U} is estimated geometrically ($\mathcal{U}_{\text{geom}} = S/(4\pi R_{\text{IF}}^2 n_{e,\text{obs}} c)$) or inferred from observed line ratios. Vertical dashed lines indicate theoretical maximum values $\mathcal{U}_{\text{geom,max}}$ (Appendix 7.2, estimated from $\max(\Xi_{i,\text{geom}})$) and $\mathcal{U}_{\text{obs,max}}$ (from $[\text{Ne III}]/[\text{Ne II}]$, figure 2.8), as well as the value of \mathcal{U}_{obs} at which dust absorption becomes significant in the sense that $f_{\text{ion}} = 0.5$ in individual young regions with our fiducial parameters (Figure 2.8). Open circles – single H II regions in M82, McCrady & Graham (2007); Large open circle – H II region M82-A1, Smith et al. (2006); Open squares – resolved H II regions in the Antennae Galaxies, Sijnders et al. (2007); Cyan and black left-pointing triangle – NGC 3256, Thornley et al. (2000); Cyan and black diamond – NGC 253, Thornley et al. (2000); Cyan and black circle – the central 500 pc starburst region of M82, where the bar indicates the possible range of $\log_{10}\mathcal{U}_{\text{obs}}$ modeled by Förster Schreiber et al. (2003); crosses – recalibrated $\log_{10}\mathcal{U}_{\text{obs}}$ values of the galaxies in Thornley et al. (2000). Sijnders et al. (2007) report a value which corresponds to our $\mathcal{U}_{\text{geom}}$, so we apply the approximate upper limit on this quantity.

Chapter 3

Line Emission from Radiation-Pressurized HII Regions: Internal Structure and Line Ratios

3.1 Chapter Overview

The emission line ratios $[\text{O III}]_{\lambda 5007}/\text{H}\beta$ and $[\text{N II}]_{\lambda 6584}/\text{H}\alpha$ have been adopted as an empirical way to distinguish between the fundamentally different mechanisms of ionization in emission-line galaxies. While most HII regions in local galaxies can be reasonably well distinguished from AGNs, high-redshift star-forming galaxies show unusual offsets in the emission line diagnostics. We carried out quasi-static HII region models to explore the parameter space they map using the same emission line diagnostics, and found that more realistic HII regions, which includes radiation pressure and stellar winds, cannot have arbitrarily high ionization parameter values. Our quasi-static HII region modeling is part of the collaborative work with Verdolini et al. (2012 in prep.), in which the dynamical evolution of HII regions are accounted for and meant to represent the entire galaxies in high redshift.

3.2 Introduction

The diagnostics $[\text{O III}]_{\lambda 5007}/\text{H}\beta$ and $[\text{N II}]_{\lambda 6584}/\text{H}\alpha$ diagram, first proposed by Baldwin et al. (1981) (hereafter BPT), is commonly adopted to distinguish emission-line objects and origins of emission line excitation, such as H II region-like galaxies and active galactic nuclei (AGNs). These emission line pairs are chosen because (1) they are bright emission lines and easy to measure in galaxies, (2) blending between the lines can be corrected with reasonable accuracy, so long as the spectra are taken with sufficient resolution, (3) the wavelengths in each line pair are quite similar, so the line ratio is less sensitive to reddening, and (4) the combination of single-element forbidden line and an HI Balmer line is less sensitive to abundances (Veilleux & Osterbrock 1987). Emission-line galaxies can be empirically distinguished on such a BPT diagram, with H II region-like galaxies located at the regime where $[\text{O III}]_{\lambda 5007}/\text{H}\beta$ and $[\text{N II}]_{\lambda 6584}/\text{H}\alpha$ ratios are lower and AGNs located at the higher line ratio regime, due to fundamentally different ionization mechanisms.

When the ionizing flux is produced by photoionization of hot stars, the $[\text{O III}]$ and $[\text{N II}]$ intensities are functions of the radiation field hardness and intensity, which are determined by the effective temperature of the stars $T_{*,\text{eff}}$ and ionization parameter \mathcal{U} . The ionizing flux decreases with $T_{*,\text{eff}}$ and \mathcal{U} , therefore the O^{++} zone size becomes smaller and the $[\text{O III}]$ intensity also drops. At a given decrease of $T_{*,\text{eff}}$ and \mathcal{U} , singly ionized species such as N^+ become the major species that fill the ionized zone. Therefore the $[\text{N II}]$ line intensity becomes steadily higher when the $[\text{O III}]$ line intensity drops. On the other hand, if the ionizing spectrum follows a power-law (ν^α), when the ionizing power becomes higher (smaller α), ionization by X-ray photons is more important and both $[\text{O III}]$ and $[\text{N II}]$ intensities increase. Therefore qualitatively, since L_i produced by a power-law ionization is more capable of ionizing species of higher ionization potential than the L_i of photoionization produced by hot stars, H II regions will show relatively lower line ratios of $[\text{O III}]/\text{H}\beta$ and $[\text{N II}]$

$]/H\alpha$, while AGNs show higher line ratios, placing the two types of objects on the lower left and upper right regime of the BPT diagram, respectively.

The local star-forming SDSS galaxies (with median redshift $z=0.1$) seem to obey a tight correlation between the $[O\text{III}]/H\beta$ and $[N\text{II}]/H\alpha$ ratios on the BPT diagram (Brinchmann et al. 2008; Liu et al. 2008), whereas higher redshift star-forming galaxies are offset to the regime where the $[O\text{III}]/H\beta$ is higher but not quite in the AGN regime, and these galaxies do not show significant correlations in the BPT diagram (e.g., Shapley et al. 2005 and Erb et al. 2006). This suggests that H II regions in high redshift star-forming galaxies may have properties fundamentally different from H II regions in local galaxies. While the current observational studies cannot rule out contaminations from AGNs or shock excitation to this unusual offset of emission-line diagnostic (e.g., Liu et al. 2008), in Chapter 2 we have pointed out that radiation pressure changes the H II region density structure, leading to saturation of observed \mathcal{U} and characteristic line ratios in starburst galaxies. This demonstrates the importance of understanding detailed H II region physical conditions, if one is going to infer physical properties of star-forming galaxies using emission-line diagnostics.

Verdolini et al. (2012 in prep., hereafter V12) investigate the detailed H II region physical conditions, using sophisticated dynamical models to construct BPT diagrams of expanding H II regions, which are meant to represent the entire galaxies. V12 aim to understand the effects of detailed H II region physical conditions in high redshift galaxies, such as their densities, ages, radiation pressure, and stellar wind pressure, in offsetting the galaxies in the BPT diagram. In this chapter, we describe the quasi-static H II region models which contribute to the V12 work, and we focus on the more fundamental analysis of the BPT diagram and our quasi-static H II regions models which is currently separate from the V12 work. The quasi-static H II region models are described in § 3.3, and we compare our quasi-static H II region models with other modeling efforts in the BPT diagram in §3.4. The implications drawn from our model

results on the BPT diagram are elaborated in § 3.5. We defer the full study of HII region dynamical models to V12.

3.3 Photoionization Models

A population of static, single HII regions, with a wide range of sizes and ionizing luminosities (L_i), are generated by spectral synthesis code Starburst99 (Leitherer et al. 1999) and photoionization code Cloudy 08.00, last described by Ferland et al. (1998). Because input parameters in photoionization models can vary from model to model, to enable a meaningful comparison between our model and others, such as the Dopita et al. 2000 (D00) model and the Levesque et al. 2010 (L10) model, we adopted the input parameters as close as possible to those of D00’s parameters. Tabel 3.1 summarizes the parameters of the different models.

We first used Starburst99 (Leitherer et al. 1999) to generate ionizing continua from coeval star clusters of different ages. We assumed that all of the clusters are massive and fully sample the stellar initial mass function, which we take to have exponents -1.3 and -2.3 between stellar mass boundaries 0.1, 0.5, and 120 M_{\odot} . We employed the Geneva standard evolutionary tracks (Charbonnel et al. 1996; Schaerer et al. 1993a;b; Schaller et al. 1992) with solar metallicity; Lejeune-Schmutz stellar atmospheres (Lejeune et al. 1997; 1998; Schmutz 1998), which incorporate plane-parallel atmospheres and stars with strong winds, are adopted in our Starburst99 calculations. Starburst99 output spectra are recorded from 0 to 11 Myr with 0.5 Myr steps.

Starburst99 output continuum spectra are fed into Cloudy as the ionizing continuum of each simulated HII region. Each HII region is spherical and in perfect force balance, although in some cases we neglect the radiation force to test its effect. We adopted Cloudy’s default solar abundances and ISM dust grain size distributions, but adjust the gas phase abundances to match the settings in D00. Each HII region

calculation stops where temperature drops to 100 K, so the ionization front is well encapsulated. A wide range of density grids¹ $\log_{10} n_{H,in} = 1$ to 5 is computed. Each set of the simulations outputs the integrated luminosity of selected optical emission lines, including $H\alpha$, $H\beta$, $[\text{O III}]_{\lambda 5007}$, and $[\text{N II}]_{\lambda 6584}$, the emission line diagnostics used in the BPT diagram.

We computed four sets of H II region models, which are defined by the radiation pressure parameter Ψ and stellar wind parameter Ω :

Model 1: $\log_{10} \Psi < 0$, $\log_{10} \Omega = -2$; radiation pressure dominated and stellar wind pressure is negligible;

Model 2: $\log_{10} \Psi < 0$, $\log_{10} \Omega = 2$; stellar wind dominated with the presence of radiation pressure;

Model 3: $\log_{10} \Psi > 0$, $\log_{10} \Omega = -2$; radiation pressure neglected and wind pressurization negligible;

Model 4: $\log_{10} \Psi > 0$, $\log_{10} \Omega = 2$; stellar wind dominated and radiation pressure is neglected.

The parameters Ψ and Ω follow the same definitions in Chapter 2 :

$$\Psi \equiv \frac{R_{\text{IF}}}{\tilde{r}_{\text{ch}}} , \quad (3.1)$$

where R_{IF} is the actual ionization front (IF) radius of each H II region, \tilde{r}_{ch} is the characteristic radius where its gas pressure equals the total unattenuated radiation pressure; and

$$\Omega \equiv \frac{P_{\text{in}} V_{\text{in}}}{P_{\text{IF}} V_{\text{IF}} - P_{\text{in}} V_{\text{in}}} , \quad (3.2)$$

where $P_{\text{IF}} V_{\text{IF}} - P_{\text{in}} V_{\text{in}}$ is the difference of the product of pressure and volume between the IF and the inner edge of the HII region, which is the outer edge of a pressurized bubble.

¹This density refers to the density at the inner boundary of each HII region.

See Table 2.1, § 2.3, and § 2.3.3 in Chapter 2 for detailed discussion of Ψ and Ω . In Model 1 and Model 2, radiation pressure is accounted for, and is allowed to exceed ionized gas pressure, in contrast to Cloudy’s default setting. On the other hand, the continuum radiation pressure is neglected in Model 3 and Model 4.

3.4 Cloudy Model Results and Discussion

3.4.1 Mapping \mathcal{U} to the BPT Diagram

Before we discuss the results of our four HII models in detail, we first demonstrate how \mathcal{U} values of photoionized regions vary on the BPT diagram. The \mathcal{U} values are calculated using the inner most zone of a sequence of our Cloudy models, which has a homogeneous mixture of gas density and radiation. The ionizing spectrum and metallicity of the stars and gas are fixed to 0 Myr and solar metallicity. The \mathcal{U} contours as a function of gas density (in this case $\log_{10} n_{H,in} = \log_{10} n_H$), are shown in Figure 3.1. The \mathcal{U} contours are shown in black solid lines, while the $[\text{O III}]/\text{H}\beta$ and $[\text{N II}]/\text{H}\alpha$ ratios as a function of density grids are shown in blue dashed lines. At a fixed radiation field hardness, photoionized regions occupy the lower left regime of the BPT diagram. \mathcal{U} shifts from the upper left to the lower right in the BPT diagram as a function of L_i , which agrees with the predicted behavior for a photoionized region. On the other hand, the $[\text{O III}]/\text{H}\beta$ and $[\text{N II}]/\text{H}\alpha$ contours shift from lower left to upper right in the BPT diagram as a function of density, then gradually decreases and moves towards the opposite direction when the gas density exceeds 10^4 cm^{-3} . This is because that the critical densities of $[\text{N II}]$ and $[\text{O III}]$ emission lines are $6.6 \times 10^4 \text{ cm}^{-3}$ and $6.8 \times 10^5 \text{ cm}^{-3}$, respectively, naturally the line intensities decrease dramatically when the gas density exceeds the species’ critical densities. While our models and others (Kewley et al. 2001; Levesque et al. 2010) demonstrated that for a given ionizing spectrum and metallicity, there is a unique mapping between the line ratios (or the

Table 3.1. Comparison of Model Parameters

	Dopita et al. 2000 Model	Our Model	Levesque et al. 2010 Model
Ionizing Spectra	Starburst99	Starburst99	Starburst99
Initial Mass Function	Salpeter, $M_{up} = 120 M_{\odot}$	Default Starburst99 IMF ^a , $M_{up} = 120 M_{\odot}$	Salpeter, $M_{up} = 100 M_{\odot}$
Stellar Tracks	Geneva standard	Geneva standard	Geneva high mass-loss
Stellar Atmospheres	Lejeune-Schmutz	Lejeune-Schmutz	Pauldrach/Hillier
Photoionization Code	MAPPINGS v3.0	Cloudy v08.00	MAPPINGS III
Radiation Pressure	Not included	Optional	Included
Geometry	Plane-Parallel	Spherical	Plane-Parallel
H II Region State	Isobaric	Force balanced	Isobaric
Metallicity	Solar	Solar	Solar
Gas Phase Abundances			
H	0	0	0
He	-1.01	-1.01	-1.01
C	-3.74	-3.74	-3.70
N	-4.17	-4.17	-4.22
O	-3.29	-3.29	-3.29
Ne	-3.91	-3.91	-3.91
Mg	-5.12	-5.12	-5.12
Si	-5.45	-5.45	-5.45
S	-4.79	-4.79	-5.19
Ar	-5.44	-5.44	-5.44
Ca	-8.16	-8.16	-8.16
Fe	-6.33	-6.33	-6.33

^aIMF exponents: 1.3 and 2.3 at mass boundaries 0.1, 0.5, and $120M_{\odot}$.

Table 3.2. Optical Emission Lines on the BPT Diagram

Line	Wavelength (Å)	n_{cr} (cm ⁻³) ^a
H β	4861	...
[OIII]	5007	6.8×10^5
H α	6563	...
[NII]	6584	6.6×10^4

^aCritical densities for collisional excitation; Osterbrock & Ferland (2006)

BPT colors) and \mathcal{U} and $\log_{10} n_H$, in the following section we will discuss how our H II regions sample the certain range of \mathcal{U} on the BPT plot, how this connects to our understanding of H II region structures, and how the assumptions in other models break down.

3.4.2 Quasi-Static HII Regions on the BPT Diagram

We plotted the four quasi-static H II region model results on the BPT diagram, together with the \mathcal{U} contours in Figure 3.1. The input ionizing spectrum is fixed at 0 Myr age and the stars and gas have solar metallicity, the same input parameters as the \mathcal{U} contours.

First we noticed that three out of four models, Model 1 to 3, appear to trace a very similar sequence of \mathcal{U} on the BPT diagram. The results of Model 4 at the lower L_i end also trace the same sequence of \mathcal{U} , while the higher L_i results divert and sample a different sequence. Overall, although the models seem to sample a similar sequence of \mathcal{U} , each model shows different results and reveals the density structure of H II regions

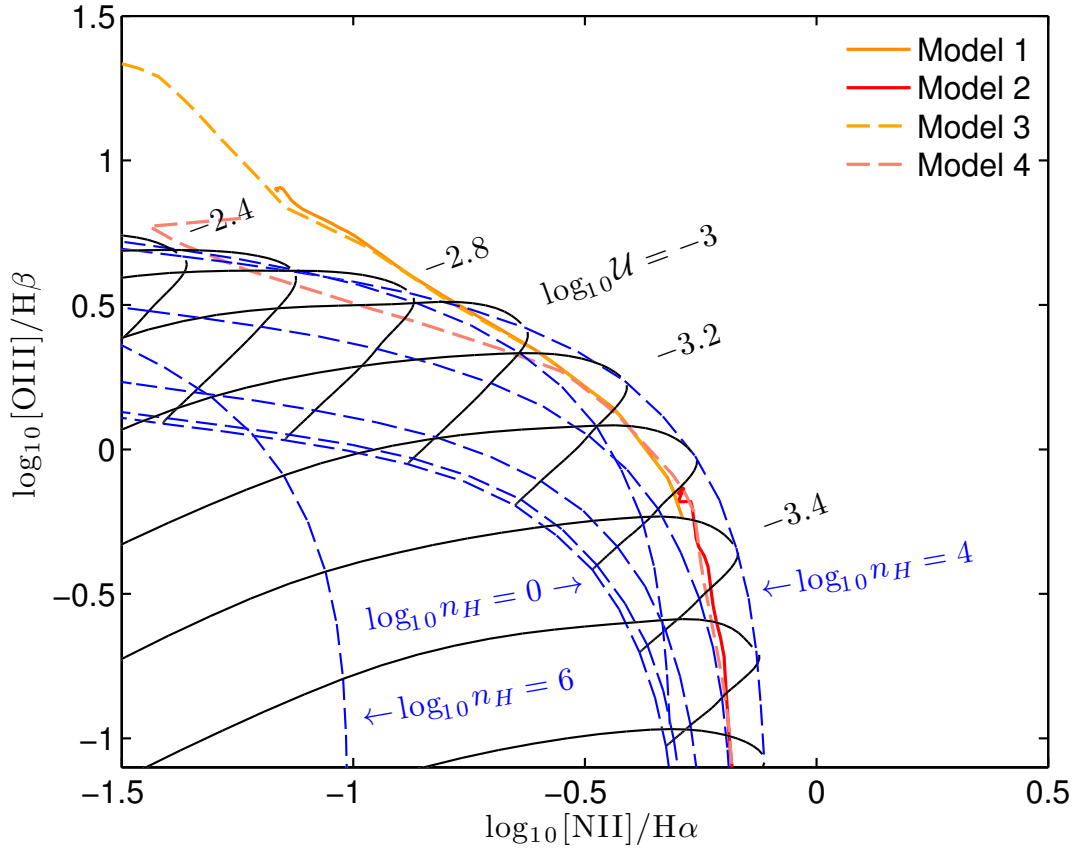


Figure 3.1: A demonstration of the mapping between the BPT colors and \mathcal{U} and $\log_{10} n_H$, at a fixed ionizing spectrum (0 Myr) and metallicity (Z_{\odot}). \mathcal{U} contours are shown in black lines, and the BPT colors (line ratios) are shown in blue dashed lines as a function of gas density grids. We also superimposed our Cloudy model results calculated with the same ionizing spectrum and metallicity, which are shown in red and orange lines.

under different physical conditions.

When stellar wind pressure is negligible ($\log_{10} \Omega = -2$), HII regions at the lower L_i end produced by Model 1 and Model 3 have very similar results, if not identical. However, HII regions at the high L_i end have quite different behaviors between Model 1 and Model 3. The \mathcal{U} values in Model 1 regions with high L_i appear to saturate at a finite value, whereas Model 3 regions can achieve much higher \mathcal{U} as L_i increases. This can be explained by the difference of density structures between Model 1 and Model 3 regions. Model 1 regions with high L_i are strongly dominated by radiation pressure. Under force balance, radiation pressure confines ionized gas into a much thinner layer and leads to a steep density gradient increasing towards the IF, limiting \mathcal{U} from reaching infinitely high in these HII regions. This effect of radiation pressure limited \mathcal{U} was discussed in detail in Chapter 2, § 2.3.2. At the lower L_i end, HII regions in Model 1 do not feel strong radiation pressure nor stellar winds, therefore the ionized gas layer has a homogeneous density with $\log_{10} n_{H,in} = \log_{10} n_H$, thus \mathcal{U} values decreases as L_i drops. HII regions in Model 3, with both radiation pressure and wind pressure neglected, are essentially Strömgen regions. These regions are filled with ionized gas of constant density everywhere in the ionized zone, and therefore their \mathcal{U} values are proportional to L_i . At the low end of L_i , HII regions of the same size in Model 1 and Model 3 are nearly identical, and they are Strömgen HII regions.

Model 2 and 4 are regions under strong pressurization of stellar winds ($\log_{10} \Omega = 2$) with large volume of ‘voids’ in the center and ionized gas confined in a thin shell on the outer edge. Therefore these regions are wind blown bubbles. However, none of the Model 2 bubbles have high \mathcal{U} values, even the ones with highest L_i , while Model 4 bubbles with the same L_i display much higher \mathcal{U} values, as shown in Figure 3.1. This dramatic difference between the two wind bubble models, arises from the influence of radiation pressure. Radiation pressure is completely neglected in Model 4 regions, therefore in their thin shells with constant density, \mathcal{U} can become arbitrarily large

when the incident L_i is very high. Because in this case \mathcal{U} is simply a function of L_i at fixed densities and bubble sizes. The Model 2 bubbles, however, feel radiation pressure. For these bubbles to have high \mathcal{U} values with the same bubble sizes their ionized gas layers must develop a pressure gradient. However a 1% pressure increase at the ionization front is not consistent with having $\log_{10} \Omega = 2$. Therefore, even Model 2 bubbles have thin shells of constant densities, their wind bubble volumes are larger than the Model 4 bubbles, leading to much lower \mathcal{U} values. Our model results show that in the most wind-dominated cases, Model 2 bubbles are one order of magnitude bigger than Model 4 bubbles. In other words, the only way to achieve $\log_{10} \Omega = 2$ is to inflate a wind-dominated bubble which has a truly thin ionized shell. Since such bubble is so wind-dominated, it is not possible to have radiation pressure at work and high \mathcal{U} at the same time. A wind bubble could achieve high \mathcal{U} values only if radiation pressure is completely neglected.

The high L_i wind-dominated bubbles (Model 4) appear to sample a different sequence of \mathcal{U} which has narrower range of \mathcal{U} values, and this behavior of such bubbles is quite natural. Strömgren H II regions are filled with ionized gas of constant density, therefore at a given distance in the region from the ionizing source, there is a corresponding \mathcal{U} value. With constant density distribution, the closer the radius is to the ionizing source, the higher the \mathcal{U} value. Therefore Strömgren H II regions cover a wider range of \mathcal{U} . On the other hand, most volume of the interior of Model 4 bubbles is filled with adiabatic expanding winds, their constant-density thin shells are much further away from the ionizing source. Ionized gas layers in Model 4 bubbles therefore resemble the outer layers of Strömgren regions and appear to sample a narrower range of \mathcal{U} values.

In § 3.4.1, we demonstrated the BPT line ratios calculated in a slab of ionized gas with constant densities. Therefore these line ratio contours should sample the \mathcal{U} contours on the BPT diagram in the same fashion as our Model 4 results, as both

calculations represent wind-dominated bubbles. In Figure 3.1, indeed our Model 4 traces the \mathcal{U} contours in a consistent fashion with the density- \mathcal{U} grids. Note that there is an offset between the constant-density line ratio contours and our model results at a given density. The shift may be due to hardening of the radiation fields in our models. The shape of an ionizing spectrum changes from the inner boundary of an HII region to its IF, because the ionizing photons of higher frequency have a smaller cross section. The change in ionizing spectrum could lead to a shift in the density- \mathcal{U} grid, therefore our modeled results would not track along the same density contours as we got for the original input spectrum.

3.4.3 Comparison of Different Photoionization Models

We set our HII model parameters in Starburst99 and Cloudy to be as close as possible to the D00 model, in order to verify that the differences seen among the models are physical, not numerical. In Figure 3.2, we compare our four model results with the results computed by D00 and L10, at the same age of ionizing star cluster (0 Myr) and same density $\log_{10} n_{H,in} = 1$.

The D00 model, which did not include radiation pressure and adopted plane-parallel ionized gas slabs at a fixed density, is essentially a wind-dominated wind bubble model. Therefore our closest model to the D00 model is Model 4. Indeed, our Model 4 results agree with the D00 results fairly well; the differences in line ratios of the D00 model and our Model 4 are around 0.1 to 0.2 dex. This confirms that our Cloudy model, with input parameters set very close to the D00 settings, produces reliable results. The L10 models calculated the BPT diagnostic line ratios as a function of \mathcal{U} grids, and they also adopted plane-parallel ionized gas slabs with constant density, while radiation pressure is also included. As we have discussed in § 3.4.2, the only way for a wind bubble to achieve high \mathcal{U} values is to shut off radiation pressure. Therefore the assumptions in the L10 model are physically inconsistent, an

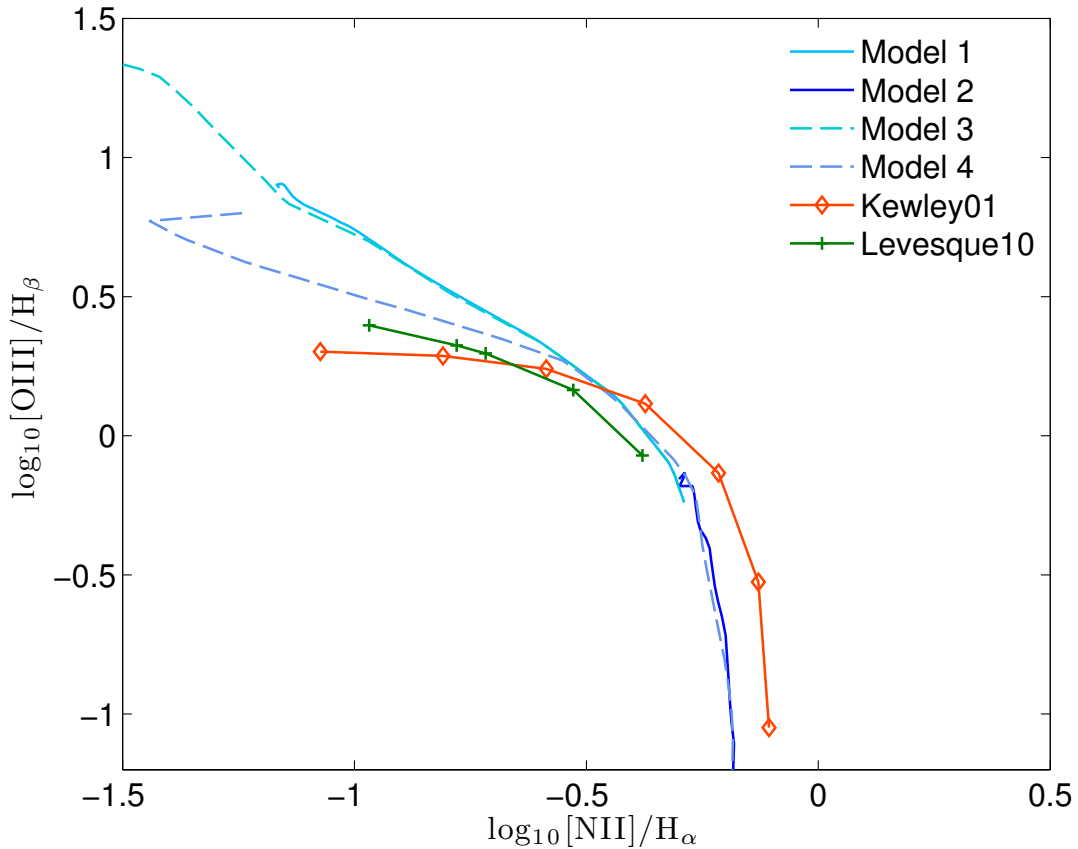


Figure 3.2: D00 model, L10 model, and our model results, compared on the BPT diagram. The D00 model (also marked as Kewley et al. 2001 in the plot) result is shown in orange, the L10 model result is in green, and our model results are shown in blue lines.

HII region cannot be wind-dominated with radiation pressure and high \mathcal{U} all at the same time. The L10 regions are wind-dominated bubbles, and they indeed agree with our Model 4 best. The differences of the line ratios computed by L10 and our Model is 0.1 dex. When compared with observed \mathcal{U} values, wind-dominated wind bubble model overestimates \mathcal{U} , and in studies like Dopita et al. (2005) the wind luminosity has to be drastically cut down to resolve the problem.

3.5 Conclusions

We carried out quasi-static H II region models using Starburst 99 and Cloudy, which covered a wide range of density and age. Our models represent four types of H II regions: (1) radiation pressure dominated H II regions and stellar winds are negligible (Model 1), (2) wind bubbles with radiation pressure (Model 2), (3) Strömgren H II regions (Model 3), and (4) wind-dominated wind bubbles (Model 4). For the first time, we explore these H II region structures and their implications on the BPT diagram.

We demonstrated that at a given radiation field hardness, photoionized regions are located on the lower left corner of the BPT diagram, which is consistent with the H II region behavior empirically determined by the $[\text{O III}]/\text{H}\beta$ and $[\text{N II}]/\text{H}\alpha$ diagnostics. A Strömgren region can achieve arbitrarily high \mathcal{U} values, while \mathcal{U} of a radiation pressure-dominated H II region saturates at a limited value. A stellar wind-dominated region cannot have high \mathcal{U} and radiation pressure all at the same time. A realistic wind bubble will be wind-dominated and with radiation pressure, so it will never have high \mathcal{U}_{obs} . The observed high \mathcal{U} regions must either be radiation pressure dominated regions, or magnetically-supported or impulsive regions of the type discussed in Chapter 2, § 2.4.3 and § 2.4.4, although this is less likely.

We compared our Cloudy model results with the D00 and L10 models. The D00 and L10 regions are wind-dominated bubbles of thin ionized shells, which corresponds to our Model 4. Our model results agree well with D00 and L10 at the same density and age. This reassures us that the differences seen among different photoionization models reflect fundamental differences of H II region structures. Caution must be paid to the structure and physical properties of modeled H II regions, in addition to spectral synthesis and photoionization modeling parameter space studies. H II region dynamics shall be taken into account in H II region modeling work of galaxies. The upcoming paper by Verdolini et al. (2012, in prep.) will investigate H II region properties and their impact in high redshift galaxies, using a more sophisticated

dynamical model which also covers a wide range of density and age grids.

Chapter 4

The 30 Doradus Nebula: An Imaging Study of Molecular and Ionized Hydrogen

4.1 Chapter Overview

We present the very first, fully calibrated H_2 1–0 S(1) image of the entire 30 Doradus nebula. The observations were conducted using the NOAO Extremely Wide Field Infrared Imager on the CTIO 4-meter telescope. Together with a $\text{Br}\gamma$ image of 30 Dor taken by NEWFIRM, our images reveal the morphologies of the warm molecular gas and ionized gas in 30 Doradus. Based on the morphologies of H_2 and $\text{Br}\gamma$, line ratio H_2 to $\text{Br}\gamma$, and Cloudy models, we found that the H_2 emission is formed inside the photodissociation regions of 30 Doradus, very close to the surface in association with the ionization front of the H II region. We also suggest that the bright H_2 -emitting area, which extends from the northeast to the southwest of R136, is a photodissociation region viewed face-on, while many clumps and elephant trunk features located at the outer shells of 30 Doradus are also photodissociation regions viewed edge-on. The characteristic radiation to gas pressure ratio is evaluated at selected regions in

30 Doradus, and we conclude that radiation pressure is not the dominating force at the current phase of 30 Doradus, while the pressurization of stellar winds and the injection of photoevaporative flows are likely the major feedback mechanisms acting to reduce the observed ionization parameter in 30 Doradus.

4.2 Introduction

The role of starburst feedback is vital in galaxy evolution, as it can be important in unbinding large molecular clouds (Krumholz et al. 2006; Fall et al. 2010; Murray et al. 2010), driving gravitational collapse inside molecular clouds and triggering sequential star formation (Elmegreen & Lada 1977; Oey et al. 2005; Zavagno et al. 2010), driving turbulent motions within the clouds (Matzner 2002), eroding molecular clouds by photo-evaporation (Whitworth 1979; Williams & McKee 1997; Matzner 2002), and determining emission line spectra of the H II regions (Yeh & Matzner 2012, Chapter 2). While the effects of massive star feedback have been extensively discussed in the literature, a critical piece of information is missing: how much energy and momentum feedback from massive stars can act to affect the molecular clouds' physical properties? Molecular hydrogen emission lines carry clues to answer this question.

H_2 emission arises at the boundary of ionized gas and neutral clouds, which is the working surface for many forms of stellar feedback into the dense gas. H_2 molecules can be excited via radiative or mechanical energy input, and the emission lines are also sensitive to the physical conditions inside the molecular clouds. Determination of the H_2 line excitation mechanisms therefore is crucial to quantify massive star feedback and molecular cloud physical conditions in starburst regions.

The 30 Doradus nebula (30 Dor) in the LMC is a well-studied and the nearest (50 kpc) starburst region, at which distance a very high spatial linear resolution ($1'' = 0.2$ pc) can be achieved. The 30 Dor nebula is dominated by the very young star cluster R136, which produces $10^{51.6}$ hydrogen-ionizing photons per second (Crowther

& Dessart 1998), equivalent to 50 O3 stars, ionizing neutral material and driving it outward. As a starburst prototype, 30 Dor's simplicity, unique proximity, and convenient location out of the galactic plane allow a direct comparison to more distant starburst regions. Many observations of 30 Dor have been done in the wavelengths from the X-ray to radio (Townsend et al. 2006; Chu & Kennicutt 1994; Poglitsch et al. 1995; Rubio et al. 1998; Indebetouw et al. 2009; Johansson et al. 1998), which provide a wealth of information on 30 Dor. However, a fully calibrated H₂ map of the entire 30 Dor has never been produced, missing the key opportunity to quantify the feedback energy budget.

Observations of H₂ in parts of 30 Dor have been done by Poglitsch et al. (1995) (P95) and Rubio et al. (1998) (R98). From the morphology and measured fluxes of Br γ and H₂ 1–0 S(1), P95 suggested that the two types of emission are spatially mixed. The measured H₂ to Br γ ratio is ~ 0.2 , indicating a high fraction of warm molecular clouds to ionized gas in 30 Dor. With their CO data mapped in the same area, P95 further suggested that the H₂ emission formed in warm (~ 2000 K) and dense (10^6 cm⁻³) molecular clouds. However the P95 data is observed in a $2' \times 2'$ area in 30 Dor, which is a very small fraction of the region. Therefore the reported line intensities and line ratio do not represent the true physical conditions of the photodissociation regions (PDRs) in 30 Dor. On the other hand, the H₂ data published by R98 was not calibrated, and again it was taken in a small area (few arcminutes). Comparing to the size of 30 Dor ($\sim 24' \times 30'$), the P95 and R98 data provide very limited information.

In this chapter, we present the very first fully calibrated H₂ 1–0 S(1) image of 30 Dor with high spatial resolution ($1''$, 0.2 pc), as well as a Br γ image of the full nebula. We describe the observations and data reduction in § 4.3. In § 4.4, we show the H₂ and Br γ morphologies and determine line ratios, identify areas of interest for further analysis, and investigate the spatial relations between H₂ and Br γ . In § 2.6, we present photoionization models using Cloudy, in order to explore the issue of bright line

contamination in the H₂ image we discovered during data reduction, and to further study the range of physical parameters inside the 30 Dor PDRs by comparing the modeled and observed H₂ to Br γ line ratio. The origin of the H₂ 1–0 S(1) emission and assessments of the impact of radiation pressure feedback in 30 Dor are discussed in § 4.6. Finally, we summarize the chapter in § 4.7. In the following sections of the chapter, all H₂ emission refer to the H₂ 1–0 S(1) transition, unless indicated otherwise.

4.3 Observations and Data Reduction

We observed 30 Dor using the NOAO Extremely Wide Field Infrared Imager (NEW-FIRM; Probst et al. (2008)) on the CTIO 4-meter telescope, over three half-nights on November 10, 11, and 12, 2010. NEWFIRM has a field of view of $28' \times 28'$, and its pixel scale is $0.4''$ per pixel. The field of view is almost exactly the same as the diameter of 30 Doradus ($\sim 30'$), so that the region can be covered by a single pointing in the sky. The H₂ 1–0 S(1) ($2.12 \mu\text{m}$) and Br γ ($2.17 \mu\text{m}$) emission line data were taken using the $2.124 \mu\text{m}$ H₂ and $2.168 \mu\text{m}$ Br γ narrow band filters, respectively. The broad-band continuum data were collected using the Ks filter. The total exposure time of the H₂ image was 210 minutes, and 14 minutes for the Br γ image. The observations were dithered in a random pattern in a $30''$ box to fill the gaps between detector arrays. The photometric standard star S121-E was observed in both $2.124 \mu\text{m}$ and $2.168 \mu\text{m}$ filters to serve as the flux calibrator. Table 4.1 summarizes details of the observations. Because the angular size of 30 Dor in the sky is about the same as the size of NEWFIRM field of view, in order to obtain sky images free of nebular emissions, we nodded the telescope on and off the target following the sky-target-target-sky sequence.

Data reduction was carried out using the NEWFIRM pipeline V1.0 (Swaters et al. 2009). Dark subtraction was first applied to the data, followed by a linearity correction and flat fielding. Sky background was determined by taking the median of four preceding and four subsequent sky exposures, and the background level was scaled

to match that in target images and then subtracted. An astrometric solution was obtained using the 2MASS catalogue, and all images were reprojected and stacked. The sky background was then redetermined and subtracted by masking objects (including stars and extended nebular emission) detected in the first pass, and new stacks of images were produced.

4.3.1 Ripple Pattern Removal in the $Br\gamma$ Image

Narrow band filters provide peak transmission rate at the designated central wavelengths over the field of view. However, in the case of a wide field of view, the filter bandpasses shift in wavelength as a radial function within the field of view, due to varying optical path length of convergent beams in the optics. At the center of the field, the designated emission line shifts to the blue end of the bandpass, and at the corner of the field the line shifts to the red end. Because of the bandpass shifts as a function of the position in the field, the amount of OH sky emission lines that pass through the narrowband filter varies, causing ‘ripple-like features’ appearing as concentric rings in the image. The intensity of these ripple features vary with time due to variations of night sky emission, but their structure is stable. In practice their structure can be characterized and removed using observations which frequently alternate on- and off-target. Significant ripple patterns are seen in the $Br\gamma$ data (Figure 4.1.). Because the $Br\gamma$ data were taken in a rather short sequence with comparatively longer exposure times, 14 minutes on the sky and 14 minutes on the target, the variation in the ripple feature intensity was not well traced. The default pipeline reduction is not designed to remove this additive background.

To characterize the ripple pattern, we first combined the $Br\gamma$ sky images that were free of nebular emission; stars were masked and the pixels are interpolated, yielding a template image which contains only the ripple pattern. The next step was to find the proper scaling factor of the ripple template with respect to that in the $Br\gamma$ image.

Table 4.1. Observation Summary

Target	Line	Vacuum Wavelength	Filter ^a	Observed Dates	Total Integration Time (minutes)	Note
30 Doradus	Ks band continuum	...	Ks	November 10 and 12, 2010	210	
30 Doradus	H ₂ 1-0 S(1)	2.121 μ m	2124 nm	November 10, 11, and 12, 2010	210	
30 Doradus	Br γ	2.166 μ m	2168 nm	November 11, 2010	14	
S121-E	H ₂ 1-0 S(1)	2.121 μ m	2124 nm	November 10, 11, and 12, 2010	210	Photometric standard
S121-E	Br γ	2.166 μ m	2168 nm	November 11, 2010	14	Photometric standard

^aSee Table 4.2 for filter configurations.

We masked stars in the Br γ image, selected areas with pixels of high S/N and free of nebular emission. We determined the scaling factor using an iterative process as follows: (1) multiply the template image by a series of trial scaling factors κ , (2) in each case subtract the scaled template image from the Br γ image, (3) find the slope $\delta\kappa$ of the relation between the residual Br γ and template image, and (4) from a curve fit to the plot of $\delta\kappa$ vs. κ , find the solution κ where $\delta\kappa = 0$. The final result was found to be $\kappa \sim -0.12$, which was then used as the adopted scaling factor.

Note that ripple patterns are not seen in the H₂ image. This is because the H₂ data were taken over a much longer time baseline (3 nights), with on- and off- target measurements made in a very frequent fashion (every 10 minutes). The variation of the ripple patterns is therefore well traced and recorded, and the default pipeline reduction successfully removed the ripples. We then measured the mode of the H₂ pixel distribution free of nebular and stellar emission, to provide indication of any residual baseline in the corrected image. Figure 4.1 and Figure 4.2 show the results, including before and after removal of the ripple patterns.

4.3.2 PSF Matching Among the H₂ , Br γ , and Ks Images

We carried out a photometric analysis of field stars using the software package SExtractor (Bertin & Arnouts 1996). Stars with detection higher than 5σ in areas free of extended nebular emission are identified by SExtractor, and their photometric parameters, such as flux and FWHM, are recorded in catalogues. We first extracted the mode of the distribution of FWHM in each stacked image, namely Br γ , H₂ , and Ks images, as the representative seeing in each image. It showed that Br γ and Ks images have better seeing ($< 1''$) than the H₂ image. We then convolved the Br γ and Ks images with gaussian kernels of various sizes, until the convolved FWHM matches that of the H₂ image. After the gaussian convolution, the seeing in H₂ , Br γ , and Ks images is $1.0''$.

Table 4.2. Filter Configurations

Filter Name	Filter Central Wavelength	Filter FWHM
Ks	2.150 μm	320 nm
2124 nm	2.132 μm	24.0 nm
2168 nm	2.177 μm	24.4 nm

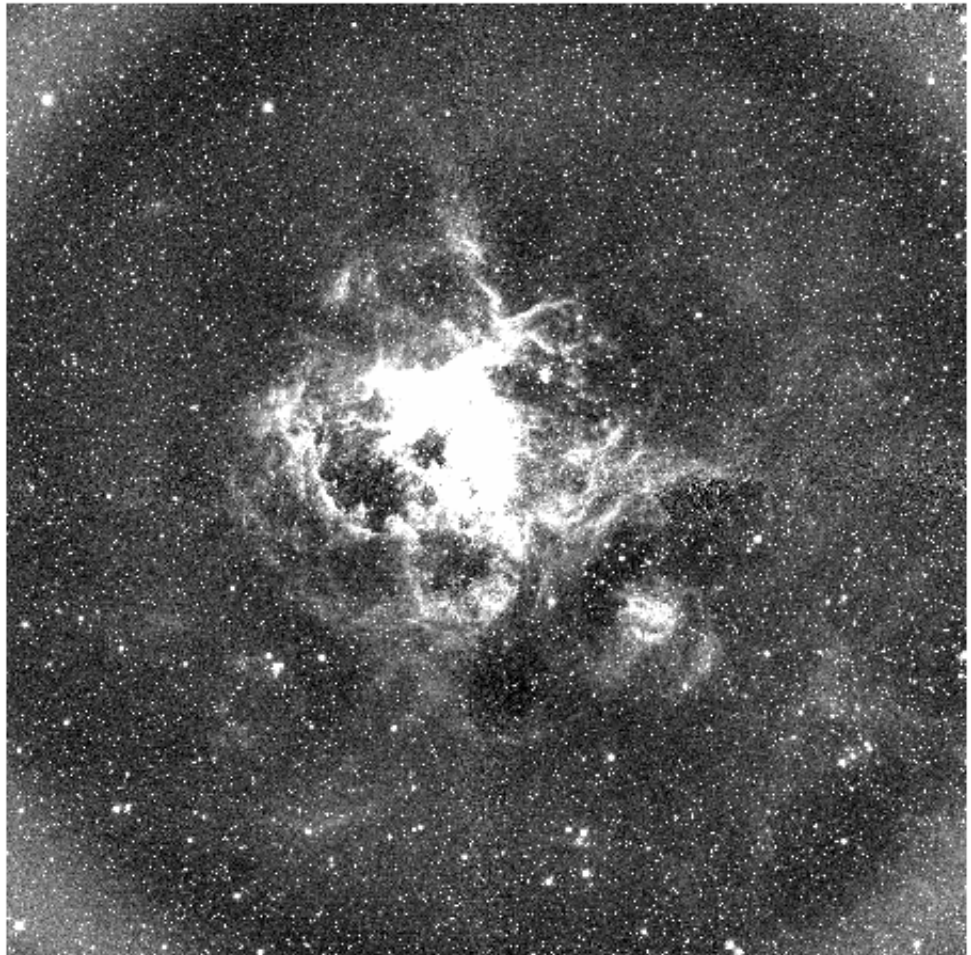


Figure 4.1: Stacked Br γ image of 30 Doradus, showing a significant ripple pattern caused by the OH sky emission lines.



Figure 4.2: Stacked $Br\gamma$ image of 30 Doradus, with ripples removed.

4.3.3 Continuum Subtraction

To produce line emission images, one must subtract continuum emission in narrow-band (NB) data. The ideal way to subtract continuum in a NB image, which contains one emission line, is to use an off-line center NB filter with identical bandwidth. Such an off-line center NB image provides continuum emission without contamination of any emission lines. However, off-line NB filters were not available when the observations were conducted. We thus carried out continuum subtraction using the broadband (BB) Ks data. However the BB Ks data contain more than just continuum emission. The data also contain Br γ and H₂ emission lines, and possibly other emission lines as well, which introduce contamination in continuum emission. We will discuss the bright line contamination in the second half of the section.

The observed fluxes in each filter (2.12 μ m, 2.16 μ m, and Ks) can be expressed as

$$F_{2124} = F_{H_2} + F_{cont_{2124}} , \quad (4.1)$$

$$F_{2168} = F_{Br\gamma} + F_{cont_{2168}} , \quad (4.2)$$

$$F_{Ks} = F_{H_2} + F_{Br\gamma} + F_{unknown} + F_{cont_{Ks}} , \quad (4.3)$$

where F_{2124} , F_{2168} , and F_{Ks} are fluxes measured in the 2.12 μ m, 2.16 μ m, and Ks filters, respectively. The convention ‘cont’ labels the continuum emission fluxes measured in a filter, and ‘unknown’ marks unknown emission line fluxes contained within the Ks filter.

Continuum subtraction in Br γ and H₂ images then will produce:

$$\begin{aligned} F_{2168} - \alpha F_{Ks} &= F_{Br\gamma} + F_{cont_{2168}} - \alpha(F_{H_2} + F_{Br\gamma} + F_{unknown} + F_{cont_{Ks}}) , \text{ yielding} \\ F_{Br\gamma} &= \frac{F_{2168} - \alpha(F_{Ks} - F_{H_2} - F_{unknown})}{1 - \alpha} , \end{aligned} \quad (4.4)$$

and

$$\begin{aligned} F_{2124} - \beta F_{Ks} &= F_{H_2} + F_{cont_{2124}} - \beta(F_{H_2} + F_{Br\gamma} + F_{unknown} + F_{cont_{Ks}}) , \text{ yielding} \\ F_{H_2} &= \frac{F_{2124} - \beta(F_{Ks} - F_{Br\gamma} - F_{unknown})}{1 - \beta} , \end{aligned} \quad (4.5)$$

where α and β are the scaling factors that makes $\alpha F_{Ks} = F_{cont_{2168}}$ and $\beta F_{Ks} = F_{cont_{2124}}$. The equations are true at every pixel in the image. The values of α and β in principle should be close to the filter bandwidth ratio of $\frac{2168}{Ks}$ and $\frac{2124}{Ks}$.

We determine α and β empirically by evaluating stellar flux ratio of 2.16 μm to Ks, and 2.12 μm to Ks. We employed SExtractor (Bertin & Arnouts 1996) to extract stellar fluxes in the 2.12 μm , 2.16 μm , and Ks images. Stars with counts higher than 10,000 ADU are excluded in the analysis, because the response of the CCD detectors becomes nonlinear in this regime. The scaling factor α and β are both 0.070, which is in good agreement with the bandwidth ratios $\frac{2168}{Ks}$ and $\frac{2124}{Ks}$.

Bright Emission Line Contamination Contributing to F_{unknown}

No direct information is available to us on the various possible emission lines (other than Br γ and H₂) which might contribute to the Ks filter emission. However, He I is a likely candidate since it is observed in other star forming regions. For example, helium emission lines are reported in M16 in the 2 μm regime (Levenson et al. 2000), in addition to Br γ and H₂ lines. Among the detected emission lines, Br γ is the brightest in M16, and a bright He I line at 2.06 μm is 70% of the total flux of Br γ . If the He I -to-Br γ ratio is the same in 30 Dor as in M16, the contamination from He I in the Ks filter will be noticeable.

It is rational to assume that Br γ line in 30 Dor is the brightest among the emission lines in the Ks filter. If the He I line has the same relative strength in 30 Dor as in M16 (70%), Equation 4.4 shows that it would represent about 5% of the Br γ emission, assuming it were distributed in the same way. Therefore continuum subtraction in the Br γ image may not be severely affected by bright emission line contamination, and Equation 4.4 can be approximated as

$$F_{Br\gamma} \simeq \frac{F_{2168} - \alpha F_{Ks}}{1 - \alpha} . \quad (4.6)$$

In the case of H₂ continuum subtraction, however, bright emission line contamination becomes a prominent effect. The continuum subtracted H₂, following Equation 4.5, shows that if no correction were made, then there would be a noticeable over-subtracted area in the vicinity of the nebula. Indeed, without correction, we noted a significant region of negative emission representing the Br γ emission. We found, via careful visual inspection, that the negative components well resemble the morphology of highest surface brightness Br γ emission. We then inspected the H₂ and Br γ images on the pixel-to-pixel basis, comparing the pixel values of the negative component in the H₂ image to the Br γ image. There is a tight correlation between the negative H₂ pixels and brightest Br γ pixels, confirming that the majority of over-subtraction comes from Br γ emission, and the slope of negative H₂ to Br γ pixels is ~ -0.09 . Therefore we correct continuum subtraction of the H₂ image by

$$F_{H_2} = F_{2124} - \beta F_{Ks} + 0.09 F_{Br\gamma} . \quad (4.7)$$

We inspected the pixel values of the corrected H₂ image, indeed the majority of the negative pixels after the correction have values around 0. In fact the factor 0.09 is higher than the expected value $\beta/(1-\beta) = 0.075$, which confirms that we have not only corrected for the contamination introduced by the Br γ emission, but also the contamination from other unknown bright emission lines. The contamination is thus $(0.09-0.075)/0.075 = 0.2$, or 20% of the Br γ emission, which corresponds to 1.5% of the Br γ flux.

We found that, after correcting the H₂ image for the contamination, some negative pixels still persist in the areas very close to R136. Those pixels can only be corrected by adding $0.12F_{Br\gamma}$ instead of $0.09F_{Br\gamma}$ in Equation 4.3. However this leads to over-correction in the image, i.e. bright Br γ features become prominent in the H₂ image, which indicates that the contaminating emission is stronger relative to Br γ near the cluster than further away. The corresponding total brightness of this line is about 60% of the Br γ emission assuming that the emission line flux is distributed in the

Ks band in the same way as Br γ , which leads to additional 3% of the Br γ flux. We suspect that He I line at 2.06 μm is the major source of continuum contamination other than Br γ , and its contamination becomes more significant in the central region of 30 Dor. Several He I lines are detected in the M16 H II region, in addition to Br γ and H₂ 1–0 S(1) (Levenson et al. 2000). As noted earlier, the brightest He emission line detected in M16 in the 2 μm regime is He I at 2.06 μm , and its flux of the He I line is 70% of the total flux of Br γ . This is a close agreement to the 60% level we have empirically estimated for the region near the cluster. Since the factor for continuum flux contamination varies from 0.09 to 0.12, the uncertainty of the corrected H₂ flux will be about 3% of the Br γ flux.

We do not have any He line data in 30 Doradus to constrain the degree of contamination, therefore we turn to Cloudy simulations to explore this issue, which is discussed in § 4.5. The H₂ image displayed in Figure 4.3 is empirically corrected for contamination, following Equation 4.7.

4.3.4 Flux Calibration

The standard star S121-E (Persson et al. 1998) was observed to provide flux calibration for the 30 Doradus data. The Ks magnitude of S121-E is 11.781 mag., which corresponds¹ to $8.32 \times 10^{-16} \text{ erg s}^{-1} \text{ cm}^{-2} \text{ \AA}^{-1}$. S121-E measured 879 counts in the Br γ image, and 974 counts in the H₂ image. Therefore 1 count corresponds to $9.28 \times 10^{-19} \text{ erg s}^{-1} \text{ cm}^{-2} \text{ \AA}^{-1}$ and $8.54 \times 10^{-19} \text{ erg s}^{-1} \text{ cm}^{-2} \text{ \AA}^{-1}$ in the 30 Dor Br γ and H₂ image, respectively. Since the Br γ and H₂ filters are centered closely at the Ks filter central wavelength, we apply the magnitude-to-flux density conversion factors derived from the S121-E data, to flux calibrate the 30 Dor Br γ and H₂ data. To do this, the above flux densities were each multiplied by the bandwidths (FWHM) of the

¹Magnitude to flux density conversion was provided by the Spitzer Science Center webpage at <http://ssc.spitzer.caltech.edu/warmmission/propkit/pet/magtojy/>.

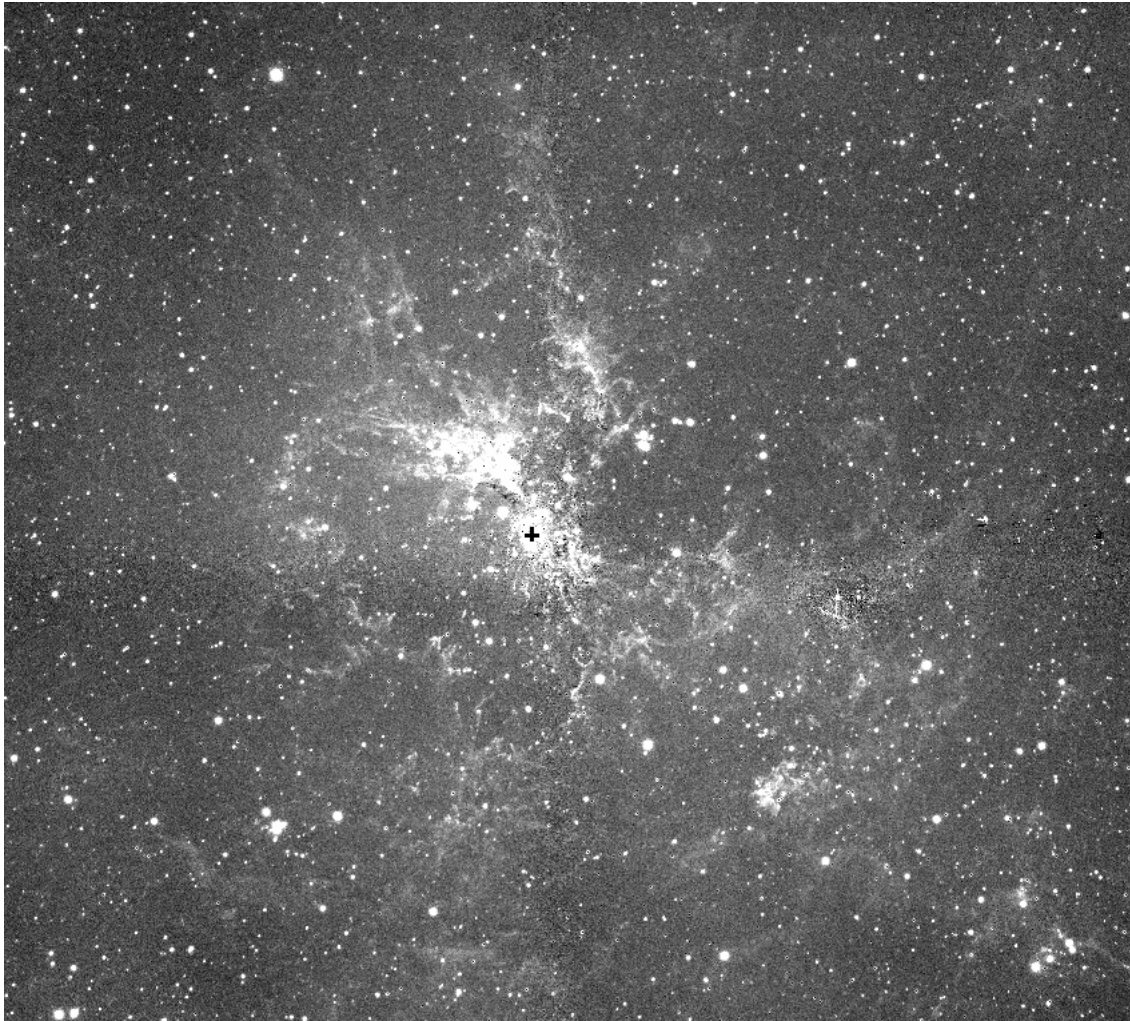


Figure 4.3: H_2 image, corrected for bright line contamination in the continuum following Equation 4.7. Field of view displayed here is $22.5' \times 20.3'$, and R136 is marked by a black cross.

respective narrow band filters.

4.4 Results

4.4.1 H₂ and Br γ Morphologies

Fully calibrated H₂ and Br γ images of 30 Dor are presented in a 3-color composite image in Figure 4.4. Red is H₂, blue is Br γ , and green is the Ks band continuum. Both Br γ and Ks are stretched logarithmically to emphasize areas of highest surface brightness, while H₂ is displayed in linear scale because the emission is much fainter. The star cluster R136 is marked by a black dashed circle. Note that the pulsar wind nebula N157B, which is located at the same distance and to the southwest of 30 Dor, also is present in the image. In this chapter we focus only on the analysis of 30 Dor and will ignore N157B.

The Br γ emission reveals the spatial distribution of ionized gas in 30 Dor. Areas with highest surface brightness appear to trace an arch structure extending from northeast to southwest of the R136 cluster, consistent with the ionized gas morphology reported in the literature (Chu & Kennicutt 1994; Poglitsch et al. 1995; Pellegrini et al. 2010). To the north and west of R136, Br γ appears quite filamentary and its surface brightness becomes lower. To the southeast of 30 Dor, the Br γ morphology reveals multiple shell structures, enveloping elephant trunks and clumpy features. The total flux in an area $11' \times 8.6'$ is measured as $2.43 \times 10^{-10} \text{ erg s}^{-1} \text{ cm}^{-2}$. This is higher than the total Br γ flux reported in P95 ($4 \times 10^{-11} \text{ erg s}^{-1} \text{ cm}^{-2}$), which is not surprising because our data cover much bigger field of view and the instrument is more sensitive.

The most prominent H₂ emission is seen to the northeast of R136, in conjunction with the bright Br γ arch and coincident with lower surface brightness Br γ emission. This prominent H₂ emitting area spans at least $3.6'$ by $2.1'$, which corresponds to $\sim 43 \times 23$ pc in the plane of the sky at a distance of 50 kpc. The H₂ emission in this area

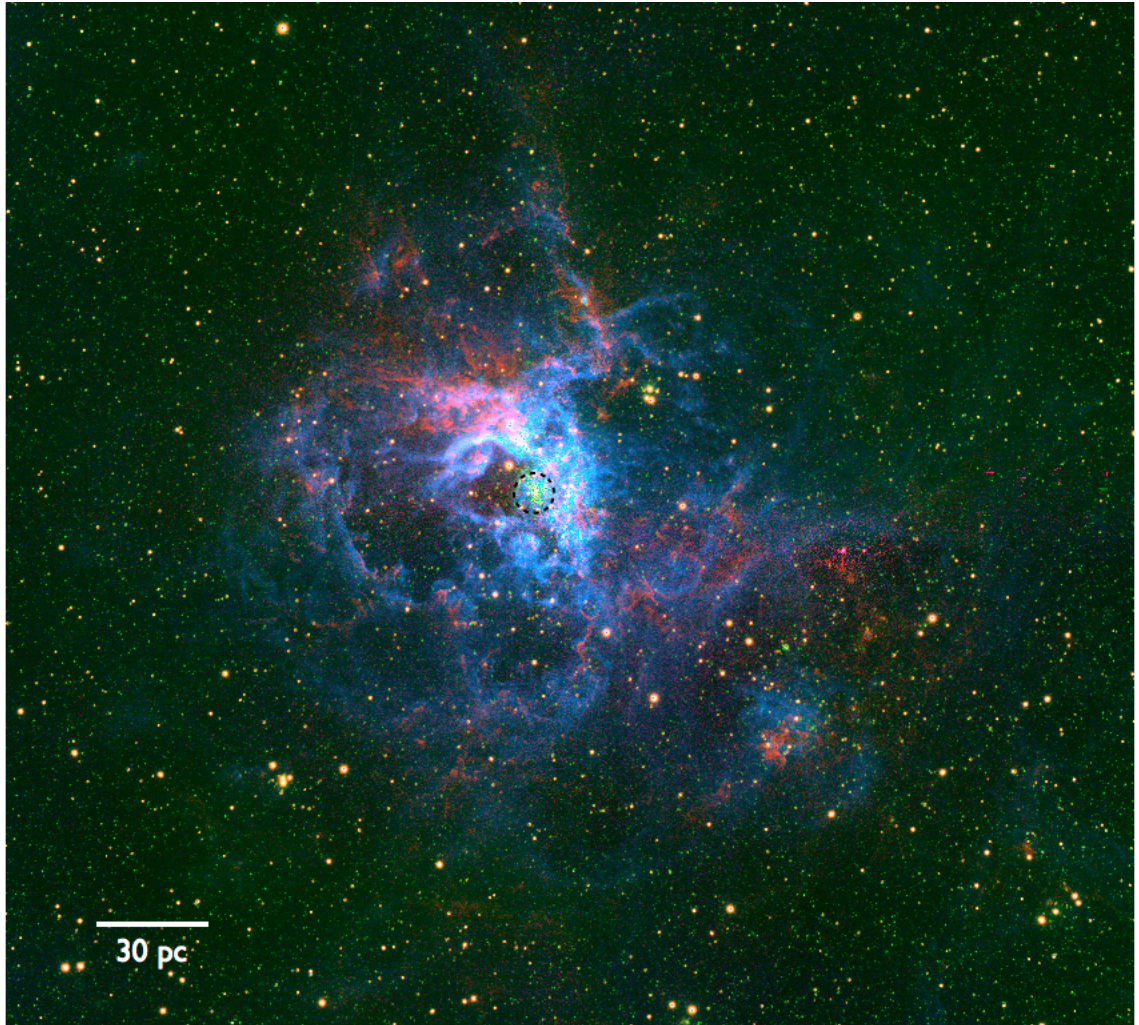


Figure 4.4: Three-color composite image of 30 Doradus. North is up and East is to the left. Red: H_2 , displayed in linear scale; green: K_s continuum in logarithm stretch; blue: $Br\gamma$ in logarithm stretch. The seeing is $1.0''$, and the field of view displayed here is $22.5' \times 18.5'$.

seems somewhat disordered, with clumps close to R136 and filaments extending away from R136. The H₂ emission to the west of R136 appears much clumpier and mixed with high surface brightness Br γ emission. To the north and northeast of R136, H₂ appears in the form of filaments which seem to form a chimney pointing away from R136, and their morphology is poorly correlated with the Br γ filaments in the same area. Prominent elephant trunks are seen in the southeast of R136, pointing towards the ionizing source R136 and are encompassed by Br γ emission. The radii of curvature of these elephant trunks are noticeably smaller than that of the Br γ envelope. H₂ is more clumpy to the south of R136, seemingly mixed with more diffuse Br γ emission. No H₂ emission was detected to the northwest of R136. The total H₂ flux measured in an area 11' \times 8.6' is $3.12 \times 10^{-11} \text{ erg s}^{-1} \text{ cm}^{-2}$.

In the areas where both Br γ and H₂ are brightest (northeast to southwest of R136), Br γ and H₂ emissions have good spatial correlation, which implies that we are viewing the H II region face-on. On the outer parts of 30 Dor, we see a separation between H₂ and Br γ emission, such as in the elephant trunks to the southeast and filaments to the north of R136. This poor spatial correlation between H₂ and Br γ then implies that we are viewing those parts of H II region edge-on. Overall, the Br γ and H₂ emitting-material appear to form walls of the cavities or holes seen in 30 Dor. The observed H₂ emission is located well within the nebula

4.4.2 Areas of Interest

We superimposed our H₂ and Br γ data with the ¹²CO 1–0 data (hereafter referred to as CO data) of 30 Dor (Wong et al. 2011). The Br γ image is displayed in grayscale to guide the reader's of ionized gas morphology. We convolved the H₂ image with a 8'' (in diameter) Gaussian kernel and plotted the contours, beginning at 20% of the peak Br γ intensity², increasing in 10% steps and stopping at 80% of Br γ peak

²The peak intensity is measured in a 2' \times 2' area northeast of R136

intensity. The spatial resolution of the CO data is 60''. We found that most bright H₂-emitting areas spatially correlate very well with the bulk of CO emission. Based on the morphological correlation between H₂ and CO emission, and H₂ and Br γ emission, a number of areas are identified as areas of interest for further analysis.

The areas of interest (marked in Figure 4.6) are as follows: (1) Area A: the north-eastern band of H₂ emission with highest H₂ surface brightness, and this area also spatially coincides with the brightest CO emission in 30 Dor; (2) Area B: the filament pointing north away from R136, which is relatively bright and spatially correlated well with the peak of CO emission in the same area; and (3) Area C: one elephant trunk to the southeast of R136 at the outer shell of 30 Dor, which has a very clearly defined morphology in the H₂ emission, surrounded by a Br γ -emitting envelope, and no CO emission is detected in this region.

H₂ was detected in an earlier observation (P95) in the western part of Area A, in a much smaller area (2' \times 2'). The H₂ morphology observed by P95 was reported to be very clumpy, which is consistent with the H₂ we observed (Figure 4.5). The peak H₂ surface brightness in the P95 result is $5.41 \times 10^{-15} \text{ erg s}^{-1} \text{ cm}^{-2} \text{ arcsec}^{-2}$. However this peak intensity arises from a point-like source in the P95 data, and it corresponds to a bright star. The reported peak intensity may thus not be reliable. In our observations, more H₂ emission is seen towards the eastern part of Area A. The maximum H₂ surface brightness is measured $8.18 \times 10^{-16} \text{ erg s}^{-1} \text{ cm}^{-2} \text{ arcsec}^{-2}$, after masking the bright stars in the field and convolved to a 8'' resolution. This peak intensity is lower than that reported in P95; however, as we have pointed out, the peak H₂ intensity in P95 likely comes from a bright star. H₂ in Area A also coincides with the bulk of CO emission in 30 Dor (Wong et al. 2011) (Figure 4.5). The good spatial correlation between the H₂ and CO emission suggests that the H₂ emission comes from molecular clouds, and it traces the ¹²CO emission. No H₂ emission is seen completely unrelated to either the Br γ or ¹²CO 2–1 emission, therefore there is no evidence for shock excited

H₂ emission, such as that seen in the Orion A giant molecular cloud (Davis et al. 2009).

Area B also shows high H₂ intensity, and the maximum H₂ surface brightness in this area is $4.23 \times 10^{-16} \text{ erg s}^{-1} \text{ cm}^{-2} \text{ arcsec}^{-2}$. This region was not detected in the P95 observations, because it is located outside their field of view. Area B lines up well with its CO counterpart (Wong et al. 2011) (see Figure 4.5), which is indicative that like in Area A, the H₂ emission traces ¹²CO, and it does not likely originate from fast outflows of protostars. As for Area C, the peak intensity measured at the tip of the elephant trunk feature is $2.58 \times 10^{-16} \text{ erg s}^{-1} \text{ cm}^{-2} \text{ arcsec}^{-2}$, comparable to the peak intensities measured in other areas. Although Area C does not appear to have any CO counterpart, the presence of H₂ emission indicates that there must be molecular clouds in that location. The morphology of this elephant trunk is very similar to the ones observed in smaller H II regions, such as M16 (Hester et al. 1996; Levenson et al. 2000). A crude estimate of the projected distance between the Br γ envelope and the elephant trunk is ~ 3 pc. Area C's neighbor clumps and elephant trunks also show similar separation between Br γ and H₂. We will return to discuss this point in §4.6.2.

4.4.3 The Spatial Relationships Between Ionized and Molecular Gas in 30 Doradus

The overall morphology of the observed H₂ emission is well correlated with the Br γ distribution within 30 Dor – when Br γ emission is present, H₂ emission is either seen very nearby the Br γ emission, such as the outer shells and elephant trunks, or appear to be a counterpart of the Br γ emission, such as the bright regions northeast to southwest of R136. The bright H₂-emitting regions in Area A and around R136 are seen spatially coincident with the Br γ emission (Figure 4.5). This suggests that we must be viewing these parts of the H II region face-on, through a column of ionized gas with molecular clouds located behind rather than in front of the ionized gas as seen from the cluster. This is supported by the Br γ morphology that it appears to be

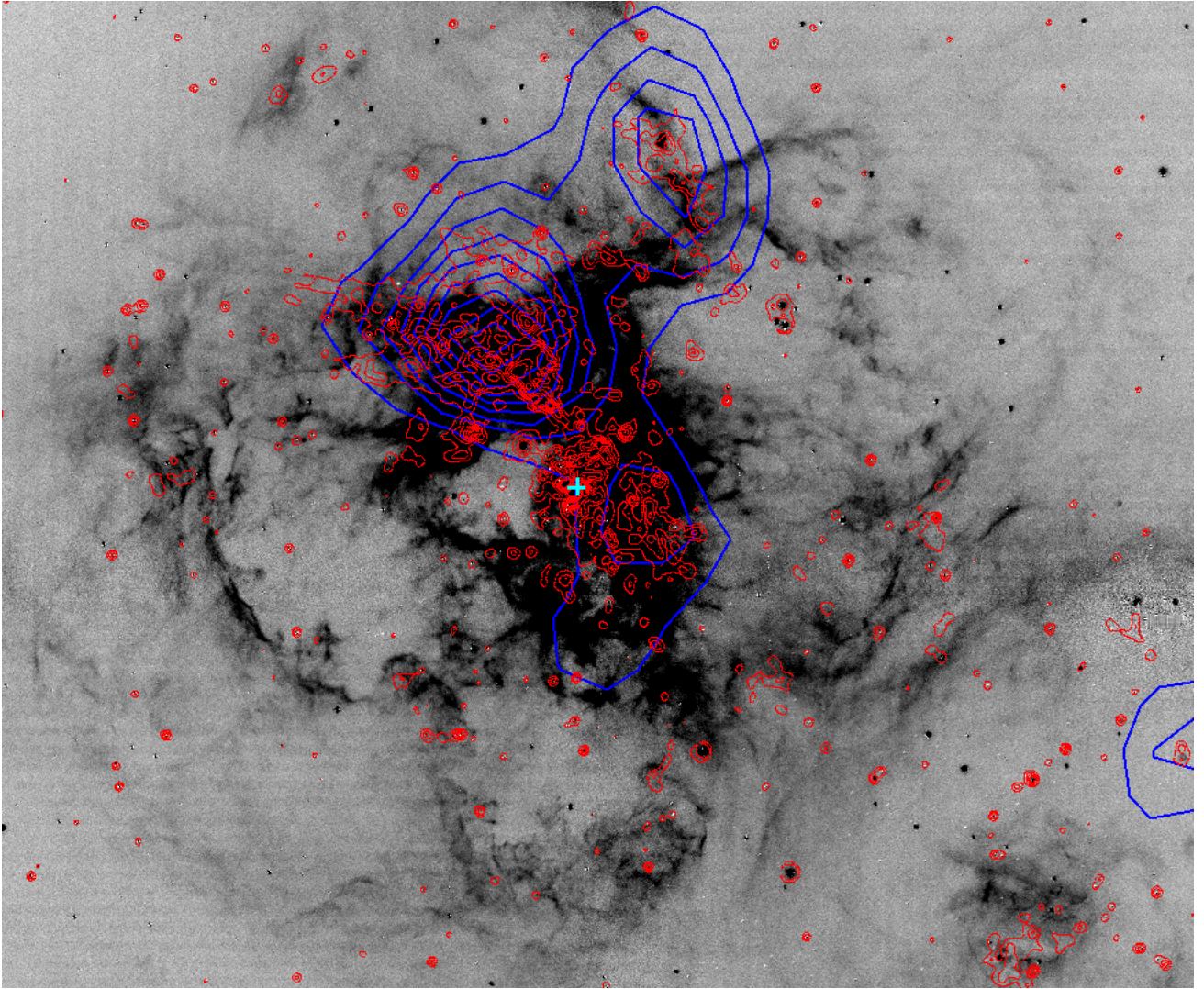


Figure 4.5: H₂ contours superimposed on Br γ (in grayscale) image and CO 1–0 contours (blue contours, Wong et al. 2011). The H₂ image was smoothed by a Gaussian kernel of 8'' diameter, and the contour levels of the smoothed H₂ data are plotted at 20% – 80% of the peak Br γ intensity ($8.19 \times 10^{-16} \text{ erg s}^{-1} \text{ cm}^{-2} \text{ arcsec}^{-2}$), increasing in 10% steps. The CO contours start at 10% of the peak intensity (12.4 K km s^{-1}), in 10% steps. The angular resolution in Br γ image is 1'', in H₂ is 8'', and in CO is 60''. The field of view displayed here is $12.8' \times 9.9'$; R136 is marked by a cyan cross.

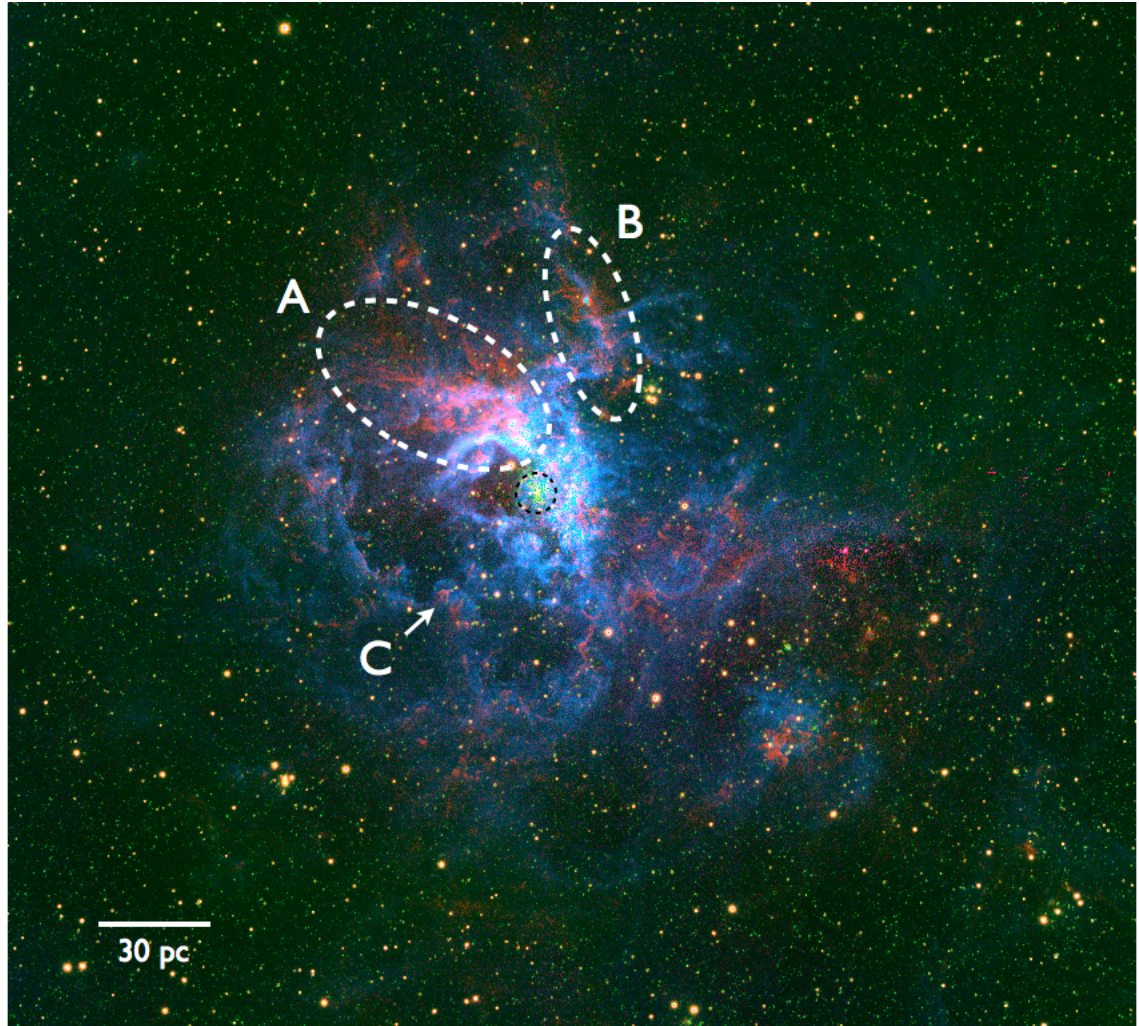


Figure 4.6: Same three-color composite image of 30 Doradus, as in Figure 4.4. H_2 -emitting areas of interest are marked by white dashed ellipses, including (1) the bright H_2 band to the northeast of R136 and (2) filaments pointing north-ward of R136. One elephant trunk to the southeast of R136 is identified by a white arrow.

rather smoothly distributed across Area A to R136, and it is also closer to the ionizing source in projected distance. If the H₂ emission were in front of the Br γ emission, given that molecular clouds have higher column density than ionized gas in an HII region, we would not have seen much of the Br γ at all, if the molecular cloud in front had homogeneous density distribution; or we would have seen more segregated Br γ clumps, if the molecular clouds were very porous. This region, Area A to R136, is also likely to be located behind R136. Again if it were in front of the ionizing source, the ionized gas traced by Br γ emission would have to be located behind the molecular clouds, which should not be the case as we have just discussed. This geometry is further supported by recent optical emission line studies by Pellegrini et al. (2011). They used the observed optical line ratios together with modeled ionization parameters, to determine where this region is located at with respect to R136. Most of the emission appears to originate from 60 pc behind R136.

Area B may share the same geometry as the regions we discussed above – this filament of molecular gas should be behind the Br γ emission and R136. Although the Br γ morphology is filamentary with rather poor correlation with the H₂ emission, Br γ is seen to partially coincide with the H₂ and CO emission in the area and much closer to R136, instead of being on the edge of the molecular clouds. This implies that the Br γ emission is not shielded by the molecular cloud, and we are viewing this region face-on, through a column of ionized gas, warm molecular gas, and cold molecular cloud (Figure 4.5).

Area C is likely located within 30 Dor with different inclination angles from the regions we discussed above. The bright Br γ emission in this region shows relatively poor spatial correlation with the H₂ emission. Br γ is seen closer to R136 in the projected plane of sky, and it envelopes the H₂ emission. This discontinuity of the Br γ and H₂ distribution implies that we are viewing Area C edge-on.

4.4.4 H₂ to Br γ Line Ratio

The morphological relations between H₂, Br γ , and CO emission are indicative that the observed H₂ emission traces the PDRs in 30 Dor. With data of only one H₂ emission line, we do not have sufficient information to firmly constrain the physical quantities in the PDR. Nevertheless, the line ratio of H₂ to Br γ is a useful guide to delineate the spatial distribution and structures of molecular gas relative to ionized gas in the PDRs, especially when a PDR is viewed face-on. Combining with numerical modeling efforts, the observed H₂ to Br γ line ratio offers a sketch of the physical properties of molecular and ionized gas in 30 Dor.

A line ratio map H₂ to Br γ is shown in Figure 4.7. The Br γ image was clipped at a 3σ level, pixels with S/N lower than 3σ detection were clipped. Pixels with S/N higher than 100σ detection in the H₂ image were masked and clipped, in order to exclude bright stars and to avoid confusion in measuring peak intensities in the image. The clipped H₂ and Br γ images were then smoothed by a $8''$ (1.6 pc) Gaussian kernel, and a line ratio map was produced.

In the vicinity of 30 Dor, the H₂ /Br γ ratio is in general very low (<0.05), due to the lack of H₂ emission. Higher H₂ /Br γ ratios are seen in Area A, Area B, filaments north of Area B, and some isolated elephant trunk features (including Area C) at the outer shells of 30 Dor. A clump to the northeast of R136 also show relatively high H₂ /Br γ line ratio, however this area is very likely to suffer from severe emission line contamination in the H₂ image, as we have discussed in § 4.3.3. Overall, the brighter H₂ /Br γ ratio areas in 30 Dor are clumpy with ratios of 0.25 to 0.7. Most areas show lower H₂ /Br γ ratio ~ 0.1 , which agrees with the same line ratio (derived from the total fluxes) observed in M16 (Levenson et al. 2000).

We show an expanded line ratio map of Area A in Figure 4.8, superimposed with H₂ emission line contours to provide a spatial and intensity perspective between H₂ emission line and H₂ to Br γ line ratio. The H₂ emission contour levels are the same as

those in Figure 4.7. In Area A, the H_2 to $\text{Br}\gamma$ ratio across the area seems quite clumpy, with some localized high ratio areas and ‘voids’. Expanded line ratio maps of Area B and Area C are shown in Figure 4.9 and Figure 4.10, in the same fashion as Area A. The line ratio at Area B overall is high (> 0.4) but poorly correlated with the higher H_2 emission, The two ‘limbs’ of high H_2 to $\text{Br}\gamma$ ratio in fact should suggest that the distribution of $\text{Br}\gamma$ across this area is fairly filamentary. Area C displayed a local maximum of H_2 to $\text{Br}\gamma$ line ratio, which also coincides with the high H_2 -emitting area at the tip of the elephant trunk.

4.5 Photoionization Models

4.5.1 Motivations

A series of H_2 emission lines, hydrogen recombination lines, and He recombination lines are present in the $2\ \mu\text{m}$ regime. We found evidence of additional emission line contamination (other than $\text{Br}\gamma$) in the Ks continuum, affecting continuum subtraction in the H_2 image (see § 4.3.3). Although we have empirically corrected for the contamination, and the estimated contamination level is in good agreement with similar type of observations in other H II regions, we will explore the contamination issue via numerical models of H II regions. Another motivation to carry out numerical simulations is to explore a wide range of physical conditions in H II regions and PDRs, and obtain emission line intensities as a function of physical conditions. The observed $\text{Br}\gamma$ and one single H_2 emission provide very limited information, but with the aid of numerical simulations, we are still able to learn something useful about the physical conditions in 30 Dor.

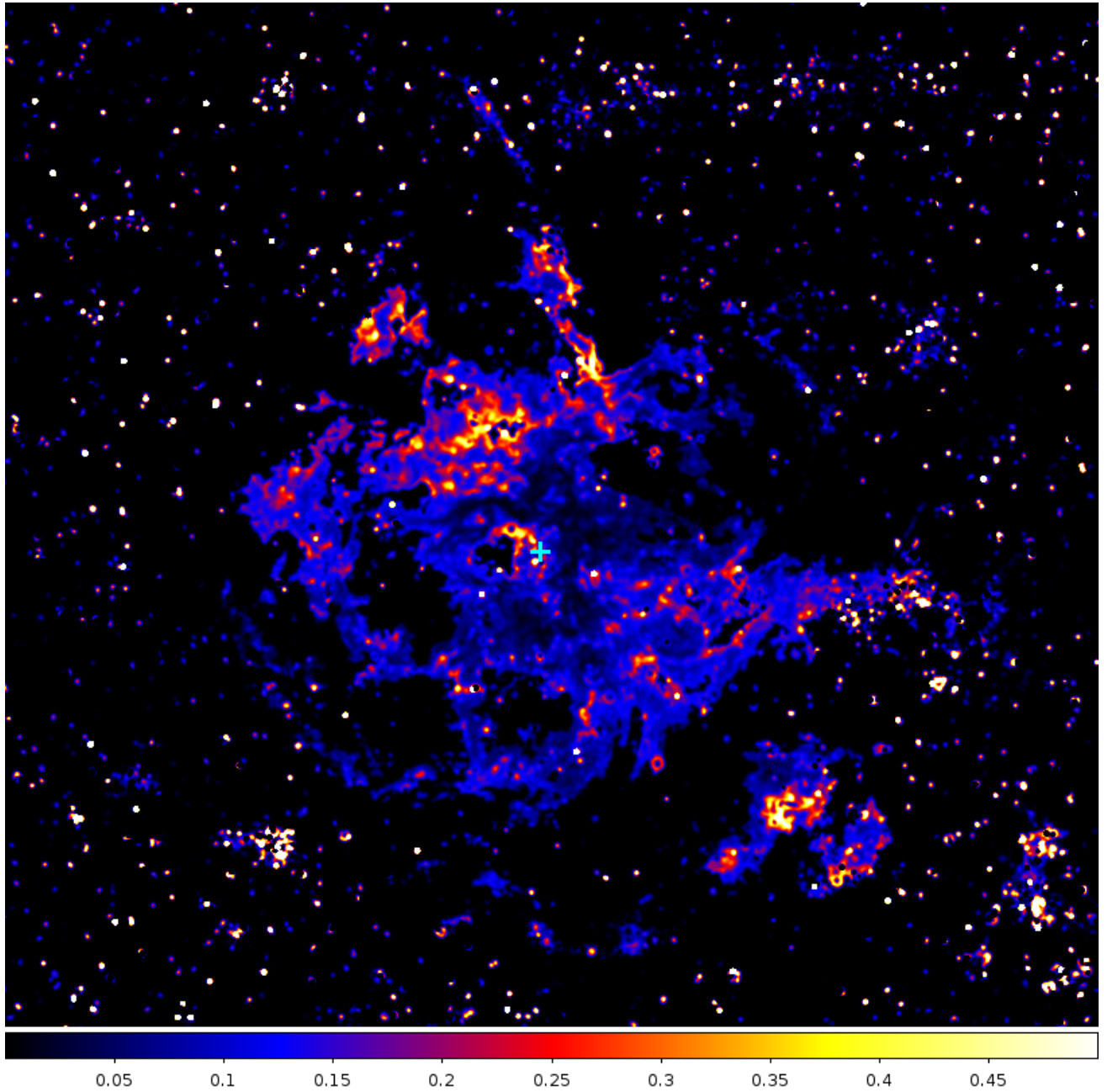


Figure 4.7: H_2 to $Br\gamma$ line ratio map of 30 Dor. H_2 and $Br\gamma$ images are smoothed by a $8''$ Gaussian kernel before the line ratio map was conducted. The color bar marks the H_2 to $Br\gamma$ ratio; R136 is marked by a cyan cross.

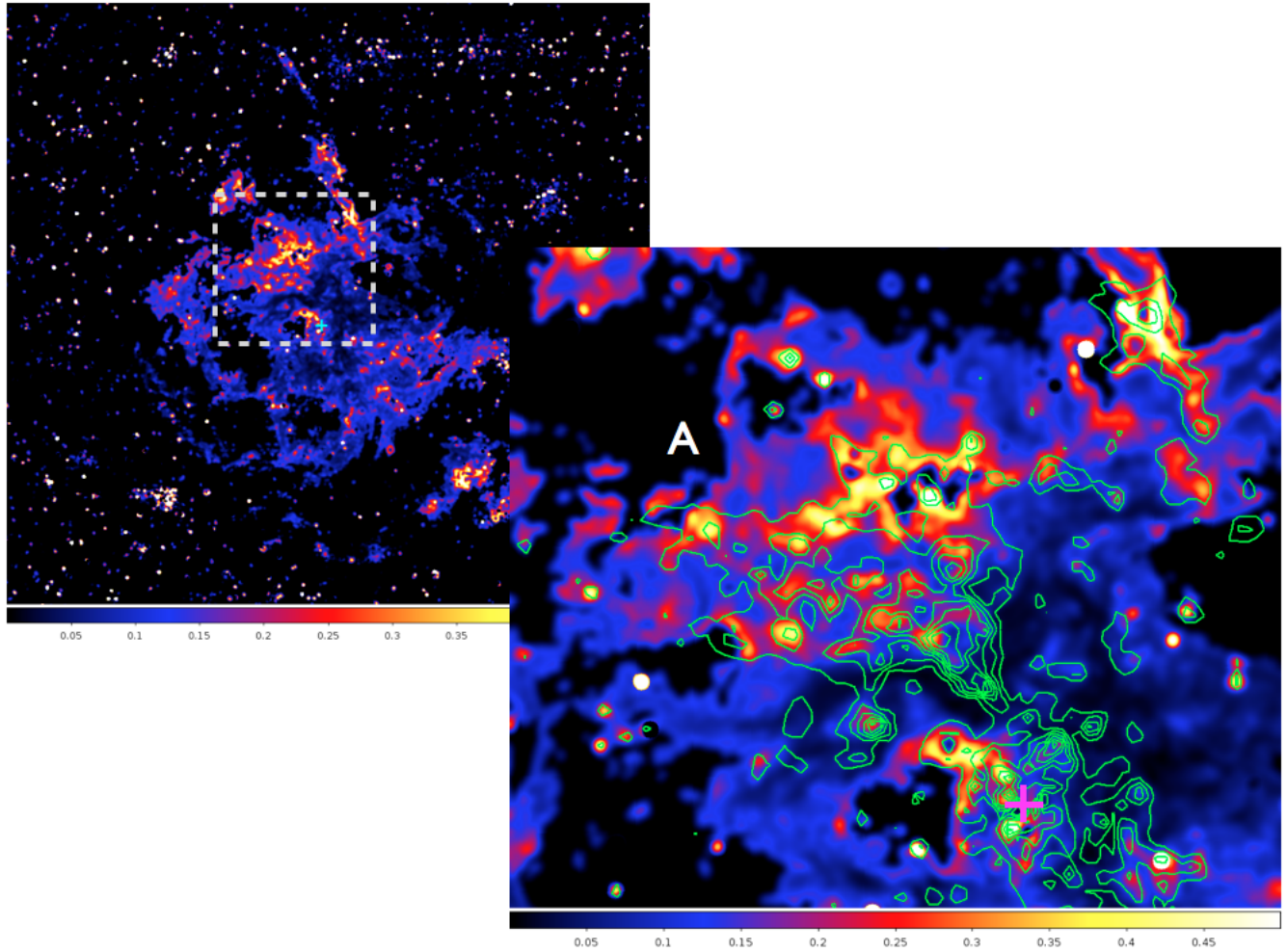


Figure 4.8: An expanded line ratio map of Area A. The area displayed on the right panel is marked by a gray box on the left panel which shows the full line ratio map of 30 Dor. The color bar marks the H_2 to $\text{Br}\gamma$ ratio; R136 is marked by a magenta cross. Note that we also plotted the H_2 emission contours (in green) based on an under-sampled, Gaussian-convolved H_2 image at every 10th pixel, in order to avoid contour crowding and to better present the overall distribution of H_2 emission.

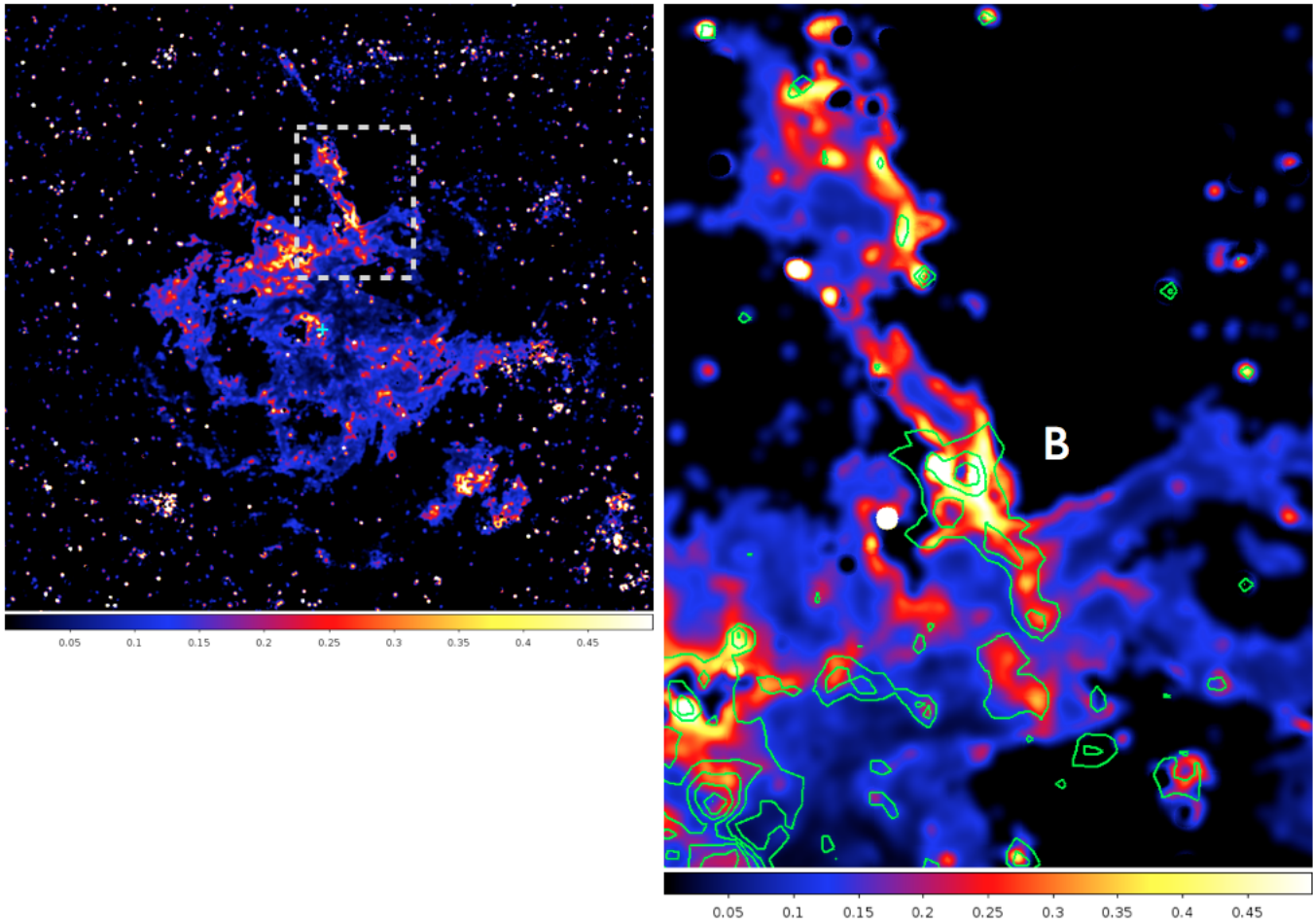


Figure 4.9: H_2 to $Br\gamma$ line ratio map of Area B. Symbols and contour levels are the same as in Figure 4.8.

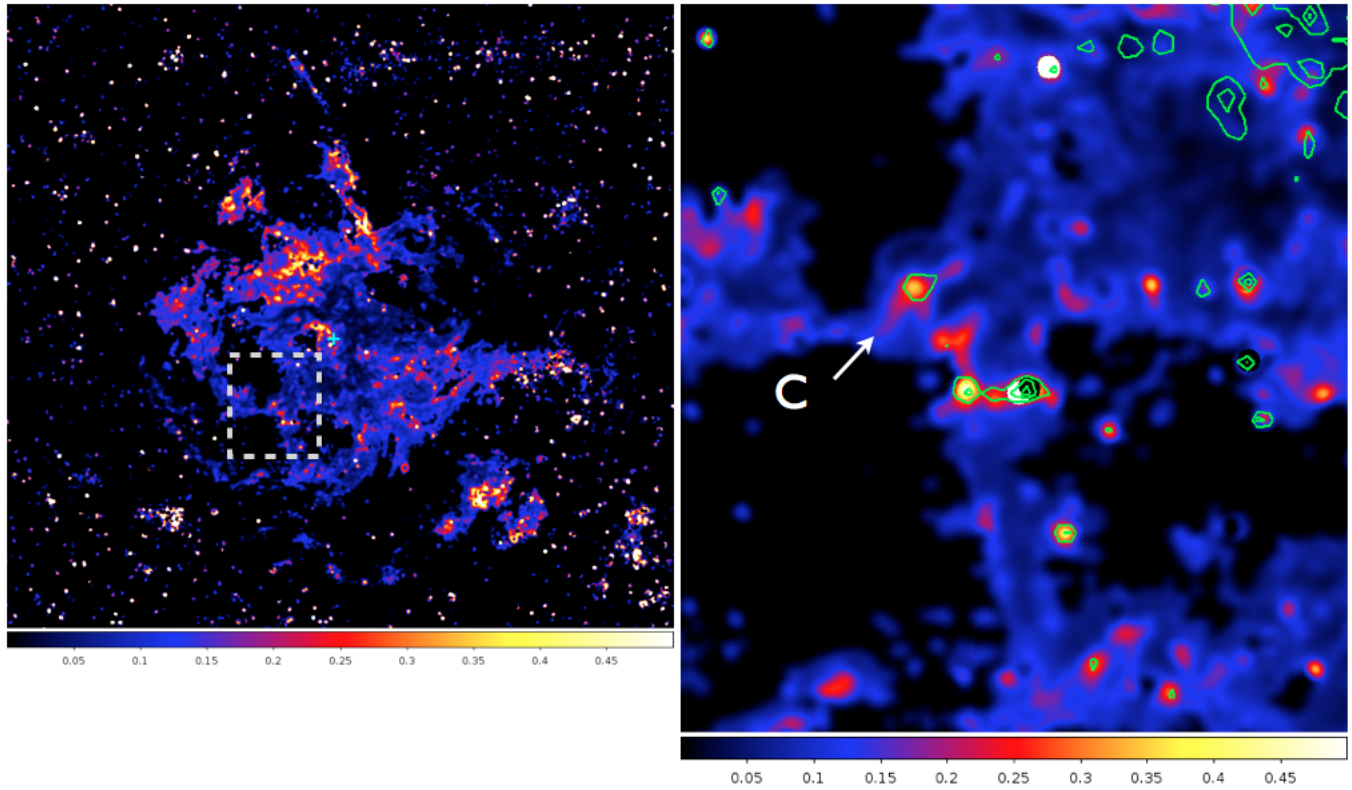


Figure 4.10: H_2 to $Br\gamma$ line ratio map of Area C. Contour levels and the cross are the same as in Figure 4.8. The white arrow marks the elephant trunk feature seen in Area C.

4.5.2 Model Parameters

We generated models of simple H II regions to study emission line intensities and physical conditions of molecular clouds in 30 Dor. First we used Starburst99 (Leitherer et al. 1999) to generate ionizing continuum spectra of a massive coeval star cluster at 2 Myr age, because the age of R136 is $\lesssim 2$ Myr (de Koter et al. 1998; Massey & Hunter 1998). The star cluster is assumed to be massive enough to fully sample the initial mass function, which has exponents -1.3 and -2.3 between stellar mass boundaries of 0.1, 0.5, and 120 M $_{\odot}$. We employed the Geneva high mass-loss evolutionary tracks with 0.4 solar metallicity. The Geneva high mass-loss tracks are optimized for modeling atmospheres of high mass stars and are recommended by Maeder & Meynet (1994). We adopt Pauldrach/Hillier atmospheres and the LMC UV line library. The atmospheres include non-LTE and line-blanketing effects (Smith et al. 2002) for O stars (Pauldrach et al. 2001) and Wolf-Rayet stars (Hillier & Miller 1998).

Starburst99 output continuum spectra are fed into Cloudy as the ionizing continuum of each simulated H II region. Pellegrini et al. (2010; 2011) suggested that the inner 15 pc of 30 Dor lacks ionized gas and thus molecular clouds, and most optical emission lines arise in the area 60 pc behind the star cluster R136. We therefore set the inner radii of the simulated H II regions at 60 pc with respect to the ionizing source. A wide density³ grid $\log(n_H)=1$ to 5 is incorporated in the calculations. We adopt the dust grain size distributions of the LMC (Pellegrini et al. 2011, private communication), and Cloudy's default ISM abundances at 0.4 solar metallicity. Each calculation stops when the cloud temperature drops to 50 K, well inside a PDR. Integrated line luminosities, Br γ at 2.17 μm , He I at 2.06 μm , H₂ 1–0 S(1) at 2.12 μm , H₂ 1–0 S(0) at 2.22 μm , and H₂ 2–1 S(1) at 2.25 μm , are calculated and recorded.

³The density at the inner edge of the H II region.

4.6 Model Results and Discussion

With the model parameter settings indicated in § 4.5.2, we first modeled HII regions under perfect force balance between thermal pressure of the cloud and incident radiation and wind pressure. At the distance 60 pc away from the ionizing source, ionized gas density in the force-balanced HII regions appears constant, however in the PDR region the cloud pressure can become unrealistically high when the ionized gas density is high. This is because our simple models do not include turbulence and magnetic field pressure terms, which are important in supporting molecular clouds. The modeled regions thus form artificially high thermal pressure beyond the ionization front (IF) in order to meet the force balance criterium. To resolve this problem, we turned to the constant density model. Although this setting does not represent a realistic HII region and PDR density profile, the $\text{Br}\gamma$ emission intensities calculated in both force balance and constant density models are consistent to within 1%, it is reassuring that the constant density models adequately represent the emission line spectra in the ionized gas, which is important in affecting the FUV spectra entered into PDR. We generated tables of emission line intensities as a function of the density grid and interpolated the observed line ratios using such tables, to obtain plausible range of physical conditions in 30 Dor.

4.6.1 Bright Emission Line Contamination

First we use our models to further explore the bright emission line contamination issue in our H_2 image. One calculated continuum spectrum of 30 Dor, which includes scattered continuum due to the presence of dust, is presented in Figure 4.11. We only focus on the continuum spectrum in the wavelength range of a Ks filter 1.99 to 2.31 μm , where the spectrum is shown in red, and the Ks filter bandpass is shown as a blue curve. $\text{Br}\gamma$ at 2.17 μm and H_2 1–0 S(1) at 2.12 μm are present in the modeled spectrum

Table 4.3. Emission lines within the Ks bandpass

Line	Wavelength
Br γ	2.17 μm
He I 2 ¹ P-2 ¹ S	2.06 μm
H ₂ 1-0 S(2)	2.03 μm
H ₂ 1-0 S(1)	2.12 μm
H ₂ 1-0 S(0)	2.22 μm
H ₂ 2-1 S(1)	2.25 μm

and are very close to the center of the filter, as expected. In addition, there is a prominent He I 2 ¹P-2 ¹S emission line at 2.06 μm to the blue end of the bandpass, and two more H₂ emission lines, H₂ 1-0 S(0) and 2-1 S(1), to the red end of the bandpass. The H₂ 1-0 S(2) line at 2.03 μm is negligible, especially since the filter transmission rate is less than 30% at that wavelength. Table 4.3 summarizes the emission lines in the Ks band.

Among all the emission lines present in the Ks bandpass, the He I line is the most plausible source of continuum contamination in our data. The calculated line ratios He I to Br γ at densities $\log(n_H)=1$ to 5 are 0.59, 0.60, 0.68, 0.72, and 0.65, respectively. This suggests that regardless the density in the H II region, the He I line will contribute 60% to 70% of the Br γ intensity to the continuum level, in satisfactory agreement with the empirically evaluated 60% level in § 4.3.3 and the 70% level in M16 (Levenson et al. 2000). Since Br γ emission is 7% of the Ks continuum, the He I contamination in the filter will be 4% to 5% of the Br γ brightness, assuming the distribution is the same.

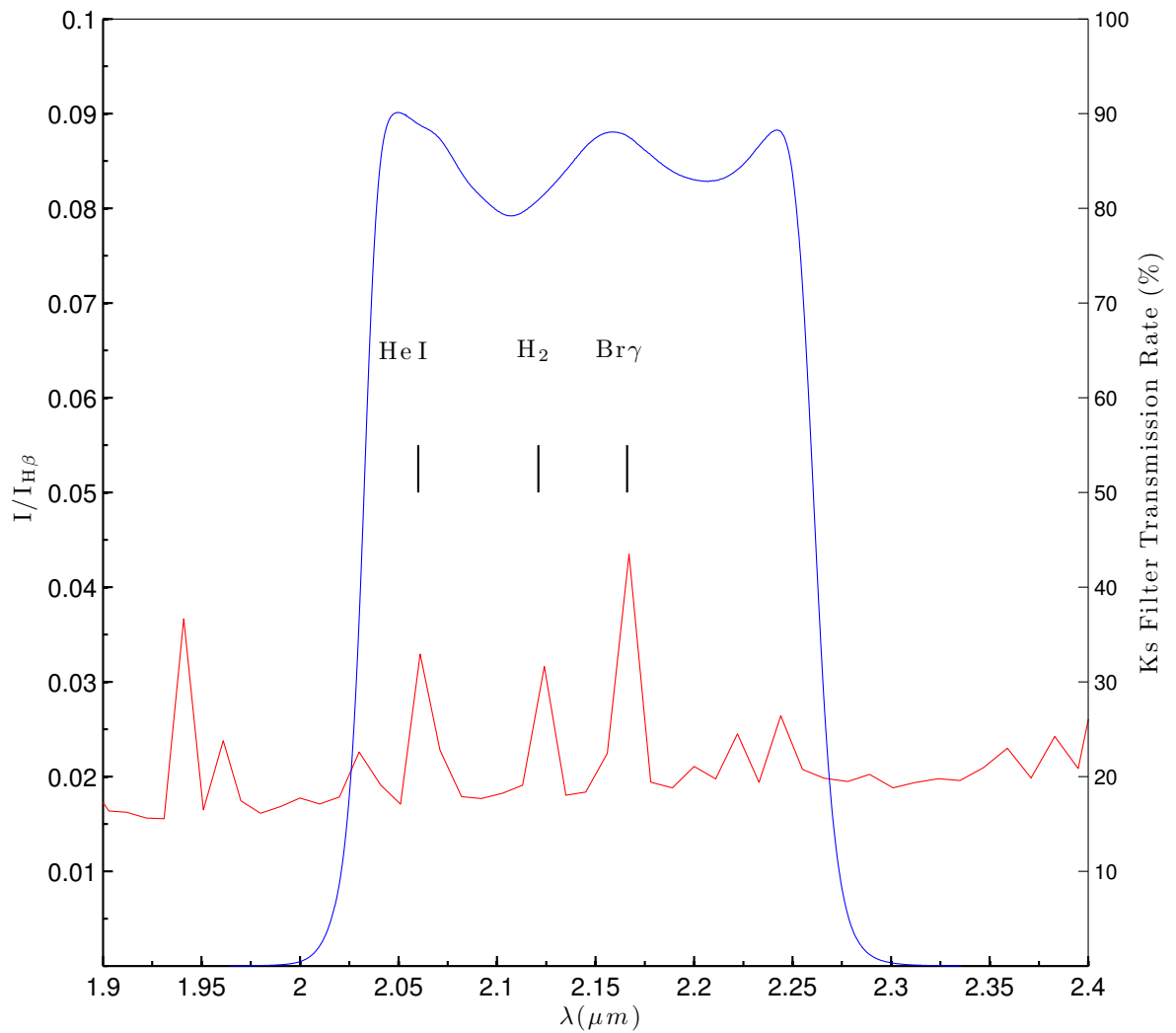


Figure 4.11: One Cloudy modeled continuum spectrum in the K-band regime, shown in the red line. The blue curve is the Ks filter bandpass as a function of wavelength and signal transmission rate. This spectrum is calculated at density $\log_{10} n_H = 3$, to demonstrate the bright emission lines within the Ks bandpass. We labeled the brightest emission lines Br γ at 2.16 μm , H₂ 1–0 S(1) at 2.12 μm , and He I 2 ¹P–2 ¹S at 2.06 μm . The line intensities are normalized to the H β intensity.

4.6.2 Origin of the H₂ 1–0 S(1) Line Emission

Molecular hydrogen emission lines in NIR can form in various ways, including (1) pure fluorescence excitation, (2) collisional excitation, and (3) shock-excited by fast protostellar outflows. The H₂ morphology, compared with Br γ and CO morphologies, excludes the protostellar outflow shock excitation, because the observed H₂ emission traces the ¹²CO distribution well, and H₂ is seen well correlated with Br γ emission. We have discussed this in § 4.4.1 and § 4.4.2. In order to distinguish fluorescence from collisional excitation, multiple transitions of rot-vibrational molecular hydrogen emission lines are required. However, our current observations only provide one transition of H₂ emission, which is insufficient to make such an assessment.

Nevertheless, we modeled simple H II regions with parameters described in § 4.5 and computed the Br γ and H₂ 1–0 S(1) emission intensities as a function of gas density $\log_{10} n_H = 1$ to 5 (Figure 4.12). In this figure, the H₂ to Br γ line ratio are shown in color contours, and the dashed line marks the ionized gas density ($10^{1.86} \text{ cm}^{-3}$) inferred from the X-ray emission assuming that ionized gas is force balanced with the X-ray emitting wind, which will be discussed in § 4.6.3. This density constrains the possible range of ionized gas density in 30 Dor, which should not be much higher or lower than this value.

Some regions in Area A show higher H₂ to Br γ ratio, 0.4 – 0.7, well correlated to the H₂ emission peaks, which implies that the H₂ emission is relatively higher than Br γ emission. Comparing to our modeled results in Figure 4.12, the molecular gas density at the corresponding line ratios is 10^2 to 10^3 cm^{-3} . Collisional excitation of IR H₂ emission lines is unimportant at density $\log_{10} n_H \lesssim 4$, and the observed H₂ emission is likely due to fluorescence excitation (Hollenbach & Tielens 1997). The simple comparison of observed and modeled line ratios suggests that H₂ in Area A is fluorescence and formed in the PDR of 30 Dor. The clumpiness of H₂ and H₂ to Br γ line ratio seen in Area A is indicative that FUV radiation could penetrate deeper into

the PDR.

In Area C the elephant trunk, the H₂ to Br γ line ratio measured at the area where H₂ emission is also highest is 0.35, at the ionized gas density $10^{1.86} \text{ cm}^{-3}$, the molecular gas density would be $10^{2.35} \text{ cm}^{-3}$. The modeled molecular gas density is lower than the density 10^4 cm^{-3} for collisional excitation to be important, therefore this implies that the H₂ emission in Area C is likely fluorescence as well. On the other hand, the Area C H₂ emission is seen with a separation of $\sim 3 \text{ pc}$ from its Br γ envelope. With the ionized gas density $10^{1.86} \text{ cm}^{-3}$, a depth of 3 pc would corresponds to $A_V \sim 0.34$. In our Cloudy model results, $A_V=0.34$ corresponds to a distance (from the illuminated cloud surface) of $\sim 4 \text{ pc}$, in satisfactory agreement with our observed H₂ and Br γ morphology. The ¹²CO emission lines forms inside a molecular cloud at a depth $A_V \sim 0.7$ (van Dishoeck & Black 1988), which further supports that the observed H₂ emission in Area C is formed inside the PDR but at a rather shallow depth. The fact that the mean separation of 3 pc between H₂ and Br γ emission seen in the outer shells and elephant trunk features in 30 Dor, which corresponds to a shallower depth ($A_V \sim 0.34$) is very indicative that these H₂ emission also come from the surface of the PDR, just like in Area C.

The relatively low molecular gas density (10^2 to 10^3 cm^{-3}) further indicates that the H₂ emission is formed very close to the surface of the molecular cloud in conjunction to the IF, where ionized gas density is $\sim 10^2 \text{ cm}^{-3}$.

4.6.3 Radiation Pressure

It has been debated whether radiation pressure from the ionizing source in giant HII regions , such as 30 Dor, is the main driving force and feedback mechanism. Lopez et al. (2011) assumed 30 Dor as a fully filled HII region and concluded that radiation pressure is the most dominating mechanism in driving the expansion of 30 Dor. However Pellegrini et al. (2011) reached the opposite conclusion, that radiation

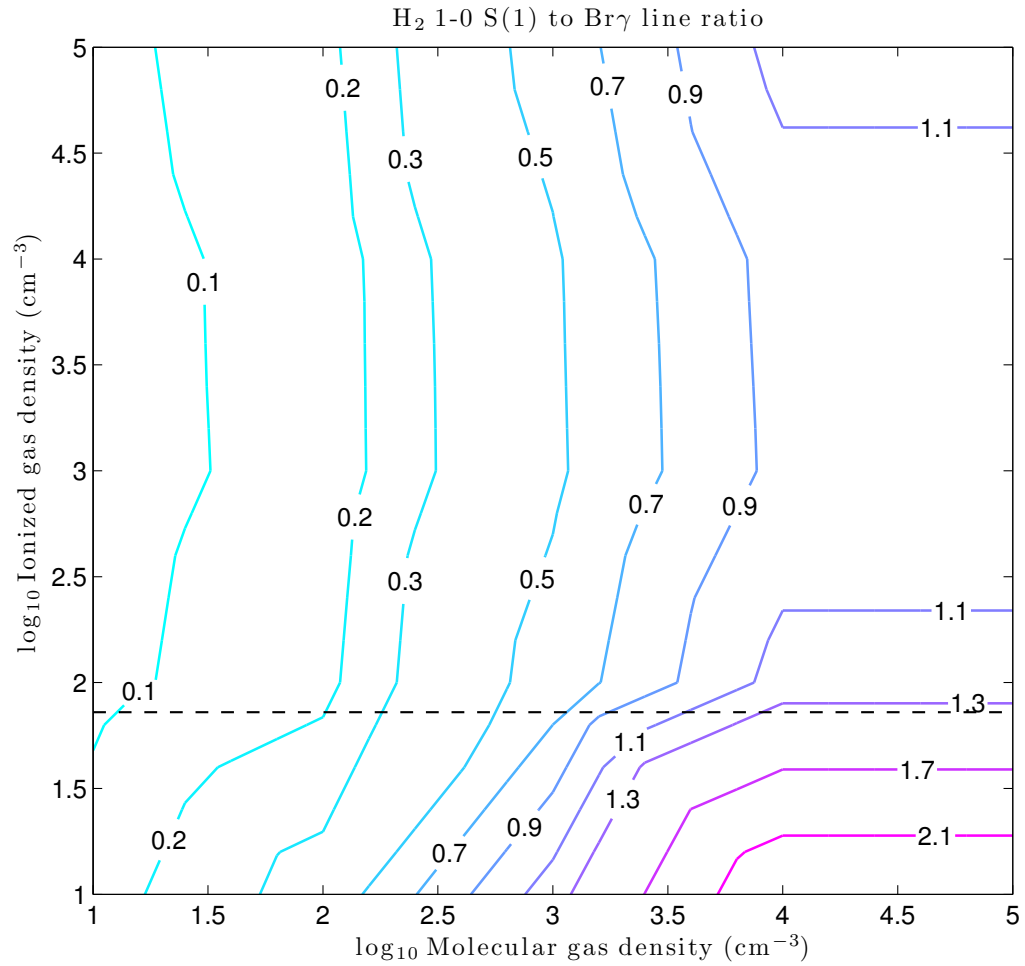


Figure 4.12: H₂ 1-0 S(1) to Br γ line ratio contours, as a function of ionized gas and molecular cloud density grids. The dashed line marks the ionized gas density derived from the X-ray emitting gas pressure (P_X) at ionized gas temperature $T=10,000$ K.

pressure is insignificant to contribute to the current moment of 30 Dor expansion, instead the X-ray emitting hot winds are the dominating force. We have discussed the role of radiation pressure, stellar wind pressure, and photoevaporative flows of clumpy ISM in H II regions in Chapter 2 . In this section, we explore the importance of each pressure at areas of interest using the 30 Dor data in the literature and our observations.

The soft X-ray emitting wind in the voids of 30 Dor is estimated to have the pressure $\frac{P_X}{k} \sim 7.2 \times 10^5 \text{ cm}^{-3} \text{ K}$ at a distance of 60 pc (Lopez et al. 2011). This pressure sets a limit for the ionized gas pressure. If 30 Dor is currently in force balance, the ionized gas pressure should equal to the X-ray emitting gas pressure, $\frac{P_{gas,i}}{k} \sim 7.2 \times 10^5 \text{ cm}^{-3} \text{ K}$. Therefore at an ionized gas temperature $T=10^4 \text{ K}$, the ionized gas density will be $n_{e,i}=10^{1.86} \text{ cm}^{-3}$, which agrees well with that derived from density sensitive Sulphur lines by Pellegrini et al. (2011).

The radiation pressure P_{rad} at Area A, 60 pc away from the star cluster, is derived to be $\frac{P_{rad}}{K}=1.92 \times 10^5 \text{ cm}^{-3} \text{ K}$, following $P_{rad}=\frac{L/c}{4\pi r^2}$, where we adopted $L=10^{42.65} \text{ erg s}^{-1}$, the luminosity of R136, and $r=60 \text{ pc}$. We found that $P_{rad}/P_{gas,i} \sim 0.26$, implying that radiation pressure at a distance of 60 pc does not appear to be the dominating pressure at Area A.

Alternatively, we evaluate the Γ parameter, which is the characteristic ratio of P_{rad} to $P_{gas,i}$ in a Strömgen H II region defined in Equation 2.2 in Chapter 2 :

$$\Gamma \simeq \frac{0.93}{T_4^{1.53}} (S_{51} n_{i*,4})^{1/3}. \quad (4.8)$$

Adopting $n_{i*,A}=n_{e,i}/10^4=0.007$, $T_4=1$, $S_{51}=4.17$, we found $\Gamma=0.29$, in good agreement with the $P_{rad}/P_{gas,i}$ derived above. Our Cloudy model results also suggest that H II regions with inner radii of 60 pc do not experience strong incident radiation pressure, their ionized gas density profile is constant and homogeneous towards the IF. Therefore we can draw the conclusion that at Area A, radiation pressure is not likely to be significant.

The effect of radiation pressure in Area C can be assessed by evaluating the Γ_c parameter. The Γ_c parameter describes the characteristic radiation to gas pressure ratio of a photoevaporative flow at the surface of a clump, as we have defined in Equation 2.19:

$$\Gamma_c = \frac{\bar{e}_i}{2.2kT_c} \left(\frac{\omega \alpha r_c S}{4\pi R_c^2} \right)^{1/2}. \quad (4.9)$$

Adopting $\bar{e}_i = 20$ eV, $\omega = 0.1$ to 0.2 , $r_c = 2$ pc, and $R_c = 33$ pc, $\Gamma_c \sim 0.04$ to 0.05 , indicating that radiation pressure is negligible at Area C. The derived Γ_c value is lower than Γ of its parent region, implying that the elephant trunk feature's radius of curvature is significantly smaller than the radius of IF of the parent region, as the analytical solution we have derived in Equation 2.20. This is confirmed by the overall H₂ morphology: the radius of curvature of the elephant trunk is much smaller than that of Area A, which is part of the 30 Dor H II region viewed face-on. Another important implication of small values of Γ_c in the region, is that the photoevaporative flows on the surface of the elephant trunk can freely flow away (towards the ionizing source) following the dynamics of ordinary photoevaporative flows (Bertoldi & McKee 1990), instead of being confined by radiation pressure if it were important. This may also be true in many other elephant trunk features or clumps seen in 30 Dor at a similar or greater projected distance. The net effect of clumps with photoevaporative flows in an H II region, is that it reduces the observed ionization parameter \mathcal{U}_{obs} from its maximum $\mathcal{U}_{obs,max}$ value, the same effect as the internal pressurization of stellar winds, which is also discussed in detail in § 2.4.

High spatial-resolution optical emission line studies Pellegrini et al. (2010; 2011) of 30 Dor shows that the majority of ionization parameter within the observed area is $\log_{10}(\mathcal{U}) \sim -2.5$ to -2 , including Area A, and few areas have $\log_{10}(\mathcal{U})$ approaching -1 . If the ionized gas layer seen at the surface of Area A represents parts of the 30 Dor H II region, the \mathcal{U}_{obs} is lower than the $\mathcal{U}_{obs,max}$ of a single H II region could have achieved, $\log_{10}(\mathcal{U}) = -1$. In Chapter 2, we discussed several physical effects which

can act to reduce $\mathcal{U}_{obs,max}$ in an H II region. From the above analysis, we can exclude the effect of radiation pressure at Area A in the current state of 30 Dor, leaving the other two sources, stellar winds and clumpy ISM, to be responsible for the reduction of $\mathcal{U}_{obs,max}$. The effect of internal pressurization of the hot wind is prominent, as P_X appears to be the dominating pressure in the region based on our simple calculation above and the study by Pellegrini et al. (2011). On the other hand, we indeed found many clumps and elephant trunk features in the H₂ image, which are all located at the outer edge of 30 Dor with a projected distance of 30 to 60 pc from R136. At these projected distances, photoevaporative flows can freely expand into the parent H II region, acting as an additional pressure in the H II region and thus further reduce $\mathcal{U}_{obs,max}$.

4.7 Summary

In this chapter, we presented the very first, fully calibrated H₂ 1–0 S(1) emission image, of the entire 30 Doradus nebula, as well as a Br γ image. In the data reduction process, we confirmed Br γ and He I emission line contamination in the Ks continuum via empirical analysis and Cloudy simulations. The uncertainty of the corrected H₂ flux will be about 3% of the Br γ flux.

The brightest H₂-emitting areas (Area A and Area B) are PDRs viewed face-on located behind the ionizing source R136, and the warm molecular clouds traced by H₂ appear to be clumpy. Those regions also trace the CO morphology well, further indicating that these PDRs are face-on, with layers of ionized gas, warm molecular gas, and cold molecular clouds.

Discontinuity of H₂ and Br γ morphology is found at the outer shells and elephant trunk features (such as Area C) in 30 Dor, suggesting that we are viewing these parts of the H II region edge-on. The mean separation between the Br γ envelope and H₂ clumps is 3 pc, which corresponds to $A_V = 0.34$. This depth agrees with the Cloudy

model results, and it suggests that H₂ emission is formed very close to the surface of the molecular clouds. The density of H₂-emitting gas is inferred from the Cloudy model results and the H₂ to Br γ line ratios. The molecular gas density is estimated to be 10² to 10³ cm⁻³, in good agreement with the ionized gas density $\lesssim 10^2$ cm⁻³, which further supports that the observed H₂ emission originates from the PDR in conjunction with the H II region.

We evaluated the characteristic ratio of radiation pressure to ionized gas pressure at Area A, which is the closest (in projected distance) H₂-emitting cloud in 30 Doradus. Radiation pressure is not likely to be important at this location, whereas the X-ray emitting gas pressure can be the dominating force. Radiation pressure is negligible at the surface of Area C, allowing its photoevaporative flow to freely escape and flow into the H II region. The \mathcal{U}_{obs} of 30 Dor is lower than the theoretical maximum value of a single H II region, and stellar winds and photoevaporative flows are likely to be the mechanisms acting to reduce $\mathcal{U}_{obs,max}$.

Chapter 5

Conclusions

We have explored the effects of massive star feedback in starburst systems, in both theoretical approaches and observational studies, and we focus on the physical properties and structures in HII regions and PDRs, which are under strong influence of radiation and stellar wind pressure in starburst galaxies.

First we investigated whether the dimensionless ionization parameter \mathcal{U} , can be a useful tool to measure the degree of radiation pressure feedback. \mathcal{U} directly reflects the importance of radiation pressure and gas pressure in an HII region, which can also be inferred from observations of forbidden line ratios. Single HII regions, regardless how luminous the ionizing source is, are never found to display arbitrarily high \mathcal{U} values. On the other hand, distant starburst galaxies often display a limiting \mathcal{U} value at $\log_{10}\mathcal{U} \lesssim -2.3$. In our theoretical analysis, we showed that in a radiation pressure dominated HII region, \mathcal{U} is limited to $\log_{10}\mathcal{U} \lesssim -1$. This is due to the fact that in a force balanced quasi-static HII region, when the incident radiation pressure is intense, ionized gas is highly compressed and confined in a thin layer with a steep density (and thus pressure) gradient, instead of having a homogeneous density profile. This process naturally limits \mathcal{U} values. The internal pressurization of stellar winds and photoevaporative flows add additional force to the region, which effectively further reduces \mathcal{U} . However, in most resolved single HII regions, the

numerical value of \mathcal{U}_{obs} is quite close to the theoretical maximum value, so we can draw a conclusion quite firmly that the stellar wind impact cannot be very high. On a galactic-scale, H II regions can be radiation pressure dominated. However, the observed ionization parameter $\log_{10} \mathcal{U}_{\text{obs}} \lesssim -2.3$ is likely limited by severe internal dust extinction. Nevertheless, these H II regions cannot be adiabatic wind bubbles either, otherwise their \mathcal{U}_{obs} values would be much lower.

We then extended the studies to understand the characteristic diagnostic $[\text{O III}]/\text{H}\beta$ and $[\text{N II}]/\text{H}\alpha$ line ratios of different H II region models. We modeled H II regions under combinations of radiation pressure and stellar, which result in Strömgen H II regions, radiation pressure dominated H II regions, stellar wind bubbles with radiation pressure, and energy-conserving wind bubbles without radiation pressure. We found that at a fixed ionizing spectrum and metallicity, there is a unique mapping between the line ratios and the $(\mathcal{U}, \text{density})$ grids. The radiation pressure dominated regions show saturated \mathcal{U} values, and the strongly wind-dominated bubbles with radiation pressure have much lower \mathcal{U} values. The only way to reach artificially high \mathcal{U} is to turn off radiation pressure. The assumption of an adiabatic wind bubble reaching high \mathcal{U} naturally breaks down, when the model reaches the high luminosity required to produce high \mathcal{U} values.

Next we turned to observational approaches to study the nearest starburst region, the 30 Doradus nebula in the LMC. We present the very first, fully calibrated H_2 1–0 S(1) emission image of 30 Doradus, together with a $\text{Br}\gamma$ image, taken by the NOAO Extreme Wide Field Infrared Imager. The morphologies of H_2 , $\text{Br}\gamma$, and archival CO data suggest that the bright H_2 -emitting regions extending from northeast to southwest of R136 is viewed face-on, with layers of ionized gas, warm molecular gas, and cold molecular cloud. Some clumps and elephant trunk features are found at the outer shell of 30 Doradus and they are likely viewed face-on. The observed H_2 spatially correlates well with $\text{Br}\gamma$, implying that these H_2 emission arise from the

photodissociation regions of 30 Doradus, and it is not excited by fast protostellar outflows or other shocks in molecular gas. From an analysis of the ratio of H₂ to Br γ lines, combined with photoionization modeling studies, we suggest that H₂ emission comes from molecular gas of density 10^2 to 10^3 cm⁻³, at a depth of $A_V \sim 0.34$. Therefore this layer of warm molecular gas is very close to the surface near the ionization front of the H II region.

We further assessed the importance of radiation pressure in 30 Doradus. We found that radiation pressure is not the dominating force in the current state of 30 Doradus, and that the photoevaporative flow at the surface of a selected elephant trunk can freely flow away from the molecular cloud, instead of being confined by radiation pressure. The pressurization of stellar winds and the injection of photoevaporative flows is likely at work to reduce the \mathcal{U}_{obs} of 30 Doradus from its theoretical maximum.

Chapter 6

Future Work

In this chapter, the discussion of future follow up work is divided into two parts, near and far future work.

For theoretical studies, we will adopt the quasi-static H II region models presented in Chapter 3 for our population synthesis code to simulate galactic regions with various physical parameters. This is a collaborative work with Silvia Verdolini and Xander Tielens at the Leiden University, and Mark Krumholz at the University of California Santa Cruz.

Spectroscopic follow up of H₂ emission line ratio studies will be the highlight of the immediate future observational work to pursue. This work will allow us to constrain excitation mechanisms of H₂ emission and physical quantities in the 30 Dor PDR. In addition, high spectroscopic-resolution studies of the selected starburst wind-molecular cloud interfaces of ionized and molecular gas will allow us to investigate their kinematics, and the mass-loading mechanism, which plays a crucial role in understanding the formation of galactic winds. In addition, our latest NEWFIRM [Fe II] image of 30 Dor will reveal the regions heated by shocks, which adds additional constraints to the H₂ excitation in PDRs.

Following our understanding of 30 Doradus, we will study other nearby galaxies which have more prominent and complicated starburst activities, such as NGC 1569

and M82, as part of the far future work. Ultimately, through detailed and high-resolution studies of nearby starburst systems, we will acquire a better understanding of star-forming galaxies in the early epoch of the Universe.

6.1 Near Future

6.1.1 Line Emission From Radiation-Pressurized HII Regions: Dynamics and Population Synthesis

We aim to understand the peculiar offset of high-redshift star-forming galaxies on the BPT diagram, which is distinctively different from the local samples. We first carried out quasi-static HII region models and explored the internal structures of individual HII regions, under the influences of radiation pressure and stellar winds. This work is described in Chapter 3. The next step is to investigate the effects of radiation pressure and stellar winds on the galactic scale, and the implications using the BPT diagram diagnostics.

In the collaborative work with Verdolini et al., we adopted the quasi-static HII region models which systematically include and exclude radiation pressure and stellar winds, and carried out population synthesis modelling to simulate galactic scale HII regions. The population synthesis code first generates HII regions following a stellar association mass function described in Williams & McKee (1997), and the HII region dynamics is described by the ambient ISM density distribution, stalling criteria, and the radiation trapping factor in each region, following the solutions in Krumholz & Matzner (2009). As the modeled HII regions evolve, a region is removed from the calculation when its stars, which provides 50% of the ionizing luminosity, leave the main sequence. The total emission line luminosities, $H\alpha$, $H\beta$, $[O III]$, and $[N II]$, of a galaxy is the sum over individual HII regions.

We then investigated individual H II regions with dynamical models, calculated their emission line ratio diagnostics on the BPT diagram, and compared the modeled regions with observations, i.e. individually resolved H II regions. We found that our H II regions successfully represented the resolved H II regions on the BPT diagram. On the galactic scale, our modeled H II regions can exceed the theoretical limit of starburst galaxies predicted by Kewley et al. (2001) when radiation pressure is significant. We were only able to produce star forming galaxies which cover parts of the parameter space of high-redshift galaxies on the BPT diagram. Our models tend to under predict the line ratio of $[\text{N II}]/\text{H}\alpha$ with respect to the observed high-redshift galaxies. This may be because (1) diffused ionized medium may be important in the higher redshift, which was not taken into account in our calculations, and (2) the ambient density distribution in higher redshift may be poorly described by the log-normal distribution at our models. We will investigate these two factors in future investigations.

6.1.2 Spectroscopic Studies of the 30 Doradus PDR

We will propose to observe a series of H₂ emission lines in the 2 μm regime in 30 Dor using SofI on NTT, or FLAMINGOS-2 on Gemini South. We aim to constrain excitation mechanisms of H₂ lines in the 30 Dor PDRs and study the corresponding physical conditions in the regions, in order to understand starburst feedback and subsequent star formation. With a recently acquired H₂ map of the entire 30 Dor as a guide for the proposed observations, we can carry out a spectroscopic study of H₂ emission in a starburst region with abundant spatial information and detail, to observationally quantify energy inputs from different excitation mechanisms of H₂ on local scales.

Scientific Goals

Massive bursts of stellar activity in starburst environments feed a prodigious amount of energy and momentum into the surrounding neutral clouds and unbind them (e.g., Krumholz et al. 2006). Feedback between a starburst and its PDRs is important in regulating the sequential star formation. This feedback is mediated by energy transfer across the ionized-neutral boundary of a PDR. Molecular hydrogen emission arises at this boundary, from both mechanical and radiative inputs. Determination of the H_2 excitation mechanisms in starburst PDRs therefore helps quantify their physical conditions. 30 Dor is the best target available in the sky to study starburst feedback and the physical conditions in the PDRs where subsequent star formation takes place. It hosts a giant HII region ionized by the young (2 Myr) star cluster R136. R136 produces H-ionizing photons at the rate of $10^{51.6} \text{ s}^{-1}$ and contains numerous O and B stars, which makes 30 Doradus a starburst prototype. While the nearest starburst galaxies are several Mpc away and the corresponding spatial resolution is poor, 30 Doradus is only 50 kpc away. It provides the spatial resolution ($1''=0.2 \text{ pc}$) to explore the physical nature of molecular hydrogen emission and its hosting PDR on local scales for a direct comparison to more distant starburst regions. Molecular hydrogen is excited either by far-ultraviolet radiation with energy $11.2 \text{ eV} < h\nu < 13.6 \text{ eV}$ or by shocks. Shocked systems are collisionally excited, which gives a emission line spectrum distinct from fluorescence excited H_2 . For shock excited H_2 , the logarithm of H_2 column density is a linear function of the upper-level excitation energy, whereas fluorescence excited H_2 does not follow the linear relation, instead each vibrational level will have its own 'branch' in the plot. Another way to distinguish shock and fluorescence excited H_2 emission is to compare the observed ortho/para H_2 line ratios. The predicted ortho/para H_2 line ratio is 3 in the shock excited case, which is also confirmed by many observations. On the other hand, the ortho/para ratio is around 2 or lower in the fluorescence excited case, which has been observed in some external

galaxies (Puxley et al. 2000). These spectral signatures allow us to observationally separate and quantify energy inputs from the two mechanisms, once we know where to look.

We have conducted fully calibrated H_2 1–0 S(1) and $\text{Br}\gamma$ maps of the entire 30 Doradus, as we have extensively discussed in Chapter 4, which serves as an excellent guide for spectroscopic follow up observations. This is the first time one can carry out a spectroscopic study of H_2 emission in a starburst region with abundant spatial information and detail, because now we have complete information of the H_2 emission distribution in 30 Dor. Poglitsch et al. (1995) suggested that the molecular gas in 30 Dor is warm and dense (2000K and 10^6 cm^{-3}) based on H_2 1–0 S(1) to $\text{Br}\gamma$ ratio in a very small area near R136. However, combining our observed H_2 to $\text{Br}\gamma$ morphologies, line ratios, and Cloudy simulations, we find that the H_2 emission is formed inside the PDRs very close to the surface of the molecular cloud ($A_V \sim 0.3$), and where the molecular gas density is 10^2 to 10^3 cm^{-3} . This indicates that there must be density inhomogeneities in the molecular clouds in 30 Doradus rather than a single density, and the H_2 emission line may form at lower density than average. An incomplete spatial sample certainly biases the interpretation of H_2 excitation mechanism and the derived physical parameters in the PDR.

We will extend this image-based work with spectroscopic determination of H_2 line ratios. SofI on NTT provides very long slits of $290''$, which corresponds to 58 pc at the distance of 30 Doradus. We can efficiently observe H_2 emission lines across a variety of morphologically selected features simultaneously, such as the areas of interest we have identified in Chapter 4. Alternatively, we can use the NIR spectrometer FLAMINGOS-2 on Gemini South. FLAMINGOS-2 offers both the long-slit mode and multi-object mode. When used in the long-slit mode, FLAMINGOS-2 provides slit length of $263''$, very much comparable to SofI's slit length. When used in the multi-object mode, FLAMINGOS-2 provides a $2' \times 6'$ rectangular field, which is a sufficient

field of view to carry out spectroscopic observations in the areas of interest in 30 Dor. The multi-object mode also enables very efficient observations, in contrast to the NTT long slits of which observers must observe areas with one slit at a time. Although the spectroscopic observations will be seeing limited, we can still achieve much higher spatial resolution in 30 Dor than in external galaxies. SofI's and FLAMINGOS-2's relatively narrow slit width ($0.6''$ for SofI and $0.18''$ to $1.44''$ for FLAMINGOS-2) also provide higher sensitivity of emission lines, which benefits the proposed science goal.

Proposed Observations

We will propose to observe 30 Dor using SofI on NTT or FLAMINGOS-2 on Gemini South (depending on the instrument availability) with a series of H₂ emission lines, including H₂ 1–0 S(1) at $2.12 \mu\text{m}$, H₂ 1–0 S(0) at $2.22 \mu\text{m}$, and H₂ 2–1 S(1) at $2.25 \mu\text{m}$. These H₂ lines emit at similar wavelengths, therefore our data will be nearly independent of foreground extinction. We will place slits across areas of interest as indicated in Figure 4.6, Chapter 4, to perform a more complete spatial study of H₂ emission lines. We will construct the logarithm H₂ column density vs. upper-level excitation energy diagram with observed H₂ line ratios, fit a shock model in the diagram which should be a linear correlation, and compare the fitted shock model with the observed data. If the data shows individual vibrational branches instead of a linear correlation, we can tell that the H₂ lines are largely fluorescence excited. We will also derive the ortho/para ratios based on the H₂ data, compare the ratio with the nominal value of 3 which is indicative of shock excited H₂. Furthermore, we are aware that fluorescence excited H₂ emission lines can sometimes mimic the shock excited lines in the H₂ column density vs. upper-level excitation energy diagram. In a denser region where the cloud density reaches the critical density of the line, H₂ can be collisionally excited and results in more thermalized spectra.

We have recently mapped 30 Dor using NEWFRIM in $1.64 \mu\text{m}$ [Fe II] emission,

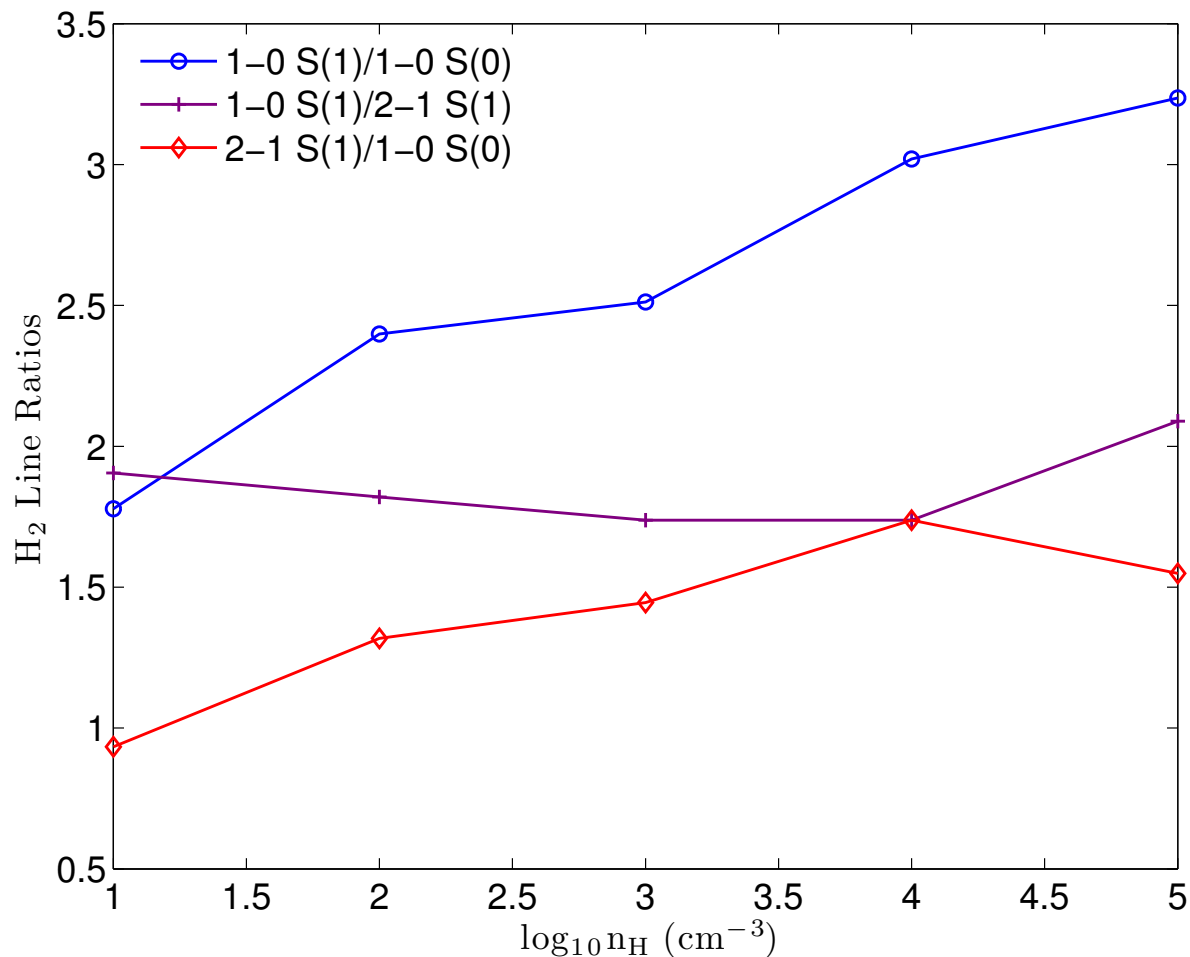


Figure 6.1: Modeled H_2 emission line ratios as a function of molecular gas density.

which serves as a guide to identify the locations of shocks independent of the H_2 distribution. The H_2 emission line ratios we have calculated using the Cloudy models described in § 4.5 (see Figure 6.1) serve as an additional guide to interpret observed H_2 line ratios and to constrain the molecular gas densities.

6.1.3 High-resolution Spectroscopic Studies of Mass-Loading in 30 Doradus

We will propose to observe H_2 1-0 S(1) and $\text{Br}\gamma$ emission lines in 30 Doradus using the CRIRES spectrograph on the VLT. We aim to constrain the important astrophysical

phenomenon, mass-loading, by studying detailed kinematics of warm neutral and hot ionized gas at wind-ambient cloud interfaces with high velocity resolution. We will map the emission measure and gas kinematics as a function of cloud geometry with parallel slits to produce maps that are equivalent to integral field maps. Our unique observations will provide the very first opportunities to understand mass-loading, its impact on sequential star formation in starburst regions, and its efficiency in cooling tenuous starburst winds.

Scientific Goals

Mass-loading, a poorly understood phenomenon, plays a vital role in understanding subsequent star formation in starburst environments. Dense gas is incorporated into starburst winds and cools the wind via mass-loading. However the cooling efficiency remains poorly understood as well, which is a crucial parameter in affecting the giant H II region dynamics and the formation of galactic outflows (Veilleux et al. 2005). We will investigate the interaction between the stellar wind and radiation field from R136 and the surrounding neutral clouds in 30 Dor. Mass-loading of starburst winds can occur via photoevaporation, wind ablation, or thermal conduction (Pittard 2007). The first two are the most relevant to clouds directly exposed to intensive stellar wind and radiation. In the ablation case, we consider that ionized gas is strongly confined and stripped by intensive starburst winds and radiation field (Arthur & Lizano 1997). This phenomenon leads to strong mixing between the hot wind and warm phases, and the broad optical emission lines detected in starburst galaxies by Westmoquette et al. (2007; 2009) are indicative of this effect. However, their low spectral resolution and the complexity of the regions studied precludes a detailed understanding of mass-loading, and the optical emission line tracers suffer from severe extinction.

We intend to test the mechanism whether photoevaporation or wind ablation is most responsible for mass-loading. In order to constrain the mass-loading mechanism,

it is crucial to resolve and determine the absolute velocity of ionized gas with respect to neutral cloud at the wind-ambient cloud interface, and to find whether the ionized gas is moving towards or away from the ionizing source. For photoevaporation, ionized gas has maximum speed $\lesssim 20 \text{ km s}^{-1}$ (Bertoldi & McKee 1990) and flows towards the ionizing source. Even with strong magnetic fields aligned parallel to the direction of the photoevaporative flows, ionized gas can only flow at a speed up to 30 km s^{-1} (Henney et al. 2009). On the other hand, wind-ablated ionized gas is swept away from the ionizing source in much higher velocity, although such velocity is very poorly constrained. The mass-loss rate of neutral clouds is a direct function of ionized gas velocity at the cloud surface in either mass-loading mechanism. It is therefore important to pin down detailed ionized gas kinematics at the wind-ambient cloud interface, which can be achieved by measuring velocities of neutral and ionized gas motion. Our fully calibrated H_2 and $\text{Br}\gamma$ images of 30 Dor serve as excellent guides to identify ionized gas and neutral cloud interfaces for the proposed spectroscopic observations, which also allow us to sample many of such interfaces. By constraining the mass-loading mechanism, we will be able to determine the impact of radiation pressure and stellar winds on a local scale, the fates of globules close to the super star cluster and the mass loading of the hot phase. Our unique observations will offer the first ever opportunities to understand the important astrophysical phenomenon, mass-loading, and its impact on star formation and cooling of starburst winds in starburst environments.

Proposed Observations

We will propose to observe wind-ambient cloud interfaces in 30 Dor using CRIRES on VLT with H_2 1–0 S(1) emission at $2.12 \mu\text{m}$ and $\text{Br}\gamma$ emission at $2.16 \mu\text{m}$. Both H_2 1–0 S(1) and $\text{Br}\gamma$ lines emit at very similar wavelength, our data will be nearly independent of foreground extinction. With CRIRES, we can measure the kinematics

of warm neutral gas and ionized gas with velocity resolution of 6 km s^{-1} , which can well resolve ionized gas thermal speed of 10 km s^{-1} . Therefore the absolute velocity of ionized gas can be determined by the H_2 and $\text{Br}\gamma$ velocities, and the direction of gas motion will be identified as well. This allows us to constrain whether mass-loading occurs via photoevaporation or wind-ablation, by identifying the direction and velocity of the photoevaporative flows. Furthermore, we will place parallel slits at selected interfaces to produce maps that are equivalent to integral field maps. The ‘data cubes’ provides information of emission measure and gas kinematics as a function of cloud geometry, then the electron density and pressure of warm neutral gas and ionized gas can be evaluated accordingly. We will further estimate the mass-loss rate of evaporated or ablated clouds, investigating how efficiently either mass-loading mechanism can cool the tenuous starburst wind.

6.2 Far Future

30 Doradus is the Rosetta stone, the gateway for understanding detailed mechanisms of massive star feedback, and its impact on subsequent star formation. We have collected H_2 data of 30 Doradus, which will guide our follow up spectroscopic studies and allow us to constrain the physical properties of the PDR. The next step is to ‘scale-up’, to extend these observational studies to systems with more vigorous starburst activities. NCG 1569 and M82 are the next targets to pursue similar kinds of studies we have been working on in 30 Dor, in order to investigate the collective effects of feedback from more than one massive star cluster. NGC 1569 is a nearby (2.2 Mpc) dwarf galaxy which hosts 2 super star clusters (SSCs), whereas M82 is at a distance of 3.6 Mpc and harbors hundreds of SSCs. Both galaxies have been well studied, and numerous multi-wavelength data have been collected. However, the key piece of information – full map of spatial distribution and intensities of H_2 emission in PDRs

in nearby starburst galaxies, remains far from being complete. Detailed spectroscopic studies of ionized gas and molecular cloud interactions are also sparse or have not yet been conducted. Galaxies in the early epoch of the Universe form stars at a higher rate, and the stars have lower metallicity. These properties at least lead to harder radiation fields and less efficient cooling in the ISM. How would feedback from massive stars operate in those epoch? Would it simply be a scale-up of the mechanisms we have learned in 30 Doradus? Exploring feedback mechanisms in NGC 1569 and M82 may ultimately allow us to understand star formation in the early Universe.

Chapter 7

Appendix

7.1 A. Force balance and pressure equilibrium

The momentum equation for fluid flow is

$$\frac{\partial}{\partial t} \rho \mathbf{v} + \nabla \cdot (\rho \mathbf{v} \mathbf{v} + P \mathbf{I}) = \mathbf{f}_{\text{rad}} + \mathbf{f}_{\text{mag}}$$

where \mathbf{I} is the unit tensor and \mathbf{f}_{rad} and \mathbf{f}_{mag} are the magnetic and radiation force per unit volume, respectively. As elsewhere in Chapter 2, P (with no subscript) is the gas pressure. Our analysis is based on a quasi-static idealization of an H II region in which $v \rightarrow 0$ and $\frac{\partial}{\partial t} \rightarrow 0$, so this simplifies to a statement of force balance:

$$\nabla P = \mathbf{f}_{\text{rad}} + \mathbf{f}_{\text{mag}}.$$

As discussed by Mihalas & Mihalas (1984), $\mathbf{f}_{\text{rad}} = \nabla \cdot \mathbf{P}_{\text{rad}}$ where \mathbf{P}_{rad} is the radiation pressure tensor. In spherical symmetry, $\mathbf{f}_{\text{rad}} = -\frac{\partial}{\partial r} P_{\text{rad}} - (3P_{\text{rad}} - u_{\text{rad}})/r$ for radiation pressure P_{rad} and energy density u_{rad} . Splitting the radiation into radially free-streaming and isotropic components $P_{\text{rad}} = P_{\text{rad,fs}} + P_{\text{rad,is}}$ with energy densities $u_{\text{rad}} = P_{\text{rad,fs}} + 3P_{\text{rad,is}}$, we have $\mathbf{f}_{\text{rad}} = -\frac{\partial}{\partial r} P_{\text{rad,is}} - r^{-2} \frac{\partial}{\partial r} r^2 P_{\text{rad,fs}}$. Our free-streaming radiation is meant to represent attenuated radiation from the central source, whose luminosity at r is $L(r)$ so that $P_{\text{rad,fs}}(r) = L(r)/(4\pi r^2 c)$, whereas the isotropic

radiation field represents trapped line emission, especially Lyman α , as well as the diffuse Lyman continuum radiation emitted during recombinations to the ground state.

Inserting this and $\mathbf{f}_{\text{mag}} = -\nabla P_{\text{mag}} + (\mathbf{B} \cdot \nabla)\mathbf{B}/(4\pi)$ into the force balance equation and writing only the radial component,

$$\frac{\partial}{\partial r}P = -\frac{\partial}{\partial r}P_{\text{rad, is}} - r^{-2}\frac{\partial}{\partial r}r^2P_{\text{rad, fs}} - \frac{\partial}{\partial r}P_{\text{mag}} + (\mathbf{B} \cdot \nabla)B_r.$$

Writing $P_{\text{tot}} = P + P_{\text{rad}} + P_{\text{mag}}$ and integrating across a range $r_{\text{in}} \rightarrow r_{\text{in}} + \Delta r$,

$$\Delta P_{\text{tot}} = -2 \int_{r_{\text{in}}}^{r_{\text{in}}+\Delta r} \frac{L(r)}{4\pi r^3 c} dr + \int_{r_{\text{in}}}^{r_{\text{in}}+\Delta r} \frac{(\mathbf{B} \cdot \nabla)B_r}{4\pi} dr.$$

This shows that the change in P_{tot} is bounded across any range of r . Since $L(r)$ is non-increasing, the magnitude of the first integral is maximized if radiation and matter do not interact, so that $L(r)$ remains constant:

$$2 \int_{r_{\text{in}}}^{r_{\text{in}}+\Delta r} \frac{L(r)}{4\pi r^3 c} dr \leq 2P_{\text{rad, fs}}(r_{\text{in}}) \left(1 - \frac{r_{\text{in}}^2}{r_{\text{out}}^2}\right) \rightarrow 4\frac{\Delta r}{r_{\text{in}}}P_{\text{rad, fs}}(r_{\text{in}})$$

where the arrow represents the limit $\Delta r \ll r_{\text{in}}$. Moreover, the magnetic tension term $(\mathbf{B} \cdot \nabla)B_r/(4\pi)$ is of order $2P_{\text{mag}}/R_c$ if R_c is the curvature radius of the magnetic field. When ionized gas is compressed in a thin shell of width Δr , R_c likely to be intermediate between Δr and r . We can therefore say in general that when the shell is thin,

$$\frac{|\Delta P_{\text{tot}}|}{P_{\text{tot}}} \lesssim 4\frac{\Delta r}{r}\frac{P_{\text{rad, fs}}r_{\text{in}}}{P_{\text{tot}}} + 2\frac{\Delta r}{R_c}\frac{P_{\text{mag}}}{P_{\text{tot}}},$$

which is typically quite small: force balance implies near-constancy of the total pressure.

7.2 B. Dusty, radiation-dominated HII regions: the planar limit

We are interested in the properties of the Dr11 solutions in the limit that ionized gas is restricted to a geometrically thin shell, as occurs in radiation-dominated regions

when $\Gamma > 1$ and (as we see below) $\gamma > 1$. We restrict equations (1)-(3) of Dr11 to the limit of a thin shell (constant r) and combine them to find

$$\frac{d\phi}{d\tau} = -\phi - \tilde{n} \quad (7.1)$$

(we use τ for the local dust optical depth, reserving τ_d for that of the entire region) and

$$\frac{d\tilde{n}}{d\tau} = \gamma^{-1} (\phi + \beta e^{-\tau} + \tilde{n}) \quad (7.2)$$

where $\tilde{n} = n/n_{\text{ch}}$ for a characteristic density

$$n_{\text{ch}} = \frac{S\sigma_d}{4\pi R_{\text{IF}}^2 \alpha} \quad (7.3)$$

which is defined so that, when $\tilde{n} = \phi = 1$, dust absorption and ionization consume ionizing photons at equal rates.

The solution with $\tilde{n} = 0$ and $\phi = 1$ at $\tau_d = 0$ is

$$\phi(\tau) = \frac{\gamma(\beta + 1)e^{-\tau(\gamma-1)/\gamma} - \beta[(\gamma - 1)e^{-\tau} + 1] - 1}{\gamma - 1} \quad (7.4)$$

and

$$\tilde{n}(\tau) = \frac{1 + \beta}{\gamma - 1} \left[1 - e^{-\tau(\gamma-1)/\gamma} \right], \quad (7.5)$$

valid up to $\tau = \tau_d$, for which $\phi(\tau_d) = 0$, so that

$$\gamma(\beta + 1)e^{-k\tau_d} = \beta(\gamma - 1)e^{-\tau_d} + \beta + 1$$

for $k = \gamma/(\gamma - 1)$, which shows that when $\gamma \gg 1$ and $k \rightarrow 1$, $\tau_d \rightarrow \ln[(\gamma + \beta)/(\beta + 1)]$.¹ Because of the planar geometry (Appendix 7.1) these solutions obey pressure equilibrium, $4\pi r^2 p = (L_n e^{-\tau} + L_i \phi)/c$, or in dimensionless terms,

$$\gamma \tilde{n} + \phi + \beta e^{-\tau} = 1 + \beta \quad (7.6)$$

so that, at the IF, $\tilde{n} = [1 + (1 - e^{-\tau_d})\beta]/\gamma$.

¹A better approximation at moderate γ is $\tau_d \simeq \ln(f) + 0.5e^{-f/8}$, where $f = (\gamma + \beta)/(\beta + 1)$.

In the special case $\gamma = 1$, we find

$$\phi(\tau) = (1 + \beta)(1 - \tau) - \beta e^{-\tau}; \quad \tilde{n}(\tau) = (1 + \beta)\tau. \quad (7.7)$$

Within these solutions,

$$\Xi_{i,\text{em}} = \frac{\int_0^{\tau_d} \phi \, d\tau}{\gamma \int_0^{\tau_d} \tilde{n} \, d\tau}. \quad (7.8)$$

and the fraction of ionizing starlight caught by gas is

$$\begin{aligned} f_{\text{ion}} &= 1 - f_{\text{dust}} = \int_0^{\tau_d} \tilde{n} \, d\tau \\ &= \frac{1 + \beta}{\gamma - 1} \left[\tau_d - \frac{\gamma}{\gamma - 1} \left(1 - e^{-\frac{\gamma-1}{\gamma} \tau_d} \right) \right] \end{aligned} \quad (7.9)$$

$$\simeq 1 - \exp[0.7(\ln \tau_d - 1) - (\ln \tau_d)^2/6], \quad (7.10)$$

where the final approximation is correct to 2% for the entire range of figure 7.1. In the very dusty limit $\gamma \gg 1$, for which $\tau_d \sim 3$, the recombination luminosity is suppressed by a constant fraction which is roughly $(1 + \beta)\tau_d/(\gamma - 1)$.

The radial coordinate can be determined by integrating $dr = d\tau/(n\sigma_d)$. Because of the low density at the inside of the slab, radiation force is transmitted to the gas only through the dust, leading to a constant acceleration and (since the temperature is assumed to be constant) an exponential interior density distribution $n \propto \exp[(1 + \beta)n_{\text{ch}}\sigma_d r/\gamma]$.

Note, however, that equation 7.5 implies a negative density if $\gamma \leq 1$; this simply means that the solution is incompatible with the imposed inner boundary of zero density and optical depth. For such low dust opacity, the solution must extend inward to join the spherical solutions of Dr11, or meet an inner, pressurized region of hot gas. The difference between compact ($\gamma > 1$) and extended ($\gamma \leq 1$) radiation-confined regions (with no inner hot gas) is apparent in the top panels of Dr11's figure 2. For $\gamma \leq 1$, radiation-confined regions with $\Gamma \gg 1$ are still concentrated toward the ionization front, but the scaling of radiative acceleration with the neutral fraction allows gas to permeate the interior. This effect would only be accentuated by the

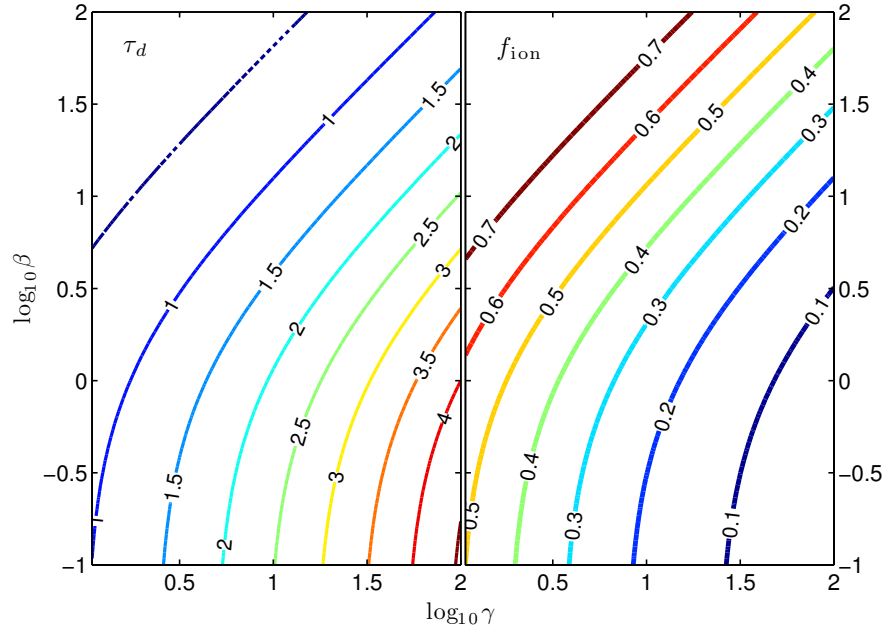


Figure 7.1: Dust optical depth, emission-averaged ionizing radiation pressure-to-gas ratio, and fraction of ionizing radiation absorbed by gas within planar, radiation-confined, dusty H II regions (equations 7.4, 7.5, and 7.8) under the assumptions of Dr11: no pressure from recombination lines, constant temperature, identical dust cross sections for non-ionizing and ionizing radiation (whose luminosity ratio is β), and no pressurized inner region ($\Omega = 0$). The parameter γ indicates the relative importance of dust in the consumption of ionizing photons in a state of equal gas and radiation pressures.

pressure of Lyman α line photons, which becomes significant when dust is scarce (Arthur et al. 2004).

The net dust optical depth τ_d and ionization efficiency f_{ion} , which reach their maximum and minimum values (respectively) in the radiation-confined state, are plotted in figure 7.1.

In figure 7.2 we plot two characteristic values of the ionizing radiation-to-gas ratio Ξ_i in the radiation-confined state: the recombination-weighted average $\Xi_{i,\text{em}}$, and the geometrical $\Xi_{i,\text{geom}}$. The latter is calculated using the emission-weighted density $n_{i,\text{em}}$. Estimates of \mathcal{U}_{obs} and $\mathcal{U}_{\text{geom}}$ derived from these limits are only approximate, because

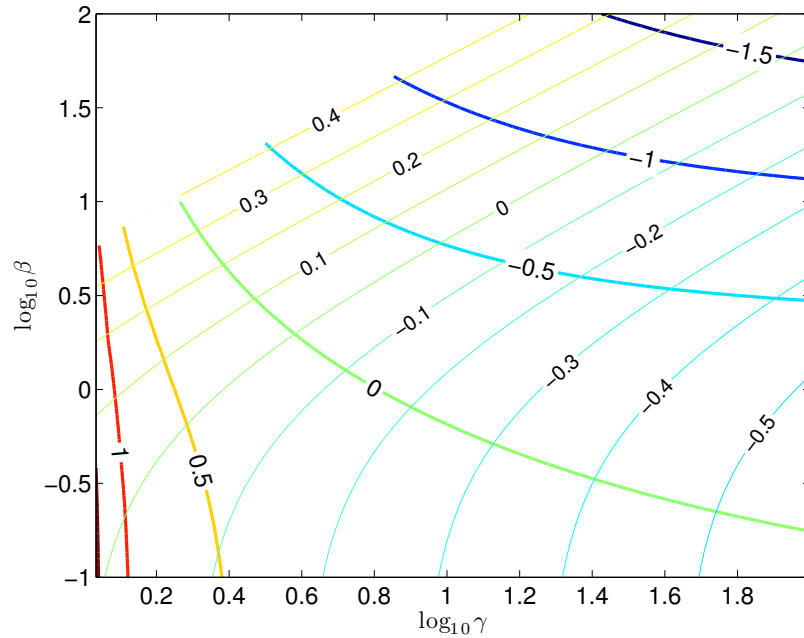


Figure 7.2: Contours of $\log_{10} \Xi_{i,\text{geom}}$ (thick lines) and $\log_{10} \Xi_{i,\text{em}}$ (thin lines) in planar, radiation-confined ionized layers with no internal pressure. Multiplied by $2.2kT_i/\bar{e}_i$, these yield estimates for the upper limits of the geometrical and line-derived values of \mathcal{U}_{obs} , respectively. However the latter is better estimated using the models of §2.6 for the specific lines in question.

line emission is not strictly proportional to the recombination rate.

Bibliography

- Abel, N. P., Dudley, C., Fischer, J., Satyapal, S., & van Hoof, P. A. M. 2009, *ApJ*, 701, 1147
- Andrews, B. H., & Thompson, T. A. 2011, *ApJ*, 727, 97
- Arthur, S. J., Kurtz, S. E., Franco, J., & Albarrán, M. Y. 2004, *ApJ*, 608, 282
- Arthur, S. J., & Lizano, S. 1997, *ApJ*, 484, 810
- Baldwin, J. A., Phillips, M. M., & Terlevich, R. 1981, *PASP*, 93, 5
- Bertin, E., & Arnouts, S. 1996, *A&AS*, 117, 393
- Bertoldi, F. 1989, *ApJ*, 346, 735
- Bertoldi, F., & McKee, C. F. 1990, *ApJ*, 354, 529
- Binette, L., Wilson, A. S., Raga, A., & Storchi-Bergmann, T. 1997, *A&A*, 327, 909
- Bottorff, M., Lamothe, J., Momjian, E., Verner, E., Vinković, D., & Ferland, G. 1998, *PASP*, 110, 1040
- Brinchmann, J., Pettini, M., & Charlot, S. 2008, *MNRAS*, 385, 769
- Carral, P., Hollenbach, D. J., Lord, S. D., Colgan, S. W. J., Haas, M. R., Rubin, R. H., & Erickson, E. F. 1994, *ApJ*, 423, 223
- Charbonnel, C., Meynet, G., Maeder, A., & Schaerer, D. 1996, *A&AS*, 115, 339

- Chu, Y.-H., & Kennicutt, Jr., R. C. 1994, *ApJ*, 425, 720
- Crowther, P. A., & Dessart, L. 1998, *MNRAS*, 296, 622
- Davis, C. J., et al. 2009, *A&A*, 496, 153
- de Koter, A., Heap, S. R., & Hubeny, I. 1998, *ApJ*, 509, 879
- Dopita, M. A., Groves, B. A., Sutherland, R. S., Binette, L., & Cecil, G. 2002, *ApJ*, 572, 753
- Dopita, M. A., Groves, B. A., Sutherland, R. S., & Kewley, L. J. 2003, *ApJ*, 583, 727
- Dopita, M. A., Kewley, L. J., Heisler, C. A., & Sutherland, R. S. 2000, *ApJ*, 542, 224
- Dopita, M. A., & Sutherland, R. S. 2003, *Astrophysics of the diffuse universe*, ed. Dopita, M. A. & Sutherland, R. S.
- Dopita, M. A., et al. 2005, *ApJ*, 619, 755
- . 2006, *ApJ*, 647, 244
- Draine, B. T. 2011, *ApJ*, 732, 100
- Dursi, L. J. 2007, *ApJ*, 670, 221
- Elitzur, M., & Ferland, G. J. 1986, *ApJ*, 305, 35
- Elmegreen, B. G., & Lada, C. J. 1977, *ApJ*, 214, 725
- Engelbracht, C. W., Rieke, M. J., Rieke, G. H., Kelly, D. M., & Achtermann, J. M. 1998, *ApJ*, 505, 639
- Erb, D. K., Shapley, A. E., Pettini, M., Steidel, C. C., Reddy, N. A., & Adelberger, K. L. 2006, *ApJ*, 644, 813
- Fall, S. M., Krumholz, M. R., & Matzner, C. D. 2010, *ApJ*, 710, L142

Ferland, G. J., & Elitzur, M. 1984, *ApJ*, 285, L11

Ferland, G. J., Korista, K. T., Verner, D. A., Ferguson, J. W., Kingdon, J. B., & Verner, E. M. 1998, *PASP*, 110, 761

Fischera, J., & Dopita, M. 2005, *ApJ*, 619, 340

Förster Schreiber, N. M., Genzel, R., Lutz, D., Kunze, D., & Sternberg, A. 2001, *ApJ*, 552, 544

Förster Schreiber, N. M., Genzel, R., Lutz, D., & Sternberg, A. 2003, *ApJ*, 599, 193

Groves, B. A., Dopita, M. A., & Sutherland, R. S. 2004, *ApJS*, 153, 9

Harper-Clark, E., & Murray, N. 2009, *ApJ*, 693, 1696

Henney, W. J., & Arthur, S. J. 1998, *AJ*, 116, 322

Henney, W. J., Arthur, S. J., de Colle, F., & Mellema, G. 2009, *MNRAS*, 398, 157

Hester, J. J., et al. 1996, *AJ*, 111, 2349

Hillier, D. J., & Miller, D. L. 1998, *ApJ*, 496, 407

Hollenbach, D. J., & Tielens, A. G. G. M. 1997, *ARA&A*, 35, 179

Indebetouw, R., et al. 2009, *ApJ*, 694, 84

Johansson, L. E. B., et al. 1998, *A&A*, 331, 857

Kennicutt, Jr., R. C., Edgar, B. K., & Hodge, P. W. 1989, *ApJ*, 337, 761

Kewley, L. J., Dopita, M. A., Sutherland, R. S., Heisler, C. A., & Trevena, J. 2001, *ApJ*, 556, 121

Koo, B., & McKee, C. F. 1992, *ApJ*, 388, 103

- Krolik, J. H. 1999, *Active galactic nuclei : from the central black hole to the galactic environment*, ed. Krolik, J. H.
- Krumholz, M. R., & Matzner, C. D. 2009, *ApJ*, 703, 1352
- Krumholz, M. R., Matzner, C. D., & McKee, C. F. 2006, *ApJ*, 653, 361
- Leitherer, C., et al. 1999, *ApJS*, 123, 3
- Lejeune, T., Cuisinier, F., & Buser, R. 1997, *A&AS*, 125, 229
- . 1998, *A&AS*, 130, 65
- Levenson, N. A., et al. 2000, *ApJ*, 533, L53
- Levesque, E. M., Kewley, L. J., & Larson, K. L. 2010, *AJ*, 139, 712
- Liu, X., Shapley, A. E., Coil, A. L., Brinchmann, J., & Ma, C.-P. 2008, *ApJ*, 678, 758
- Lopez, L. A., Krumholz, M. R., Bolatto, A. D., Prochaska, J. X., & Ramirez-Ruiz, E. 2011, *ApJ*, 731, 91
- Maeder, A., & Meynet, G. 1994, *A&A*, 287, 803
- Massey, P., & Hunter, D. A. 1998, *ApJ*, 493, 180
- Mathews, W. G. 1967, *ApJ*, 147, 965
- Mathis, J. S. 1971, *ApJ*, 167, 261
- Matzner, C. D. 2002, *ApJ*, 566, 302
- Matzner, C. D., & McKee, C. F. 1999, *ApJ*, 526, L109
- McCradly, N., & Graham, J. R. 2007, *ApJ*, 663, 844
- McKee, C. F., van Buren, D., & Lazareff, B. 1984, *ApJ*, 278, L115

- McKee, C. F., & Williams, J. P. 1997, *ApJ*, 476, 144
- McKee, C. F., & Zweibel, E. G. 1992, *ApJ*, 399, 551
- Melnick, G., Gull, G. E., & Harwit, M. 1979, *ApJ*, 227, L29
- Mihalas, D., & Mihalas, B. W. 1984, *Foundations of radiation hydrodynamics*, ed. Mihalas, D. & Mihalas, B. W.
- Murray, N., Quataert, E., & Thompson, T. A. 2010, *ApJ*, 709, 191
- O'dell, C. R., Wen, Z., & Hu, X. 1993, *ApJ*, 410, 696
- Oey, M. S., & Clarke, C. J. 1997, *MNRAS*, 289, 570
- Oey, M. S., Watson, A. M., Kern, K., & Walth, G. L. 2005, *AJ*, 129, 393
- Osterbrock, D. E., & Ferland, G. J. 2006, *Astrophysics of gaseous nebulae and active galactic nuclei*
- Pauldrach, A. W. A., Hoffmann, T. L., & Lennon, M. 2001, *A&A*, 375, 161
- Pellegrini, E. W., Baldwin, J. A., & Ferland, G. J. 2010, *ApJS*, 191, 160
- . 2011, *ApJ*, 738, 34
- Persson, S. E., Murphy, D. C., Krzeminski, W., Roth, M., & Rieke, M. J. 1998, *AJ*, 116, 2475
- Petrosian, V., Silk, J., & Field, G. B. 1972, *ApJ*, 177, L69
- Pittard, J. M. 2007, *Mass-Loaded Flows*, ed. T. W. Hartquist, J. M. Pittard, & S. A. E. G. Falle, 245
- Poglitsch, A., Krabbe, A., Madden, S. C., Nikola, T., Geis, N., Johansson, L. E. B., Stacey, G. J., & Sternberg, A. 1995, *ApJ*, 454, 293

- Probst, R. G., George, J. R., Daly, P. N., Don, K., & Ellis, M. 2008, in Society of Photo-Optical Instrumentation Engineers (SPIE) Conference Series, Vol. 7014, Society of Photo-Optical Instrumentation Engineers (SPIE) Conference Series
- Puxley, P. J., Ramsay Howat, S. K., & Mountain, C. M. 2000, *ApJ*, 529, 224
- Roy, A. L., Goss, W. M., Mohan, N. R., & Anantharamaiah, K. R. 2005, *A&A*, 435, 831
- Rubio, M., Barbá, R. H., Walborn, N. R., Probst, R. G., García, J., & Roth, M. R. 1998, *AJ*, 116, 1708
- Russell, R. W., Melnick, G., Gull, G. E., & Harwit, M. 1980, *ApJ*, 240, L99
- Russell, R. W., Melnick, G., Smyers, S. D., Kurtz, N. T., Gosnell, T. R., Harwit, M., & Werner, M. W. 1981, *ApJ*, 250, L35
- Schaerer, D., Charbonnel, C., Meynet, G., Maeder, A., & Schaller, G. 1993a, *A&AS*, 102, 339
- Schaerer, D., Meynet, G., Maeder, A., & Schaller, G. 1993b, *A&AS*, 98, 523
- Schaller, G., Schaerer, D., Meynet, G., & Maeder, A. 1992, *A&AS*, 96, 269
- Schmutz, W. 1998, in *Astronomical Society of the Pacific Conference Series*, Vol. 131, *Properties of Hot Luminous Stars*, ed. I. Howarth, 119
- Shapley, A. E., Coil, A. L., Ma, C.-P., & Bundy, K. 2005, *ApJ*, 635, 1006
- Slavin, J. D., & Cox, D. P. 1993, *ApJ*, 417, 187
- Smith, L. J., Norris, R. P. F., & Crowther, P. A. 2002, *MNRAS*, 337, 1309
- Smith, L. J., Westmoquette, M. S., Gallagher, J. S., O'Connell, R. W., Rosario, D. J., & de Grijs, R. 2006, *MNRAS*, 370, 513
- Snijders, L., Kewley, L. J., & van der Werf, P. P. 2007, *ApJ*, 669, 269

Storey, J. W. V., Watson, D. M., & Townes, C. H. 1979, *ApJ*, 233, 109

Storey, P. J., & Hummer, D. G. 1995, *MNRAS*, 272, 41

Strömgren, B. 1939, *ApJ*, 89, 526

Swaters, R. A., Valdes, F., & Dickinson, M. E. 2009, in *Astronomical Society of the Pacific Conference Series*, Vol. 411, *Astronomical Data Analysis Software and Systems XVIII*, ed. D. A. Bohlender, D. Durand, & P. Dowler, 506

Tan, J. C., & McKee, C. F. 2003, in *IAU Symposium*, Vol. 221, *IAU Symposium*, 274P

Tarter, C. B., Tucker, W. H., & Salpeter, E. E. 1969, *ApJ*, 156, 943

Thornley, M. D., Schreiber, N. M. F., Lutz, D., Genzel, R., Spoon, H. W. W., Kunze, D., & Sternberg, A. 2000, *ApJ*, 539, 641

Townsley, L. K., Broos, P. S., Feigelson, E. D., Brandl, B. R., Chu, Y.-H., Garmire, G. P., & Pavlov, G. G. 2006, *AJ*, 131, 2140

Townsley, L. K., Feigelson, E. D., Montmerle, T., Broos, P. S., Chu, Y.-H., & Garmire, G. P. 2003, *ApJ*, 593, 874

van Dishoeck, E. F., & Black, J. H. 1988, *ApJ*, 334, 771

van Hoof, P. A. M., Weingartner, J. C., Martin, P. G., Volk, K., & Ferland, G. J. 2004, *MNRAS*, 350, 1330

Vázquez, G. A., & Leitherer, C. 2005, *ApJ*, 621, 695

Veilleux, S., Cecil, G., & Bland-Hawthorn, J. 2005, *ARA&A*, 43, 769

Veilleux, S., & Osterbrock, D. E. 1987, *ApJS*, 63, 295

Voit, G. M. 1992, *ApJ*, 399, 495

- Weaver, R., McCray, R., Castor, J., Shapiro, P., & Moore, R. 1977, *ApJ*, 218, 377
- Westmoquette, M. S., Smith, L. J., Gallagher, III, J. S., O'Connell, R. W., Rosario, D. J., & de Grijs, R. 2007, *ApJ*, 671, 358
- Westmoquette, M. S., Smith, L. J., Gallagher, III, J. S., Trancho, G., Bastian, N., & Konstantopoulos, I. S. 2009, *ApJ*, 696, 192
- Whitworth, A. 1979, *MNRAS*, 186, 59
- Williams, J. P., & McKee, C. F. 1997, *ApJ*, 476, 166
- Williams, R. E. 1972, *ApJ*, 178, 105
- Wong, T., et al. 2011, *ApJS*, 197, 16
- Wood, D. O. S., & Churchwell, E. 1989, *ApJS*, 69, 831
- Wu, Y., Wei, Y., Zhao, M., Shi, Y., Yu, W., Qin, S., & Huang, M. 2004, *A&A*, 426, 503
- Yeh, S. C. C., & Matzner, C. D. 2012, *ApJ*, 757, 108
- Zavagno, A., et al. 2010, *A&A*, 518, L101